UNIVERSIDAD DE CHILE
FACULTAD DE CIENCIAS FÍSICAS Y MATEMÁTICAS
DEPARTAMENTO DE INGENIERÍA ELÉCTRICA

DESIGN AND MEASUREMENTS OF AN OPTICAL SYSTEM FOR ALMA BAND 1

TESIS PARA OPTAR AL GRADO DE MAGISTER EN
INGENIERÍA ELÉCTRICA

VALERIA VICTORIA TAPIA LABARCA

PROFESOR GUÍA:
FAUSTO PATRICIO MENA MENA

MIEMBROS DE LA COMISIÓN:
RICARDO ALBERTO FINGER CAMUS
ÁLVARO GONZÁLEZ GARCÍA
NICOLÁS ANDRÉS REYES GUZMÁN

Este trabajo ha sido parcialmente financiado por CONICYT, a través de sus programas
Fondo Basal (Proyecto PBF06), Fondo ALMA para el Desarrollo de la Astronomía
(Proyecto 31120005)

SANTIAGO DE CHILE
2015

RESUMEN

DISEÑO Y MEDICIÓN DE UN SISTEMA ÓPTICO PARA LA BANDA 1 DE ALMA

El proyecto astronómico ALMA, Atacama Large Millimeter/submillimeter Array, es el radiobservatorio interferométrico más grande del mundo. Se compone de 66 antenas con diámetros de 7 y 12 m, ubicadas en el norte de Chile a una altitud de 5000 m sobre el nivel del mar. Su excelente localización y tecnología proveerán sensibilidad y resolución sin presedentes para el estudio de los origenes del universo, formación y evolución de galaxias, estrellas, planetas y la compleja química del medio interestelar. Por ello, ALMA constituye un gran desafío en diversas áreas de la ciencia y la tecnología.

En esta tesis se presenta el diseño, contrucción y caracterización del sistema óptico para el receptor heterodino de la Banda 1 de ALMA. Este sistema combina una serie de exigentes especificaciones técnicas, limitaciones de construcción y restricciones de costo que requieren equilibrarse. El sistema debe cubrir el rango de frecuencia entre 35–50 GHz (con el objetivo de extenderlo hasta 52 GHz) sin ninguna sintonización mecánica, lograr un eficiencia de apertura para toda la banda que supere el 80%, poseer una apertura de polarización superior a 99.5%, incluir en torno a 10 K de ruido, poseer un error de alineamiento menor a 5 mrad respecto a la posición nominal y no debe interferir con los dispositivos ya existentes. Además, el sistema debe ser compatible para las antenas de 7 y 12-m, que poseen un ángulo de iluminacón distinto al secundario.

El sistema óptico consiste en una antena tipo bocina compacta corrugada, una membrana de gore-tex y membrana ranurada de teflón como filtros de las etapas de 15 y 110 K, respectivamente, y un lente con zona biconvexo fabricado de polietileno que incluye corrugaciones como capa anti-reflectora. Está tesis se enfoca en la antena tipo bocina y el lente.

El proceso de diseño de los dipositivos se realizó de manera iterativa, por lo que dos modelos de antenas tipo bocina y tres lentes de una zona son presentados. El diseño de las antenas consistió en determinar las características necesarias del patrón radiativo utilizando modelos cuasiópticos. Luego se optimizó su perfil utilizando ténicas de adaptación modal y algoritmos genéticos. El procedimiento de diseño de lentes fue similar al utilizado para la bocina. Primero, se consideraron como parámetros iniciales los valores calculados mediante el modelo quasioptico y luego se realizaron análisis de sensibilidad utilizando la ténica de método de los momentos y método de elementos finitos.

El mejor sistema en simulación corresponde a la segunda versión de la antena y la tercera del lente. Este sistema cumple totalmente las especificaciones mencionadas, logrando eficiencias de apertura mejores que 80.4% para toda la banda. La temperaturas de ruido promedio calculada es de 10.4 K, donde el lente presenta la mayor contribución con aproximadamente 7 K. Además, el sistema es compatible para la antena de 7 y 12 m, si el lente se desplaza 5.66 mm hacia el centro del criostato en la configuración de 7-m, con degradaciones en eficiencia de apertura menores a 0.5%.

Por último se presentan dos sistemas caracterizados, correspondientes a la primera antena más la primera o segunda lente, pues al momento de escribir esta tesis, el resto de dispositivos se encontraban en construcción. El mejor sistema medido poseen eficiencias de apertura mejores que 79.2% en excelente concordancia con las simulaciones. Además, se han identificado algunas fuentes de error que poseen las mediciones, incluyendo errores en alineamientos y cambios de fase por temperatura.

ABSTRACT

DESIGN AND MEASUREMENTS OF AN OPTICAL SYSTEM FOR ALMA BAND 1

The Atacama Large Millimeter Array (ALMA) is the largest millimeter and submillimeter radio telescope in the world. It consists of 66 antennas with diameters of 7 and 12 m. It has been constructed in the north of Chile at an altitude of 5000 m above sea level. Its excellent location and technology provides unprecedented sensitivity and resolution for the study of the origins of the universe; formation of galaxies, stars, and planets; and the complex chemistry of the interstellar medium. Therefore, ALMA is a major challenge in many areas of science and technology.

This thesis presents the design, construction and characterization of the optical system of the Band-1 heterodyne receiver. This system combines a series of stringent technical specifications, construction limitations and cost constraints that require trade-offs with each other. The optical system must cover the frequency range between 3550 GHz (with the goal of extending the coverage to 3552 GHz) without mechanical tuning, meet a total aperture efficiency that exceeds 80% and a polarization efficiency better than 99.5%, add noise close to 10 K, attain an angular alignment of the optical beam within 5 mrad of the nominal direction, and it cannot interfere with the already-existing devices. Furthermore, the 7 and 12-m antennas use the same front end which leads to different beam tilt angles to the secondary.

The optical system consists of a compact spline-profile corrugated horn, a thin gore-tex membrane and a grooved surface of teflon as infrared filters at the 15 and 110-K stages, respectively, and a low-loss polyethylene biconvex one-zone lens that includes a corrugated anti-reflection coating. This thesis focuses on the horn and lens.

The design process of the components was performed by iterations, therefore, two horn antennas and three one-zoned lenses are presented. The antenna design consists on determining the needed quasi-optical beam pattern parameters and then optimize the profile of the horn using Mode-matching techniques and genetic algorithms. The lens design was similar to the horn. First, a quasi-optical model to calculate initial values was used, and then a sensitivity analysis was performed using the method of moments and the finite-element method.

The best simulated system correspond to the second horn and third lens. This system is totally in specs, achieving an aperture efficiency better than 80.4% in the full band. An average noise temperature of 10.4 K was calculated, where the lens is the principal contributing device (about 7 K). Moreover, the system can be used in the 7-m antennas if the lens is offset 5.66 mm from the center of the cryostat respect to the 12-m antenna. This causes minor degradation in aperture efficiencies (lower than 0.5%).

Finally, we present two characterized optical systems, corresponding to the first antenna plus the first or second lenses, since at the time of writing the other devices were under construction. The best measured system achieves aperture efficiencies better than 79.2% in excellent agreement with simulations. Moreover, we have identified the main error sources in the measurements, that include misalignment errors and phase instability.

My sincere gratitude to the Millimeter Wave Laboratory team for their continuous support, trust and help. In the same way, I would like to express my gratitude to the ALMA Band 1 team for sharing their knowledge, for their insightful comments and stimulating discussions. Finally, I would like to thank my family, Luis Tapia, Sandra Labarca, Evelyn Tapia and Hernán Calderón. Without their love, support and patience, the process of creation of this thesis could not be possible.

Contents

List of Tables

List of Figures

Chapter 1

Introduction

Multiples astronomical projects have been established in the north of Chile owing to its extraordinary atmospheric conditions for the study of the universe. The Atacama desert in the north of Chile has extensive plains over the thermal inversion layer, little light pollution, low levels of electromagnetic radiation and excellent seeing. Particularly, the Chajnantor plateau situated at 5000 m above the sea level, combines a high altitude and dryness of the Atacama Desert. It achieves a very low amount of precipitable water vapor around typically 1 mm, except the altiplanic winter [1] [2]. All these conditions allow high levels of radio frequency transmission for at least 9 months a year. Hence, it is a perfect place to locate the largest radio astronomy project in the world, ALMA.

ALMA, Atacama Large Millimeter / sub-millimeter Array, is a gigantic revolutionary interferometric radio telescope created by international partnership. Such consortium includes the collaboration of Europe, North America, East Asia and Chile. It was designed to observe millimeter and sub-millimeter waves in the range of frequency between 35–950 GHz divided in 10 frequency bands as described in table 1.1.

Table 1.1: ALMA receivers frequency bands

ALMA band	Frequency range (GHz)	Bandwidth (%)
1	35–50	35.9
2	67–90	29.6
3	84–116	32.4
4	125–163	26.6
5	162–211	26.5
6	211–275	26.6
7	275–373	30.6
8	385–500	26.2
9	602–720	17.9
10	787–950	18.9

ALMA is constituted by two arrays. The main array consists of 50 antennas of 12 -meters and the Atacama Compact Array (ACA) constituted by 12 antennas of a diameter 7 -meters plus 4 12 -

meters antennas called the Total Power Array (TP Array). It has a total collecting area of 5650 m^2 with configurations allowing base lines up to 16 km with an angular resolution of 5 milli-arcseconds in the most extended configuration.

1.1 Specific background

The ALMA project is a major technological challenge in various areas of science and engineering, since the ambitious scientific goals require unprecedented technical challenges. Particularly, for engineers dedicated to develop instrumentation, the challenge is to create highly sensitive receivers, with very low noise and large bandwidth to study the far and cold universe composed mainly by the interstellar medium and radiation of cosmic background.

The radio waves from the universe are collected and concentrated by a reflector antenna, which guides the radiation from the main plate to the sub-reflector sending it to the first electronic device, the heterodyne receiver. This receiver is responsible for capturing, amplifying and down-converting the signal under study.

The heterodyne receivers are coherent detectors widely used in radio astronomy and telecommunications. They convert the incoming signal into a lower frequency, called Intermediate Frequency (IF) signal, maintaining the phase and amplitude of the original signal. The aim of this conversion is to make the post-processing easier.

A usual heterodyne radio receiver is shown in figure 1.1. This configuration is called Single Side Band. In this configuration, the Radio Frequency (RF), composed by the Lower Side Band (LSB) and the Upper Side Band (USB) signals, is collected by the antenna and then conducted to the second device, a Low Noise Amplifier (LNA), which amplifies the incoming signal adding some noise. Afterwards, the signal is filtered in order to suppress one of the bands and to be down-converted by a mixer soon after.

A mixer is a nonlinear component to produce an output consisting of the sum and difference of the frequency of two input signals, being Schottky diodes the most common technologies for down-conversion lower than 100 GHz and Superconductor Isolator Superconductor (SIS) junctions to higher frequencies [3] [4]. In radio receivers, the main input is the RF signal and the second one is a reference signal known as Local Oscillator (LO). The output are IF $\omega_{IF} = \omega_{RF} \pm \omega_{LO}$ and harmonics terms $n \cdot \omega_{RF} + m \cdot \omega_{LO}$, m and n are integers, where the term of interest is $\omega_{RF} - \omega_{LO}$ [3]. Therefore, an additional filter is needed to eliminate the spurious frequencies produced by the mixing process. Finally, the signal is amplified.

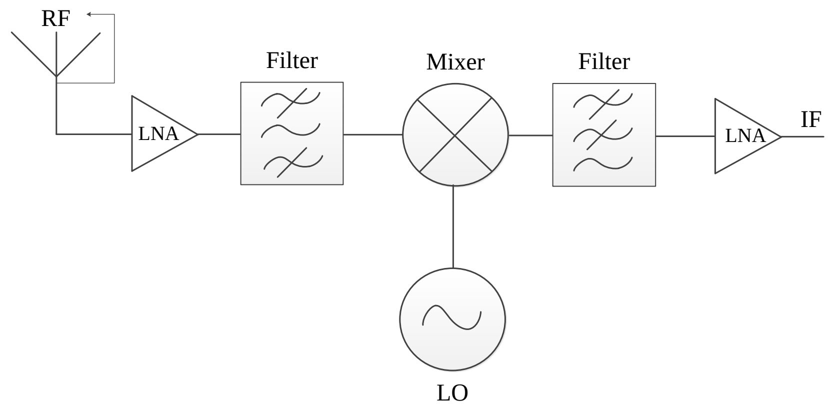

Figure 1.1: Usual configuration of a single sideband heterodyne radio receiver. The input is a RF signal is first filtered, amplified and mixed. The resulting signal is filtered and amplified again, in order to obtained the IF signal which is easier to post-process than the original RF signal.

If the filters stage is not included, the receiver corresponds to the simplest configuration, the Double Side Band (DSB). Due to the fact that the components of the RF signal are not filtered, the resulting IF signal includes the LSB and USB response overlapped, making the analysis and increase the noise of the signal difficult. On the other hand, in order to observe the two sidebands at the same time, a more complex configuration can be used , as the Side Band Separating (2SB) that avoids the overlapping of the signal. A detailed description about the configuration of the receivers can be found in [5] and [6].

Particularly, the Band 1 receiver can be divided into three parts, the optical, amplification and down-conversion system. In Band 1, the radio frequency signal goes through a lens and then through two infrared filters reaching a horn antenna. The latter captures the signal allowing its reception and transporting it to a second device called Ortho-Mode Transducer (OMT), which divides the signal in two orthogonal polarizations. The two independently polarized waves pass to the next stage, each one follows a SSB configuration, where the amplification is performed by an amplifier based on a High Electron Mobility Transistor (HEMT). Then, using a mixer based on a Schottky mixer, the down-conversion of the signal frequency is performed. Finally, the IF signal is filtered and amplified in order to have appropriate conditions for the Back-End processing.

In order to minimize the noise introduced by the receiver each subsystem has to be optimized, in particular those at the beginning of the chain. Since the optics is the first subsystem in the receiver chain of each antenna, achieving good noise temperature and aperture efficiency are fundamental for best sensitivity [7]. This thesis presents the design and results of the optical system for the Band-1 receivers of ALMA.

1.1.1 Science with ALMA Band 1

The original frequency range to Band 1 was defined from 31.3 to 45 GHz. Nevertheless, in order to improve the astronomical science, the frequency coverage was modified to the range from 35 to 50 GHz [8][9]. The current long wavelength of the Band-1 receiver, in addition to its high sensitivity and resolution, unprecedented information about planetary formations , stars, galaxies, the Interstellar Medium (ISM) and the Cosmic Microwave Background (CMB) can be provided.

The detection of continuous emissions from gas, dust and particles can be used to study the formation of planets. An important scientific case is detailing the evolution of grains involved in the process of accretion in protoplanetary disks. Most of the mass in the disk are grains that emit at millimeter and centimeter wavelengths, converting ALMA Band-1 in a specially useful tool to study the evolution of planetary formation.

Through the characterization of molecular hydrogen, H_2, molecular clouds, where star formation occurs, can be studied. However, H_2 despite of being the most abundant molecule in the universe is difficult to find since of their transition lines are weak. Therefore, indirect detection is used through tracers. The most common tracer is CO. ALMA Band 1 will allow the observation of CO_{1-0}, CO_{2-1} and CO_{3-2}, including red-shift $1.3<z<2.5$, $3.6<z<6.0$ and $6<z<10$ respectively. In this way, distant galaxies can be studied. Band 1 will increase by a factor of 8, the observable Universe in CO.

Regarding the dynamics and chemistry associated with star formation, it can be study tracing complex organics molecular lines providing meaningful information. In the ALMA Band-1 frequency range twenty complex organics molecules, as HC_5N or CH_3OH, have transitions. Moreover, the system noise temperature at Band 1 will be significantly lower than in ALMA higher bands, giving extra sensitivity to detect weak transitions from less abundant molecules.

Masers correspond to a microwave amplification by stimulated emission. Band 1 meets the conditions to observe several SiO and CH_3OH maser lines. This lines can be used to observe very specific physical conditions in the ISM and probe theoretical models about its production mechanisms.

The Sunyaev Ze$'$dovich is a spectral distortion effect produced by hot electrons that interact with low energy photons from the CMB producing small fluctuations. The energy of these photons is increased and the blackbody spectra of CMB is modified shifted up in frequency. Band 1 will helps to detect this density perturbations at high redshift and possibly to separate the effect from other phenomena. A more detailed description of each topic outlined here can be found in [10].

1.2 Objectives

The general objectives of this work is to design and characterize an optical system for the heterodyne receiver of ALMA Band 1 including a horn antenna and a bi-hyperbolic lens that meets the electrical and mechanical targets listed below.

- The optical system shall be frequency independent between 35–50 GHz (with minor degradation) without mechanical tuning.

- The aperture efficiency shall exceeded 80%, taking into account the efficiency of amplitude, phase, polarization and spillover.

- The cross-polarization efficiency shall be at least of 99.5%.

- The noise temperature due to the complete optical system shall be about 10 K.

- The far-field beam shall have a maximum angular alignment error of 5 mrad relative to the nominal direction.

- The system shall be compatible with the 7 and 12-meters antennas, which have different angles of projection on the sub-reflector.

- If warm optics is used, it shall not interfered with the calibration system or any other existing device.

- The interface between the horn antenna and the rest of the heterodyne receiver shall be a circular waveguide with diameter of 6.7 mm.

- The devices shall be designed considering a mass production of 70 units, 1 for each antenna module plus 4 spares.

In addition, we want to achieve these complementary objectives,

- Analyze the matching between the beam pattern measurements and the HFSS-IE software results in order to validate the simulation accuracy.

- Create and improve the existent post-processing scripts to analyze the measurement and simulation data.

1.3 Scope of this thesis

The Band-1 receiver is being developed by a consortium leaded by the Academia Sinica Institute of Astronomy & Astrophysics (ASIAA) from Taiwan. It includes the collaboration of the National Radio Astronomy Observatory (NRAO), from USA, the Herzberg Institute of Astrophysics (HIA) from Canada, National Astronomical Observatory of Japan (NAOJ) and Universidad de Chile.

A full schematic diagram of the heterodyne receiver is shown in figure 1.2. The optical system, which is constituted by the warm optics, the vacuum windows and the cold optics is being developed by a collaboration between Universidad de Chile and NAOJ. The next device in the chain, the OMT, is in charge of HIA. The Cryogenic HEMT for the LNA, and LO are provided by NRAO. Additionally, management and testing facility support are provided by NAOJ. The cartridge design, down-conversion and the assembly processes are performed by ASIAA. Detailed information about every sub-system can be found in [11] and [12].

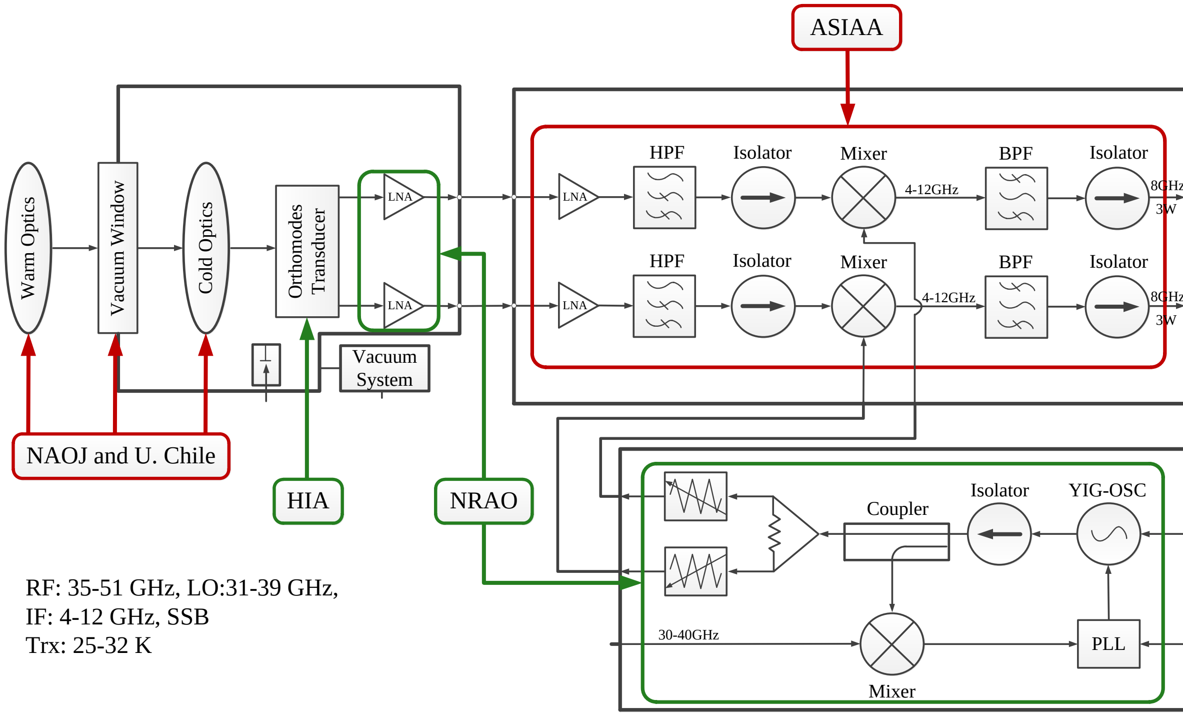

Figure 1.2: Schematic of Band 1 heterodyne receiver and consortium colaboratium.

The proposed baseline design for Band-1 optical system consists on a standard cold horn and a warm lens [13]. A first working design in the older Band-1 frequency range (31.3–45 GHz) was developed by Pablo Zorzi [14]. This system consisted on a HDPE bi-hyperbolic lens without anti-reflection coating and a spline profile corrugated horn constructed as a split block [15]. It achieved a measured aperture efficiency, better than 77.64%, and a noise contribution lower than 14.4 K. Afterwards, a second iteration was conducted to cover the current range of Band 1 defined from 35 to 50 GHz. A detailed comparison among several proposed configurations for Band 1 was conducted by Nicolas Reyes et al [16]. The best configuration was found to be a spline-profile horn (machined as a single block) [17] and a zoned lens solution [18]. The design process shown in this thesis starts at this point.

1.4 Summary of this thesis

This thesis starts with chapter 2 reviewing the main theoretical and practical concepts necessary to understand and contextualize the optical system under study. We describe in a general way the designed devices (horn antennas and dielectric lens), the main characterization parameters (Beam pattern, efficiencies and noise temperature) and the electromagnetic modeling techniques used for simulation. In chapter 3 we discuss in depth the main technical constraints and construction limitation to be considered in the full optical system. The methodology and evolution of the design of the lenses and the horn antennas are presented. All the proposed designs, including beam patterns simulations results, calculation of efficiency and estimation of noise temperature are also presented. Chapter 4 shows and analyses the results corresponding to reflection-loss and beam-pattern measurements. Besides, the analysis of the sources of error and possible improvements to the system are discussed. Additionally, the electromagnetic characterization of the HDPE material is shown. Finally, in chapter 5 the conclusions of the work performed are listed by comparing the initial objectives with the goals achieved, and future work is proposed.

Chapter 2

Literature review

In this chapter we present a review of the main concepts and theoretical support to understand the design, construction and characterization of the optical system studied in this thesis. For this purpose we will review the gaussian beam as a solution for the quasioptical analysis and the electromagnetic modeling techniques used to simulate the designs presented in this thesis reviewing the general mathematical background and its particularities. Moreover, the main characteristics of dielectric lens, horn antennas and Cassegrain reflectors are described.

2.1 Gaussian beam

The electromagnetic radiation phenomenon can be studied from different approaches, being the simplest one the geometrical optics and the most complex the use of full electromagnetic theory. The best approach will be the simplest model that describes properly the problem to be solved. If the wavelength of the radiation is much smaller than the propagation system dimensions, the behavior of the wave can be described by rays and a set of geometrical rules called geometrical optics. On the other hand, electromagnetic theory provides a complete treatment of the wave solution in general problems. Nevertheless, electromagnetic calculations are hard to solve in a general system and they are time consuming. A halfway approach is the quasioptical theory, describing the radiation behavior when the wavelength of the radiation is comparable to the system dimensions. It describes the propagation of a radiation beam that is reasonably well collimated but has relatively small dimensions when it is measured in wavelengths that are transverse to the axis of propagation [19].

In particular, in this chapter we will review a solution of the quasioptical analysis specially useful for millimeter and sub-millimeter feed horn systems, the gaussian beam propagation.

2.1.1 Derivation of Gaussian beam propagation

The gaussian beam propagating in a uniform medium, satisfies an approximation of the Helmholtz equation,

$$(\nabla^2 + k^2)\psi = 0, \tag{2.1}$$

where ψ represents any component of E or H and k is the wave-number. A propagation beam is essentially a plane wave with some variation in the perpendicular direction to the axis of propagation. We can assume that both electric and magnetic fields are perpendicular to each other and to the direction of propagation. Consequently, the electric field can be describe by

$$E(r, z) = u(r, z)\mathrm{e}^{-jkz} \tag{2.2}$$

where positive z is the direction of propagation, u is a complex scalar function that defines the non-plane part of the beam and we assume symmetry of u in ϕ.

We assume that the variation of the amplitude u along the direction of propagation is small over distances comparable with the wavelength. Additionally, we assume that the variation perpendicular to this direction is small compared to the axial variation. This assumption is called the paraxial approximation and can be written as

$$\frac{\Delta\frac{\partial u}{\partial z}}{\Delta z}\lambda << \frac{\partial u}{\partial z} \tag{2.3}$$

If we substitute the equation 2.2 in 2.1 using cylindrical coordinates and the paraxial approximation, the wave propagation can be written as

$$\frac{\partial^2 u}{\partial r^2} + \frac{1}{r}\frac{\partial u}{\partial r} - 2jk\frac{\partial u}{\partial z} = 0. \tag{2.4}$$

The solutions to this equation describe the Gaussian beam modes that form the quasioptical beam. It can be demonstrated [19] that the normalized fundamental solution for equation 2.4 is

$$E(r, z) = \sqrt{\frac{2}{\pi w(z)^2}}\exp\left(\frac{-r^2}{w(z)^2} - jkz - \frac{j\pi r^2}{\lambda R(z)} + j\phi_0(z)\right) \tag{2.5}$$

where R, w and ϕ_0 define the behavior of the beam and they are shown in figure 2.1. R is the radius of curvature of the beam wavefront defined by

$$R(z) = z + \frac{1}{z}\left(\frac{\pi w_0^2}{\lambda}\right)^2. \tag{2.6}$$

$$\tag{2.7}$$

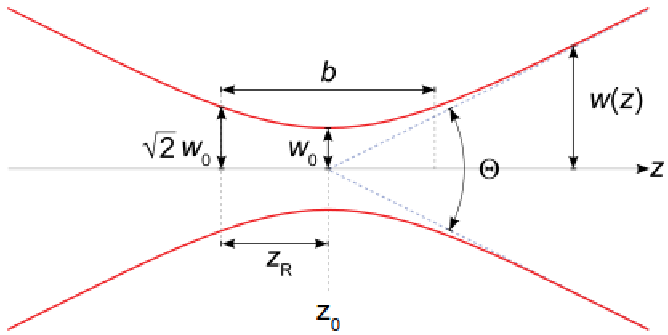

Figure 2.1: Main Gaussian-beam parameters. z is the propagation axis, w the beam radius, $w_0 = w(z_0)$ is the beam waist and θ is the equivalent angle.

When the field amplitude drops 1/e this value is called Beam Waist (BW) size and corresponds to $w_0 = w(z = 0)$. The radius at any point is w and it is defined by

$$w(z) = w_0 \sqrt{1 + \left(\frac{\lambda z}{\pi w_0^2}\right)^2}. \tag{2.8}$$

$$\tag{2.9}$$

The Phase Center Location (PCL) is defined as the axis of equi phase fronts and it is the equivalent to the point source in the geometrical optics approximation. Gaussian beam theory, commonly use the PCL as the reference point as well $w(z_{PCL}) \approx w_0$. Finally, ϕ_0 is the phase shift defined by

$$\phi_0 = \arctan\left(\frac{\lambda z}{\pi w_0^2}\right) \tag{2.10}$$

The solution to the paraxial wave equation presented above is the simpler solution. However, it is not the only one. A complete mathematical description of the beam pattern and its propagation can be achieved using higher order Gaussian beam modes transverse to the axis of propagation. The most common application are off-axis mirror and corrugated feed horns. Assuming axial symmetry, in cylindrical coordinates the equation to describe higher order modes is

$$E_{p0}(r, z) = \sqrt{\frac{2}{\pi w(z)^2}} L_{p0}\left(\frac{2r^2}{w(z)^2}\right) \exp\left(\frac{-r^2}{w(z)^2} - jkz - \frac{j\pi r^2}{\lambda R(z)} + j\,(2p+1)\,\phi_0(z)\right) \tag{2.11}$$

where L_{p0} are the ordinary Laguerre polynomials, and in the Gaussian beam context p is the radial index and describes the order of the mode. The electrical fields related to the first four lower modes are shown in the figure 2.2, including the fundamental mode.

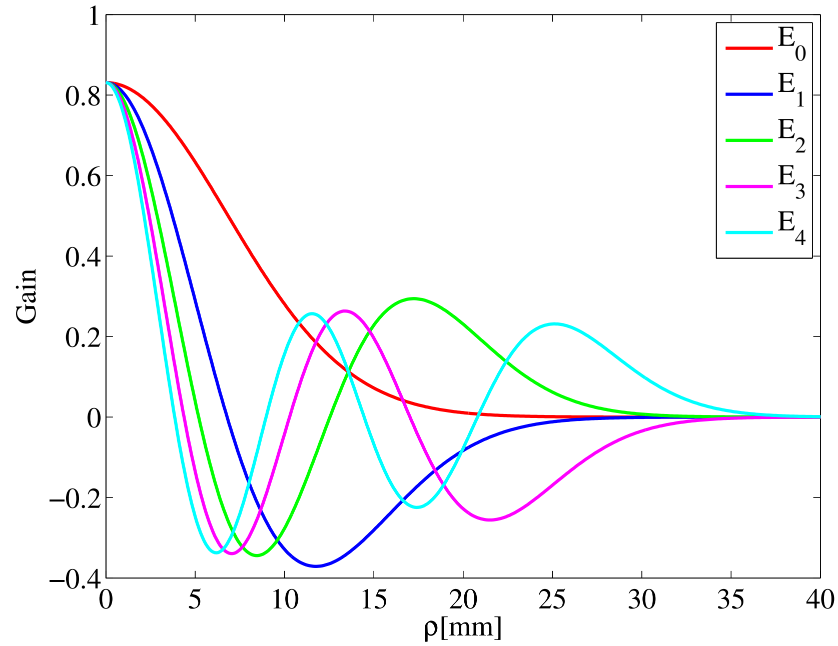

Figure 2.2: Higher order Gaussian beam modes.

2.1.2 Near and far-field patterns

The radiating space of any emitting device can be divided in three regions, reactive near-field, radiating near-field and far-field. It is important to note that the transition among these regions is smooth and a unique criterion to establish them does not exist. The reactive near-field surrounds the antenna and is the region wherein the reactive field predominates. It is given by $z < 0.62\sqrt{D^3/\lambda}$, where D is the diameter of the aperture in aperture antennas, and λ the wavelength. The radiating near-field, also called Fresnel zone, is the intermediate region between the reactive near-field and the far-field. In this region, the radiation field depends on the radial distance and the distribution at this distance. The far-field, also known as Fraunhofer zone, is the region defined by $z > 2D^2/\lambda$ where the angular field distribution is essentially independent from the distance of the antenna [20].

The confocal distance z_c or Rayleigh range defines the boundary between the near and the far-field in a different way than the previous definition [19]. It is more useful for gaussian-beam approximation so it will be widely used in this thesis. It is defined as

$$z_c = \frac{\pi w_0^2}{\lambda}. \tag{2.12}$$

We consider that $z << z_c$ defines the near field, because in this place the beam radius is practically the same as the beamwaist $w \leq \sqrt{w_0}$. For $z >> z_c$ the beam radius and the radius of the curvature increase linearly with the distance. In this limit we can use the relation

$$\theta_0 = \frac{\lambda}{\pi w_0}. \tag{2.13}$$

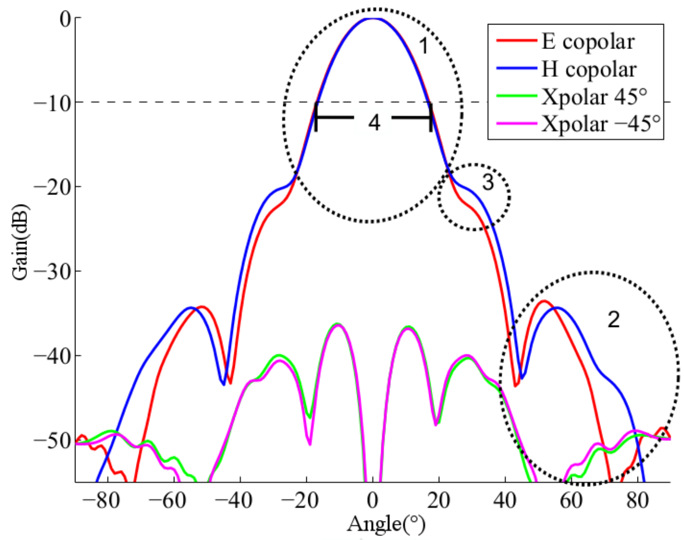

Figure 2.3: Cross-section of a radiation pattern. (1) Main or major lobe, (2) side or minor lobes, (3) shoulder lobes and (4) 10-dB point.

2.1.3 Radiation pattern

Radiation patterns are a graphical representation of the radiation properties as a function of the space coordinates. They can be two or three dimensional, relative to the power or energy in linear or logarithmic scale. It is used to represent the near-field or most commonly the far-field of the radiation [20]. Particularly, in this thesis, we will use the two dimensional pattern in logarithmic scale to represented the radiation of the antennas presented.

The polarization patterns are the spatial distribution of the polarizations of a field vector radiated (or excited) by an antenna taken over its radiation sphere. At each point on the radiation sphere the polarization is usually resolved into a pair of orthogonal polarization, tangent at each point on the sphere, the co-polarization and the cross-polarization. The polarization that the antenna is intended to radiate (or receive) is called copolarization or copolar. The radiation orthogonal to a specified polarization (usually the copolarization) is called cross-polarization, crosspolar or Xpolar [21]. If a Huygens source [1] is used as reference polarization, the most usual coordinates system is the third definition of Ludwig,

$$E_{co} = E_\theta \cos\phi - E_\phi \sin\phi \tag{2.14}$$

$$E_x = E_\theta \sin\phi + E_\phi \cos\phi \tag{2.15}$$

where E_{co} is the copolarization, E_x is the crosspolarization, and θ and ϕ are the usual spherical coordinates components and the main vector is aligned with the y-axis.

In figure 2.3 we can appreciate some important characteristics of the radiation pattern that are intensively used in this thesis. They are the following.

[1]Electric and magnetic dipoles with orthogonal axes lying in the aperture plane and radiating equal field in phase along z-axis

- **Plane E**: For linearly polarized antennas, it is the reference radiation plane that contains the electrical field vector and the direction of maximum power.
- **Plane H**: The definition is similar to the plane E. It is the radiation plane that contains the magnetic field vector and the direction of maximum power.
- **Main lobe**: This lobe, also called major lobe, contains the the direction of maximum power of the pattern. It is not necessarily a single lobe.
- **Side lobes**: These lobes, also called minor lobes, contains the local maximums power of the pattern. Usually, this is the power lost in undesired directions.
- **Back lobes**: It is the power radiate in the opposite of the main lobe.
- **Shoulder lobes**: They correspond to a side-lobe attached to a main lobe.
- **10-dB point**: It is the beamsize when the normalized radiation has a value of -10 dB.
- **Edge taper**: It is the relative power density at a defined radius. To a fundamental Gaussian beam at a radius r_e is given by

$$T_\mathrm{e}(r_\mathrm{e}) = \exp\left(\frac{-2r_\mathrm{e}^2}{w^2}\right) \tag{2.16}$$

2.2 Electromagnetics Modelling Techniques

Gaussian beam allows efficient analysis of quasioptical systems. Nevertheless, depending on the applications, more accurate methodologies are required in order to study the real behavior of the optical system, being necessary to solve the electromagnetic equations.

The equations needed to model electromagnetic problems are frequently very complicated or impossible to solve in closed form. In most of the cases, it is necessary to use numerical approximations to know the behavior of the system. Fortunately, modern computers have the necessary characteristics to solve very complex problems including a large number of variables and sophisticated geometries.

The different techniques have different stability, accuracy, reliability and adaptivity. Consequently, the technique to be applied to each problem should be carefully chosen in order to obtain a good agreement between the model and reality.

In this section we will review the main mathematical and algorithmic techniques used in the design shown in this thesis: mode matching technique, method of the moments and finite element method. These tools were used through two softwares, HFSS (High Frequency Structural Simulator, from Ansys, including finite element method and method of the moments), and MWW (MicroWave Wizard, from Mician, including mode matching techniques and finite element method).

2.2.1 Mode Matching

Mode-matching technique is a powerful numerical method to solve the electromagnetic field on

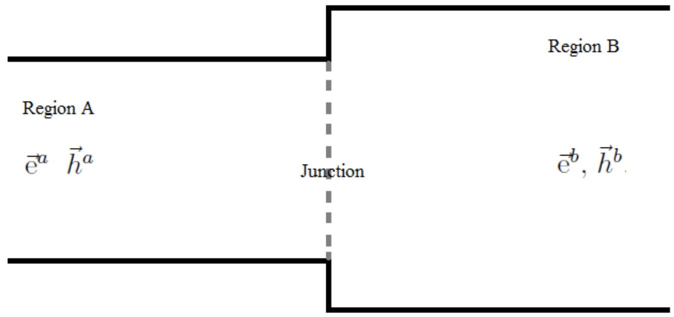

Figure 2.4: Mode matching schematic. The most simple structure consisting of the two wave propagation regions and the junction, where the boundary conditions are applied.

structures whose transitions can be expressed as a scattering matrix. In this structures, the total field can be described by the sum of infinite modes [22].

Let be A and B two uniform waveguides connected by the junction cross-section as shown figure 2.4. Let us also assume that the modes propagating in A and B are respectively $\vec{e}^a$, $\vec{h}^a$ and $\vec{e}^b$, $\vec{h}^b$. Then, the field in the junction is given by [23] [24]

$$\vec{E}_t^a = \sum_{n=1}^{\infty}(a_n^+ + a_n^-)\vec{e}^a \tag{2.17}$$

$$\vec{H}_t^a = \sum_{n=1}^{\infty}(a_n^+ - a_n^-)\vec{h}^a \tag{2.18}$$

$$\vec{E}_t^b = \sum_{n=1}^{\infty}(b_n^+ + b_n^-)\vec{e}^b \tag{2.19}$$

$$\vec{H}_t^b = \sum_{n=1}^{\infty}(b_n^+ - b_n^-)\vec{h}^b \tag{2.20}$$

where a_n and b_n are the n^{th} mode propagate in the waveguide A and B in the $+z$ or $-z$ directions, respectively. If we impose the continuity boundary condition into the cross-section S, we obtain

$$\sum_{n=1}^{\infty} P_{mn}^a(a_n^+ + a_n^-)\vec{e}^a = \sum_{n=1}^{\infty} A_{mn}(b_n^+ + b_n^-)\vec{e}^b \tag{2.21}$$

$$\sum_{n=1}^{\infty} B_{mn}(a_n^+ + a_n^-)\vec{e}^a = \sum_{n=1}^{\infty} P_{mn}^b(b_n^+ + b_n^-)\vec{e}^b \tag{2.22}$$

$$\sum_{n=1}^{\infty} C_{nm}^*(a_n^+ - a_n^-)\vec{h}^a = \sum_{n=1}^{\infty} B_{nm}^*(b_n^+ - b_n^-)\vec{h}^b \tag{2.23}$$

$$\sum_{n=1}^{\infty} A_{nm}^*(a_n^+ - a_n^-)\vec{h}^a = \sum_{n=1}^{\infty} P_{nm}^{b*}(b_n^+ - b_n^-)\vec{h}^b \tag{2.24}$$

where $m = 1, 2, ..., \infty$ and the coefficients P^a_{mn}, P^b_{mn}, A_{mn}, B_{mn} and C_{mn} are defined by

$$P^a_{mn} = \int_S \vec{e}^a \times h^{\vec{a}*}_m \hat{z} \, \mathrm{d}S \tag{2.25}$$

$$P^b_{mn} = \int_S \vec{e}^b \times h^{\vec{b}*}_m \hat{z} \, \mathrm{d}S \tag{2.26}$$

$$A_{mn} = \int_S \vec{e}^b \times h^{\vec{a}*}_m \hat{z} \, \mathrm{d}S \tag{2.27}$$

$$B_{mn} = \int_S \vec{e}^a \times h^{\vec{b}*}_m \hat{z} \, \mathrm{d}S \tag{2.28}$$

$$C_{mn} = \int_S \vec{e}^a \times h^{\vec{a}*}_m \hat{z} \, \mathrm{d}S \tag{2.29}$$

We can note that the output solution depends only on the input modes. Then, the solution for a single junction can be obtained by the truncation of the infinity series, ensuring the sufficient convergence. In general, around 100 modes are needed [25]. Finally, the total field on the structure is computed as the cascade of the all single junctions.

This method has limited applications. The most popular are waveguide discontinuities, horn antenas and resonator cavities. Nevertheless, it is a very fast method with low computational requirements.

2.2.2 Method of the moments

The most popular integral methods are the Electric Field Integral Equation (EFIE) and Magnetic Field Integral Equation (MFIE) methods. They enforce the convergence of the tangential electrical field boundary condition and of the tangential magnetical field, respectively. Commonly, they are solved by the Method of Moments (MoM), which computes the currents on the surfaces of objects. It is a efficiently technique for open radiation and scattering problems [22].

The field generated by a current can be defined by

$$E(\vec{r}) = \frac{1}{j\omega\varepsilon}(\bigtriangledown \bigtriangledown + k^2) \int J(\vec{r}) G(|\vec{r} - \vec{r'}|) \mathrm{d}\vec{r} \tag{2.30}$$

where J is the surface current density, k is the wavenumber, ω is the frequency in radians, ε is the dielectric constant and G is the Green's function [26] defined by

$$G(r) = \frac{\exp(-jkr)}{4\pi r}. \tag{2.31}$$

Then, the problem to be solved is

$$n \times \vec{E(\hat{r})}^{incident} = n \times \frac{1}{j\omega\varepsilon}(\bigtriangledown \bigtriangledown + k^2) \int J(\vec{r}) G(|\vec{r} - \vec{r\prime}|) \mathrm{d}\vec{r} \tag{2.32}$$

The solution of this integral equation is usually obtained through the finite elements technique. In this approximation each cell assumes a current distribution. This converts the integral equation in a matrix problem. The method expands the currents on the scattering object in a finite approximation of linear summation of pondered functions [27]. To begin with the calculation of coefficients by solving integral equations, the integral equation can be expressed as

$$g = Lf_a = L \sum_{\mathrm{i}=1}^{N} a_{\mathrm{i}} f_{\mathrm{i}} \tag{2.33}$$

where g is the source or excitation, L is a lineal operator, f_a the unknown currents, f_{i} are the functions that represent the currents and a_{i} are the ponderation coefficient. The representation of current function are basis functions such as pulses, star, triangles, trigonometrical or polynomial. They are chosen to derive efficient expressions for evaluating the fields. Anyway, solving these equations require time-consuming numerical methods, mostly for the matrix inversion. The method does not satisfy the boundary condition at every point, it only converges to the average of them.

The most commonly application is over conductor materials. This structure can be expressed as an infinite periodic array and they can be simplified using Fourier series. Dielectric problems require special considerations.

2.2.3 Finite elements Method

The Finite-Elements Method (FEM) is a numerical technique to solve partial differential equation problems in different disciplines. In particular, it can be applied to the electromagnetic field equations, where FEM solves the Maxwell equation in the frequency domain [22]. The full structure is divided in small cells, usually parallelepipeds, hexahedral or tetrahedral, allowing an accurate approximation to any geometry configuration. The most usual approach is to calculate the tangential field at each vertex to the cell and then interpolate in order to solve the other points. The analysis must be repeated at every required frequency [28].

Within this representation, the Maxwell's equations can be transformed into a matrix problem and solved using traditional numerical methods. Respect to the increase of accuracy of the method, commercial software use adaptative-mesh methods, i.e., iterative processes in which the mesh is automatically refined in critical regions. In order to minimize the use of time and computational resources, the initial mesh is rough. In the next iteration, in order to decrease the error, the mesh is refined in areas of high error to achieve the convergence goals.

We can understand the methodology in a better way, if we analyze a simple example as illustrated in figure 2.5. Let be $F : X \to \mathbb{R}$ the function we want to determine and $F'(x)$ an approximate function of $F(x)$. According to the Finite Element Method, the first step is to discretize the domain of the function in several cells, in this example 6 cells as shown 2.5(a). In the second step, we sample

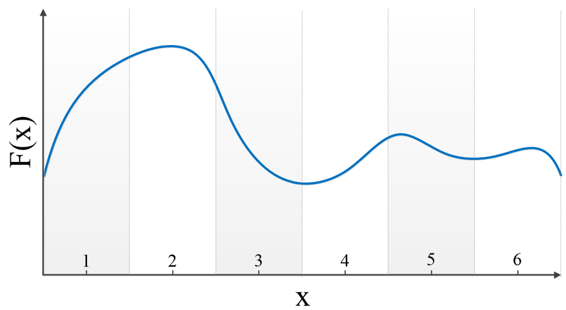

(a) Initial $F(X)$ function to determinate

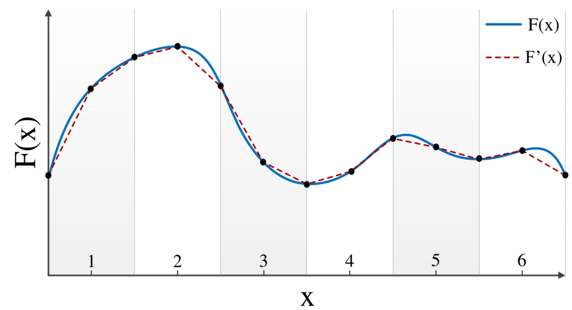

(b) Calculation of the approximate function $F'(X)$

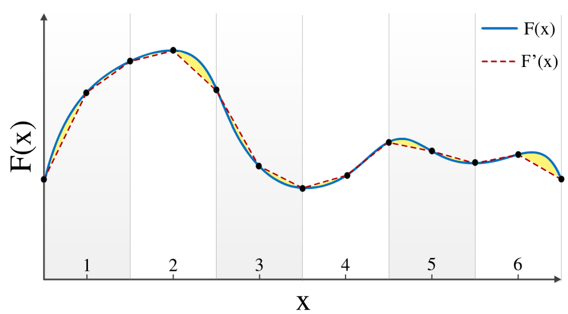

(c) Computation of the error between $F(X)$ and $F'(X)$

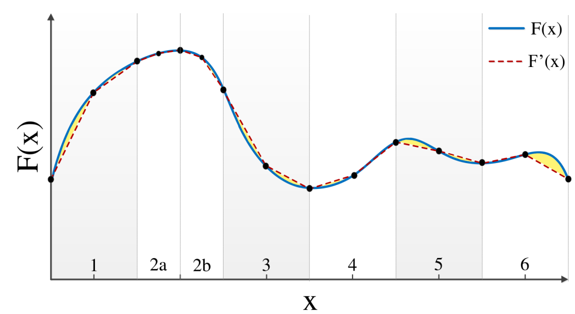

(d) Make the mesh denser in cell with high errors

Figure 2.5: Example of FEM methodology in 1D [29]. The blue line represents the function that we want to know, the red one the approximate function based on FEM methodogy and the yellow area represent the error between $F(X)$ and $F'(X)$.

the approximate function value in each vertex and intermedia point of the cells and interpole the function to obtain a linear function as shown 2.5(b). Then, since we solve using numerical methods, we compute the error between the function $F'(x)$ and the function $F(x)$ as shown in figure 2.5(c) in yellow areas. If any cell has a value greater than the allowable error, this should make the mesh denser as shown 2.5(d) [29].

2.3 Optical devices

The behavior of multiples devices can be described considering the quasioptical theory explained in section 2.1 and calculated in more accurate way using the techniques shown in 2.2. Nevertheless, each device is different due to have a special rol in the optical path, consequently they need a particular description. In this section we analysis the main components that are included in the optical system of ALMA Band 1, describing their main designer parameters and characteristics.

2.3.1 Dielectric lens

The diffraction phenomenon is directly related to the propagation of the wave. However, if the wavelength of the radiation is comparable to the system dimensions, diffraction dominates propagation, as is the case of Gaussian beams discussed in section 2.1. If the confocal distance is such that $z_c << z$, the diffraction is described by equation 2.13. A transformation that changes the propagation properties is required in order to collimated the beam. This transformation is provided by lenses and mirrors. This is equivalent to classical geometrical optics problems, but considering that in the present case the focus is a waist instead of a point. In this section we study lenses since they have been chosen to collimate the beam in the Band-1 optical system.

Lenses are passive devices whose performance is defined by its geometry and construction material. They have four main design features, the input and output surface shape, the relative permitivity and the distance from the feed source. There are many types of lenses, dielectric, metal-plate, waveguide, bootlace-type, phased array, dome and luneburg. In any case, the most common are the rotational dielectric lenses [30].

Quasioptical focusing approach

The focusing process can be analyzed from the quasioptical approach [19]. The general relationship relating the output and input ray position is given by

$$q_{out} = \frac{A \cdot q_{in} + B}{C \cdot q_{in} + D} \tag{2.34}$$

where we have considered the input-output reciprocity of the refocus elements, q is called the Gaussian beam parameter and the ABCD matrix is known as the transfer matrix. This matrix represents the effect of the element over the beam, it includes the diffraction in the propagation of the beam and the Snell law. If more than one element is in the optical path, the cascade effect will be considered. In other words, the resulting ABCD matrix will be the multiplication of each single transfer matrix, starting from the last one in the path. Below we describe some important transfer matrices.

For a beam traveling across a uniform medium the ray transfer matrix that describes the propagation is

$$\begin{bmatrix} 1 & \mathrm{d}/n \\ 0 & 1 \end{bmatrix} \tag{2.35}$$

where n is the refractive index and d the propagation distance.

For a beam passing through a spherical interface from medium 1 to medium 2, the ABCD matrix describing the propagation is

$$\begin{bmatrix} 1 & 0 \\ \frac{n_2-n_1}{n_2 \cdot R} & \frac{n_1}{n_2} \end{bmatrix} \tag{2.36}$$

where n_1 and n_2 are the refractive index for the medium 1 and 2 respectively, R is the radio of curvature and d the propagation distance.

Using a single curved refracting surface, there is a unique solution for equiphase output. To bifocal design can be useful one more degree of freedom using two refracting surface lens. The ABCD matrix for a bifocal thick lens, is defined by

$$\begin{bmatrix} 1+\frac{\mathrm{d}\cdot(n_2-n_1)}{n_2\cdot R_2} & \frac{\mathrm{d}\cdot n_1}{n_2} \\ -\frac{1}{f}-\frac{\mathrm{d}\cdot(n_2-n_1)^2}{n_1\cdot n_2\cdot R_1\cdot R_2} & 1+\frac{\mathrm{d}\cdot(n_1-n_2)}{n_2 R_2} \end{bmatrix} \tag{2.37}$$

where d is the lens thickness, R is the radius of curvature, n the refraction index and f the focus ($+f$ for concave surface and $-f$ for convex surface). Using the thin lens approximation, d $\rightarrow 0$, then the ABCD matrix can be written as

$$\begin{bmatrix} 1 & 0 \\ -\frac{1}{f} & 1 \end{bmatrix} \tag{2.38}$$

Finally, the transformed beam parameter has a waist radius w_{0out} at distance d_{out} from the transformer system are defined by

$$d_{out} = -\frac{(A d_{\text{in}} + B)(C d_{\text{in}} + D) + AC z_c^2}{(C d_{\text{in}} + D)^2 + C^2 z_c^2} \tag{2.39}$$

$$w_{out} = -\frac{w_{0\text{in}}}{\sqrt{(C\mathrm{d}_{\text{in}} + D)^2 + C^2 z_c^2}} \tag{2.40}$$

where A,B,C and D are the elements from a cascaded transfer matrix and the input Gaussian beam has a waist radius of w_{0in} at a initial distance to d_{in} from the transformer system.

General profile deduction

The necessary profile of the lens to collimate travelling beams can be deduced considering the Fermat's principle of least time and Snell's law of refraction. In this manner, the refocusing is produced in the lens surface. From the geometry described in figure 2.6, it can be demonstrated that the curved surface of any concave surface can be describe by

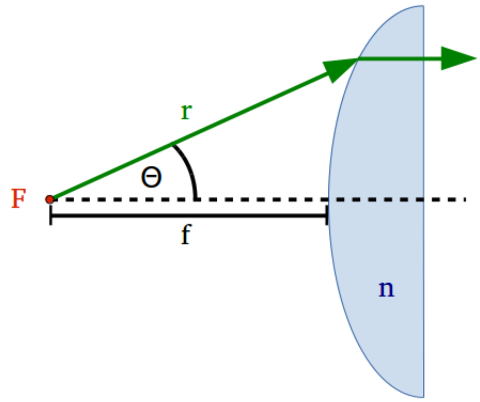

Figure 2.6: Geometry of a concave general lens.

$$r = f + n(rcos(\theta) - f) \tag{2.41}$$
$$\Leftrightarrow r = \frac{(n-1)f}{ncos(\theta) - 1}$$

where r and θ are the polar coordinates parameters, f is the focal distance and n the refraction index.

Herein, we concentrate on dielectric lenses with refraction index $n > 1$. In other words, the wave phase velocity inside the lens is less than the velocity in the free space. Moreover, if $n > 1$, equation 2.41 represents a hyperbola with its origin in f and eccentricity n [30].

Zoned Fresnel lens

A standard bi-hyperbolic lens can be a large structure depending on its design features that could produced assembly or mechanical difficulties. Furthermore, the long path, respect to the wavelength, produces appreciable absorptive loss and introduces considerable noise to the system.

In order to avoid these disadvantages, it is possible to reduce the thickness of the lens if an appropriate discontinuous shape is used, these kind of devices are called zoned lens. They are designed to produce a jump of a multiple of 2π radians in the ray path, at the designed frequency, between two adjacent zones . Therefore, the resulting wavefront is not affected by the shape variation [30].

A standard bi-hyperbolic lens is a frequency independent device. When zoning is applied it introduces a limitation in the bandwidth operation since only for the designed frequency the difference in the optical path between the zones is exactly 2π radians. Furthermore, the zoning produces regions with shadow which reduces the gain and increases the side-lobe level. For a zoned lens the relation between the bandwidth and the number of zones is

$$Bandwidth = \frac{25}{K-1}\% \tag{2.42}$$

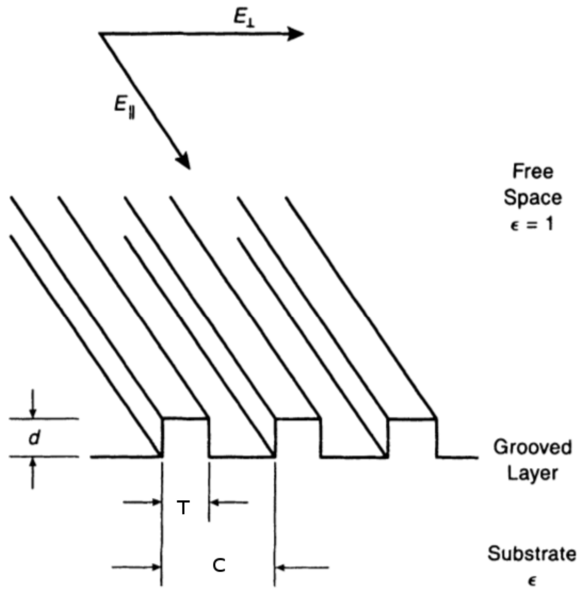

Figure 2.7: Antireflection coating using a grooved layer. d is the depth of the corrugation, T the width of the teeth, C the width of the corrugation ,ε the dielectric constant of the medium, $\vec{E_{\|}}$ the direction parallel E-field ans $\vec{E_{\perp}}$ the direction perpendicular one [19].

where K is the number of zones in the lens ($K = 1$ for an non-zoned lens). In polar coordinates the description of the surface shape in a zoned lens is

$$r = \frac{(n-1)f - (K-1)\lambda_0}{n\cos(\theta) - 1} \tag{2.43}$$

where r and θ are the polar coordinates term, f is the focus length and n the refractive index [30].

Anti-reflection coatings

The material to build a dielectric lens, has a refractive index different to the propagation medium, then reflection are produced. The reflection could produce several unwanted effects as power loss in the beam transmission, introducing additional noise or interference if it couples to undesirable direction. It can also produce standing waves, if there are multiples mismatches. Therefore, special treatments are required at the interfaces in order to reduce the reflection losses due to a change of medium.

Let be a plane wave traveling from a homogeneous medium A to another homogeneous medium B with refraction indexes n_a and n_b respectively, such that $n_a < n_b$. The reflection index, R, at normal incidence can be written as

$$R = \left(\frac{n_a - n_b}{n_a + n_b}\right)^2 \tag{2.44}$$

In order to reduce the reflection in the interface an extra layer of refraction index n_c, such that $n_a < n_c < n_b$, should be introduced. If the C layer is chosen appropriately, it provides a better matching between the mediums A-C and C-B, resulting on lower reflection than the A-B interface. The optimum value is $n_c = \sqrt{n_a \cdot n_b}$. The same effect can be achieved controlling the index of the material by geometry modifications as holes, protuberances or grooves in the basic material. Figure 2.7 shows a groove layer. It was demonstrated in [19] that for the interface between free space and a material of index $n = \sqrt{\frac{\varepsilon}{\varepsilon_0}}$ and dielectric constant ε, the best depth to a groove layer is defined by

$$d = \frac{\lambda_0}{4\sqrt{n}} \tag{2.45}$$

and the best ratio $f = T/C$ between the width of teeth T and the corrugation C is given by

$$f_{\|} = \frac{\sqrt{\varepsilon} - 1}{\varepsilon - 1} \tag{2.46}$$

$$f_{\perp} = \frac{\sqrt{\varepsilon}(\sqrt{\varepsilon} - 1)}{\varepsilon - 1} \tag{2.47}$$

where $f_{\|}$ is the ratio to the electromagnetic field parallel to the grooves and $f_{\perp}$ the perpendicular one. The differences to the parallel and perpendicular direction are explained since the impedance depends on the geometry in the path.

Grooves layers are widely used since they are very simple to machine on plastics materials. Nevertheless, they introduces anisotropy, astigmatism and phase problems [31], whose impact should be assessed for each design .

Dielectric characterization

As mentioned in the previous sections, the fabrication material of the lens has a fundamental role in its operation, since defined the necessary optical path in the refocusing elements, the noise contribution of the devices and make it necessary the use of anti-reflection coating. Consequently, it is important discuss about the definition of dielectric materials and obtaining their electromagnetic characteristics.

The dielectric materials have the propriety to be polarized [2] when an electric field is applied. Therefore, the total displacement flux is defined by

$$\vec{D} = \varepsilon_0 \vec{E} + \vec{P} = \varepsilon_0 \vec{E} + \varepsilon_0 \chi \vec{E} = \varepsilon \vec{E} \tag{2.48}$$

[2] It is referred to the internal property of some materials to orientate their charges creating dipoles.

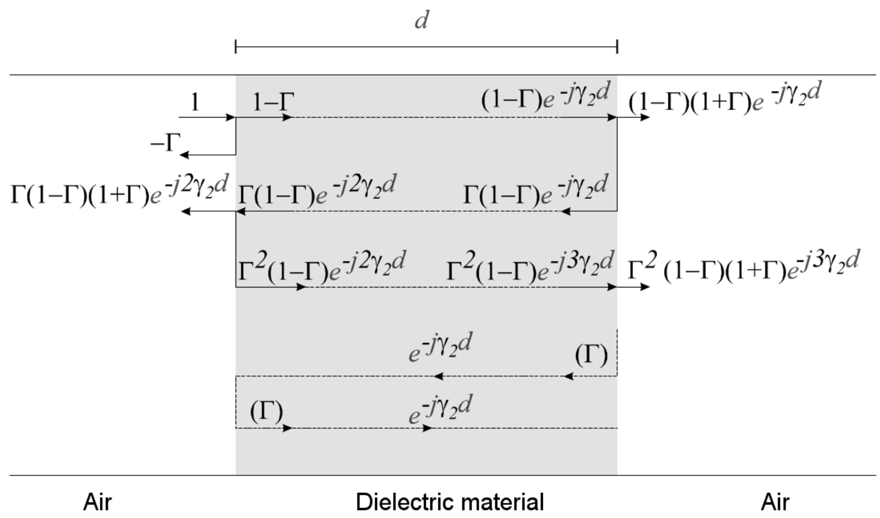

Figure 2.8: Waveguide multi-reflections model.

where ε_0 is the dielectrical constant in the vacuum, $\vec{P}$ is the polarization and χ the susceptibility when the medium is linear. Using the Maxwell's curl equation for $\vec{H}$ we obtain

$$\bigtriangledown \times \vec{H} = j\omega\vec{D} = j\omega(\varepsilon^{'} - j\varepsilon^{''})\vec{E} = \varepsilon^{'}(1 - j \cdot \tan\delta)\vec{E} \tag{2.49}$$

where ω is the angular frequency, $\varepsilon^{'} = \varepsilon_r\varepsilon_0$ is the real part to the dielectric constant, ε_r is the material relative dielectric constant and $\tan\delta = \varepsilon^{''}/\varepsilon^{'}$. This means that to characterize the electromagnetical behavior, we need to know the relative dielectric constant and the loss tangent $\tan\delta$ [3].

When using industrial materials for the construction of lenses, it is necessary to take into acount bach-to-bach variations. Therefore, it is necessary to characterize each block that will be used in the fabrication of the lens.

Depending on the frequency range of study, diverse techniques have been developed in order to characterize completely the electromagnetical properties of materials. Here we describe the dielectric characterization in rectangular waveguides using a multi-reflection model [3] [32]. Other methods can be reviewed in [33] and [34].

The dielectric characterization using a rectangular waveguide has the advantage of providing good accuracy in a reasonably simple setup, avoiding spurious effects. Moreover, the full bandwith can be measured in only one step. The main disadvantage is that it requires a slab of the studied material that is loaded into the waveguide. Therefore, it is an invasive method and it cannot be implemented into a device that has already been built.

Let us consider the multiples reflection produced by a change of medium as shown in figure 2.8. Then, the total reflections and transmission, assuming that only the fundamental mode is propagating, are defined by

$$\rho = -\Gamma + \frac{(1-\Gamma)(1+\Gamma)}{\Gamma}\sum_{n=1}^{\infty}(\Gamma^2 \mathrm{e}^{-j2\gamma_2 \mathrm{d}})^n = \frac{-\Gamma\left(1-\mathrm{e}^{-j2\gamma_2 \mathrm{d}}\right)}{1-\Gamma^2\mathrm{e}^{-j2\gamma_2 \mathrm{d}}} \tag{2.50}$$

$$\tau = (1-\Gamma)(1+\Gamma)\mathrm{e}^{-j\gamma_2 \mathrm{d}}\sum_{n=1}^{\infty}\left(\Gamma^2 \mathrm{e}^{-j2\gamma_2 \mathrm{d}}\right)^n = \frac{(1-\Gamma)(1+\Gamma)\mathrm{e}^{-j\gamma_2 \mathrm{d}}}{1-\Gamma^2\mathrm{e}^{-j2\gamma_2 \mathrm{d}}} \tag{2.51}$$

where d is the length of the waveguide. The wave propagation number, γ, is defined by

$$\gamma = \beta - j\alpha = k_0\sqrt{\Lambda\varepsilon_r} - \frac{jk_0 tan(\delta)}{2\Lambda}\sqrt{\Lambda\varepsilon_r} \tag{2.52}$$

$$\Lambda = 1 - \frac{\pi^2}{(ak_0)^2\varepsilon_r} \tag{2.53}$$

$$k_0 = \omega\sqrt{\varepsilon_0\mu_0}$$

where ε_r is the dielectric constant of the studied material, μ_0 and ε_0 are the permeability and the dielectric constant of vacuum, respectively. The total transmission and reflection are measured in two-port configurations using the S-parameters coming from a Vector Network Analyzer (VNA), accordingly $\gamma = S_{11}$ and $\tau = S_{21}$.

Having already established the multi-reflection model, the first step to implement it consists on choosing a waveguide to cover the appropriate bandwidth. The cut-toff region of the waveguide can be computed using

$$f_n^{min} = \sqrt{n^2 + \frac{\mathrm{d}}{a}^2}\frac{c}{2\mathrm{d}\sqrt{\varepsilon_r}} \tag{2.54}$$

$$f_n^{max} = \sqrt{\left(n+\frac{1}{2}\right)^2 + \frac{\mathrm{d}}{a}^2}\frac{c}{2\mathrm{d}\sqrt{\varepsilon_r}}$$

where $n = 0, 1, 2, ..$ when $\mathrm{d} = 2n\pi$, c is the speed of light in vacuum and ε_r the relative dielectric constant. Then, the empty waveguide, of known dimensions, must be measured in order to estimate the attenuation produced by the walls. The relation between the S_{21} parameter and the attenuation coefficient is

$$|S_{21}^{empty}| = \mathrm{e}^{-\alpha_m \mathrm{d}}. \tag{2.55}$$

The next step, supposing that the instrument calibration is well done in the input and output of the waveguide, consists on filling the waveguide with the material to be characterized in order to measure the reflection $S_{11}^{load\mathrm{WG}}$ and transmission coefficient $S_{21}^{load\mathrm{WG}}$. Finally the values of ε_r and $\tan\delta$ can be determined by fitting the multi-reflection model to the measured data.

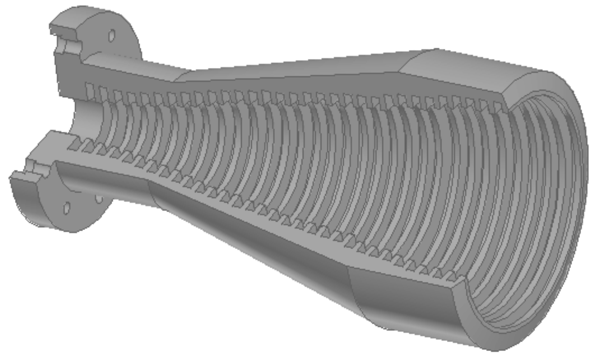

Figure 2.9: Corrugated horn antenna.

2.3.2 Horn antenns

In order to feed the optical system using beam with the characteristics shown in section 2.1, a horn antenna can be used. Horn antennas are aperture devices that allow the electromagnetic transition from the waveguide to free space. This transition uses a series of cross-sections that connect the aperture to the waveguide. They are used for an ample range of applications from MHz to THz. Commonly, horn antennas are meant to feed the reflector antennas on radio-astronomy, satellites and communication systems. Additionally, horns are used for calibration of high-gain antennas.

The shape of horn antennas depends on the characteristics required for its design objectives, gain, radiation pattern, efficiency and impedance. According to the waveguide used to fabricate the horn, the most common are rectangular and conical. In many applications where radiation pattern requirements are not too demanding, the profile is usually just a smooth straight line. Nevertheless, the best performance is achieved using corrugated horns as exemplified in figure 2.9.

Corrugated horns are characterized by a profile made up of teeth and grooves of variable depth and width as shown in the figure 2.10. They produce beam patterns with excellent performance that includes good symmetry, low side-lobes and low cross-polarization with a wide bandwidth. The purpose of the corrugations is to provide a surface to support the propagation of hybrid modes. This characteristics allow to increase the aperture efficiency from 50-60% to 75-80% in reflector antennas, which is a highly desirable characteristic in satellital, radio-astronomical and, currently, in communication systems [20].

In recent years, due to the usage of computational numerical control (CNC) milling machines and improvements in electroforming techniques, in the manufacturing process has allowed more sophisticated corrugated horn, with smaller dimensions and better performance [35].

Hybrid mode

Let us consider the Maxwell's equation in cylindrical coordinates

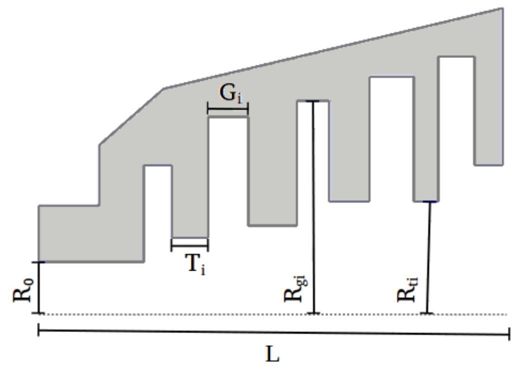

Figure 2.10: Main parameters defining a corrugated horn. R_0 is the input waveguide radius, $R_{g\mathrm{i}}$ is the groove radius, $R_{t\mathrm{i}}$ is the teeth radius, T_i is the teeth width, G_i is the groove width and i is the corrugation number.

$$E_\rho = \frac{-j}{k_c^2}\left(\beta\frac{\partial E_z}{\partial \rho} + \frac{\omega\mu}{\rho}\frac{\partial H_z}{\partial \phi}\right) \tag{2.56}$$

$$E_\phi = \frac{-j}{k_c^2}\left(\frac{\beta}{\rho}\frac{\partial E_z}{\partial \phi} - \omega\mu\frac{\partial H_z}{\partial \rho}\right) \tag{2.57}$$

$$H_\rho = \frac{j}{k_c^2}\left(\frac{\omega\varepsilon}{\rho}\frac{\partial E_z}{\partial \phi} - \beta\frac{\partial H_z}{\partial \rho}\right) \tag{2.58}$$

$$H_\phi = \frac{-j}{k_c^2}\left(\omega\varepsilon\frac{\partial E_z}{\partial \rho} + \frac{\beta}{\rho}\frac{\partial H_z}{\partial \phi}\right) \tag{2.59}$$

where $k_c^2 = k^2 - \beta^2$ is the cutoff wavenumber, E is the electrical field, H is the magnetical field and ρ, ϕ and z are the cylindrical coordinates components, according to figure 2.11. Moreover, we assume that the wave is propagating in the $+z$. A complete deduction can be found in [3].

When we impose that either $E_z = 0$ or $H_z = 0$, the result is the solutions of the waveguide equation inside a waveguide. A smooth waveguide can only support pure Transverse Electrical (TE) or Transverse Magnetic (TM) modes, while corrugated waveguides also support hybrid modes.

The hybrid mode is a mixture of TE_{nm} and TM_{nm} modes of the form $\sum_n \sum_m \gamma_{E_{nm}} \cdot TE + \gamma_{M_{nm}} \cdot TM$, where γ is a parameter called the mode-content factor. In addition, if the reactances

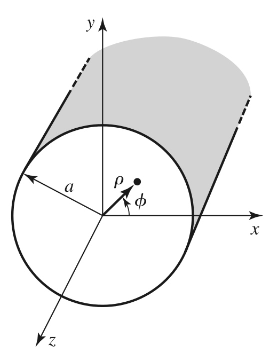

Figure 2.11: Cilindrical waveguide model [3].

$X_\phi \to 0$ and $X_z \to \infty$, we obtain the balanced hybrid condition. This condition allows the TE and TM components to propagate together as a single hybrid mode with a common velocity.

All in all, the hybrid modes under balance hybrid condition can be described in the following equations

- HE hybrid modes

$$E_{xmn} = \frac{\sqrt{2Z_0}}{R\sqrt{\pi}} \frac{J_{m-1}\left(\frac{p_{mn}\cdot\rho}{R}\right)}{J'_{m-1}\left(p_{mn}\right)} \cos((m-1)\phi)\mathrm{e}^{-j\beta z} \tag{2.60}$$

$$E_{ymn} = \frac{\sqrt{2Z_0}}{R\sqrt{\pi}} \frac{J_{m-1}\left(\frac{p_{mn}\cdot\rho}{R}\right)}{J'_{m-1}\left(p_{mn}\right)} \sin((m-1)\phi)\mathrm{e}^{-j\beta z} \tag{2.61}$$

- EH hybrid modes

$$E_{xmn} = \frac{\sqrt{2Z_0}}{R\sqrt{\pi}} \frac{J_{m-1}p_{mn}\rho}{J'_{m-1}p_{mn}R} \cos((m+1)\phi)\mathrm{e}^{-j\beta z} \tag{2.62}$$

$$E_{ymn} = \frac{\sqrt{2Z_0}}{R\sqrt{\pi}} \frac{J_{m-1}p_{mn}\rho}{J'_{m-1}p_{mn}R} \sin((m+1)\phi)\mathrm{e}^{-j\beta z} \tag{2.63}$$

where Z_0 is the impedance in the free space, R is the waveguide radius, J_n is the Bessel function of the first kind, J'_m is the derivative Bessel function, p_{mn} are the m-th root of J_m, $\beta_{nm} = \sqrt{k - \left(\frac{p'_{mn}}{a}\right)}$, and p'_{mn} are the roots of the m-th J'_m.

The dominant hybrid mode in a corrugated waveguide is the HE_{11}, defined by

$$E_x = \left(\frac{2.405r}{R}\right)\left(A_1 \cdot J_0 - A_2 \cdot J_2 \frac{X-Y}{kR} \cdot cos(2\phi)\right) \tag{2.64}$$

$$E_y = A_2 \cdot J_2 \frac{2.405r}{R} \frac{X-Y}{kR} \cdot \sin(2\phi) \tag{2.65}$$

where $J_0(k\rho)$ and $J_2(k\rho)$ are Bessel functions of the first kind, k is the free space wave-number, A_1 and A_2 are the amplitude coefficients, X and Y are the impedance and admittance at the boundary $r = R$, defined by

$$X = -j\frac{E_\phi}{H_z Z_0} \tag{2.66}$$

$$Y = j\frac{H_\phi}{E_z Z_0} \tag{2.67}$$

Notice that in general, a corrugation of depth $d = R_t - R_g$ has a reactance, defined by

$$X_s = Z_0 \frac{2\pi d}{\lambda} \tag{2.68}$$

Table 2.1: Main ALMA antenna parameters.

Parameter	Value
Focal Beam f/D	8
Primary aperture D	12 m
Focal length of primary(f)	4.8 m
Secondary aperture (d)	0.75 m
Secondary eccentricity (e)	1.10526
Distance between primary and secondary focus ($2c$)	6.177 m
Antenna magnification (M)	20

We can understand how the field is distributed inside a corrugated waveguide and how it achieves the balance hybrid condition in its aperture, when there are enough corrugations per wavelength for make $X = 0$ at $\rho = R$. If corrugation teeth T is narrow and $\rho = \lambda/4$, they are a short circuit connected to an open circuit at $\rho = R$. It does not have axial current, so $Y = 0$ or $X_z \to \infty$ [30].

As shown in equation 2.68 the reactance of the horn depends on the operation frequency, or in other words, it has a limited bandwidth. In order to operate in a more extensive range of frequency, the design needs varying corrugation depths. A usual technique consisting in use corrugations from d $\approx \lambda/2$ to d $\approx \lambda/4$, starting from the input waveguide to achieve a good performance [19].

2.3.3 Cassegrain antennas

Cassegrain antennas are one of the most popular reflector antennas because they increase the effective focal length but keeping compact configurations. They consist of a primary paraboloid reflector (also called main dish) and a hyperboloid secondary (or sub-reflector) as it can be seen in figure 2.12. Analyzing the Cassegrain configuration in transmission mode, the secondary transforms the narrow beam from the feed to illuminate the primary reflector which is much larger. The collimating properties are obtained by putting one of the focus from the sub-reflector at one focus of the main parabolic dish, it is the virtual focus F_1. Moreover, F_2, the second focus of the sub-reflector, should be located at the receiver optics focus, a real focus point [30]. The main parameters that define the ALMA 12-meters antennas are shown in table 2.1 [13]. Notice that the magnification factor depends on the sub-reflector eccentricity by the well known geometrical relation

$$M = \frac{1 + \mathrm{e}}{1 - \mathrm{e}} \tag{2.69}$$

Two-reflector antennas have the advantage of providing an additional degree of freedom when compared to prime-focus antennas. In the two-reflector antennas, we can give a position of F_2 closer to the crossing of the optical axis and the main sub-reflector in order to decrease the blockage of the feed and increase the aperture efficiency. Nevertheless, the sidelobes produced by Cassegrain antennas are not remarkably low. Consequently, the design should be considered carefully to control the dish diffraction and the radiation pattern of the feed antenna.

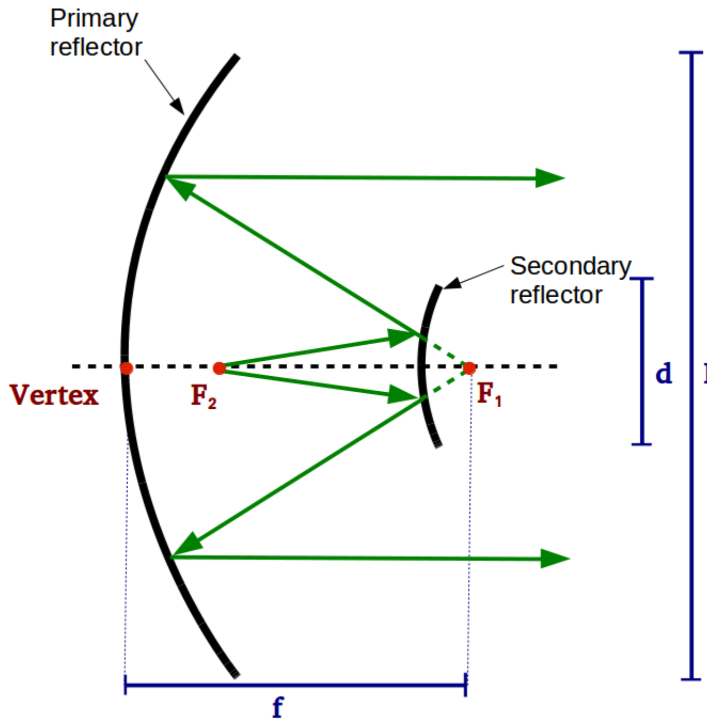

Figure 2.12: Cassegrain geometry. D is the primary and d secondary aperture, f the focal length of primary, F_1 primary focus and F_2 the secondary focus (it may be positioned behind the Vertex).

Aperture Efficiency

Aperture efficiency is defined as the ratio of the effective collecting area of the antenna to its geometric area [19]. For a reflector antenna the effective collecting area is the sub-reflector, subtending a solid angle Ω, and the principal dish is the geometric area of the antenna. The solid angle subtended for a sub-reflector of angle θ_m is defined by

$$\Omega = \int_{\Omega} \partial\omega = \int_0^{2\pi}\int_0^{2\theta_m} \sin\theta \ \mathrm{d}\theta\mathrm{d}\phi = 2\pi(1-\cos\theta_m) \tag{2.70}$$

where $\mathrm{d}\omega$ is the differential of solid angle.

The aperture efficiency can be decomposed in several efficiency components, such as surface, blockage, defocusing, radiation, spillover, polarization, amplitude and phase errors. Here we describe in detail the last four efficiencies, directly related to the illumination in the sub-reflector and the used in ALMA specifications [36].

Spillover efficiency represents the power intercepted by the secondary reflector in comparison to the total power radiated by the source. It is defined through

$$\eta_{spillover} = \frac{\int_{\Omega} |E_{total}|^2 \mathrm{d}\omega}{4\pi}. \tag{2.71}$$

Amplitude efficiency, also called taper or illumination efficiency, expresses the power lost by a signal since the field does not have a uniform distribution over the sub-reflector. It can be calculated as

$$\eta_{amplitude} = \frac{[\int_{\Omega} |E_{copolar}| \mathrm{d}\omega]^2}{\Omega \int_{\Omega} |E_{copolar}|^2 \mathrm{d}\omega}. \tag{2.72}$$

The polarization efficiency ratio expresses the power used in co-polarization fields compared to the total power. It is defined by

$$\eta_{polarization} = \frac{\int_{\Omega} |E_{copolar}|^2 \mathrm{d}\omega}{\int_{\Omega} |E_{total}|^2 \mathrm{d}\omega}. \tag{2.73}$$

The phase efficiency quantifies any phase error in the pattern over the sub-reflector. It can be calculated by

$$\eta_{phase} = \frac{|\int_{\Omega} E_{copolar} \mathrm{d}\omega|^2}{[\int_{\Omega} |E_{copolar}| \mathrm{d}\omega]^2}. \tag{2.74}$$

Finally, the aperture efficiency considering the described ratio efficiencies is

$$\eta_{aperture} = \eta_{spillover} \cdot \eta_{amplitude} \cdot \eta_{polarization} \cdot \eta_{phase}. \tag{2.75}$$

As we can appreciate from the definition of the spillover and the amplitude efficiencies, there is correlation between them for usual antennas. The best amplitude efficiency is achieved when the energy density on the sub-reflector is constant. Nevertheless, for a gaussian beam, if we achieve a nearly uniform illumination we also have a great loss of energy as shown in figure 2.13(a). On the other hand, the maximum spillover efficiency is achieved when the total energy is caught by the sub-reflector. High values of spillover, however, means that there exists high concentration of energy in the center of the sub-reflector, resulting in poor energy distribution over the sub-reflector as shown figure 2.13(b). In order to optimize the aperture efficiency an intermediate value should be chosen. This point will be crucial in the designs presented in this thesis.

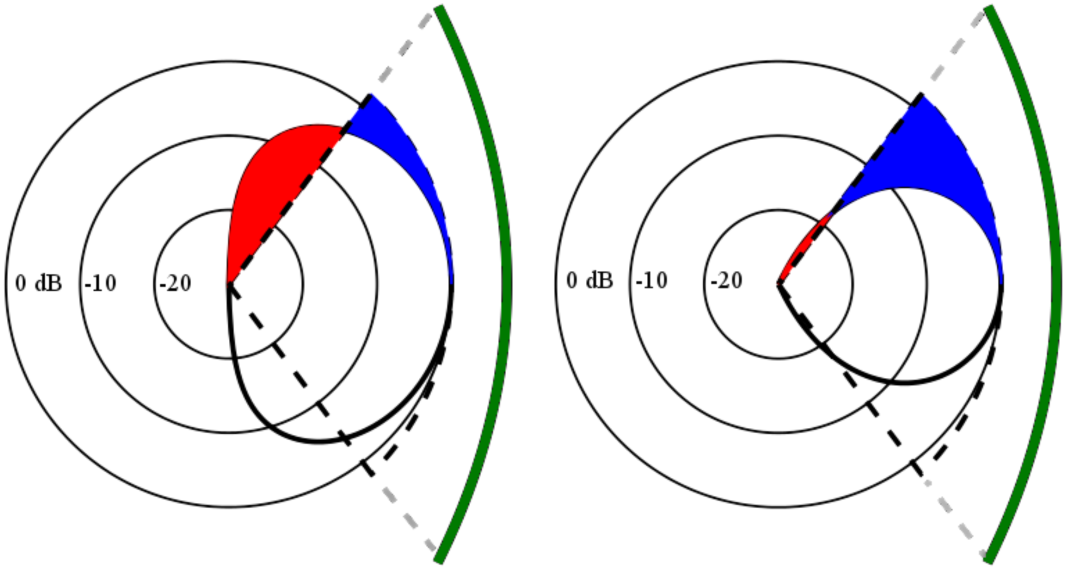

(a) (b)

Figure 2.13: Amplitude and spillover efficiency in two different radiation patterns. Blue areas represent the amplitude loss and red ones the spillover loss, while the green line is the collector dish of the main antenna. (a) Radiation pattern with high spillover loss and (b) radiation pattern with high amplitude loss [37].

Spillover and amplitude efficiencies in Gaussian radiation patterns can be described by the edge taper T_e (discussed in section 2.1.3). In fact, they can be written as

$$\eta_s = 1 - exp(-2\alpha) \tag{2.76}$$

and

$$\eta_a = \frac{2 \cdot (1 - exp(-\alpha))^2}{\alpha \cdot (1 - exp(-2\alpha))}, \tag{2.77}$$

respectively, where $\alpha = (r_a/w_a)^2 = 0.115 \cdot T_\mathrm{e}$ dB, r_a is the projected radius at the sub-reflector and w_a is the beamsize at the subreflector. In figure 2.14 the aperture, spillover and amplitude efficiencies are calculated according to the edge taper. We have assumed that all the others efficiences components are equal to 1.

Noise Temperature

The noise temperature expresses the noise contribution of all the components in the desired signal. It includes the addition of noise to the original signal from diverse sources such as the sky, the antenna and the thermal noise of analog components [22]. The total noise contribution can be defined by

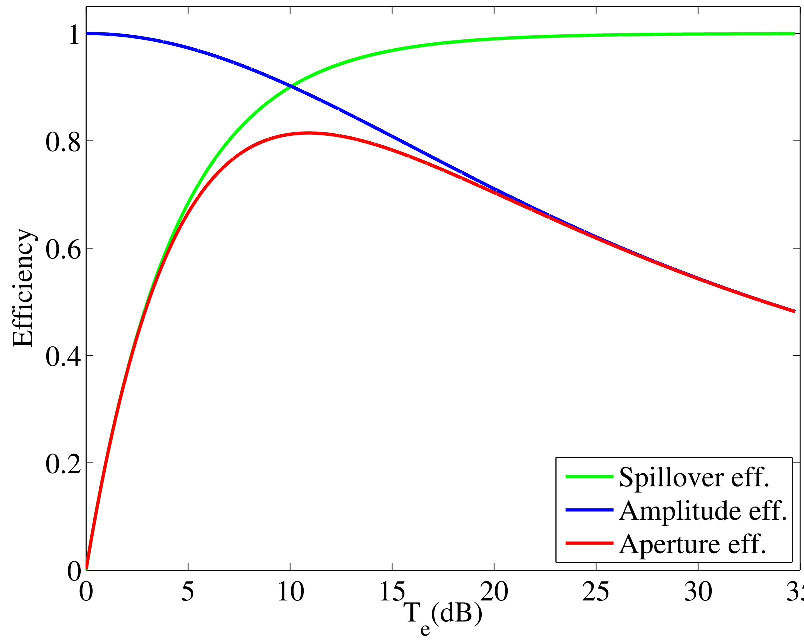

Figure 2.14: Aperture, spillover and amplitude efficiencies calculated according to the edge taper. It can be noted that there is a trade-off between maximum spillover and amplitude efficiency. Aperture efficiency reaches a maximum around 10 dB.

$$T_{sys} = T_{sky} + T_{ant} + T_{rec}, \tag{2.78}$$

where T_{sky} represent the noise including due to the atmospheric temperature and the CMB, T_{ant} represent the scattered and spillover temperatures of the antenna, T_{rec} the total noise temperature of the receiver. Moreover, T_{rec} depends on the temperatures and gains of any single component according to

$$T_{rec} = T_1 + \sum_{\mathrm{i}=2}^{N} \frac{T_{\mathrm{i}}}{\Pi_{j=1}^{\mathrm{i}-1} G_j}, \tag{2.79}$$

where T_{i} is the noise temperature of the i component, G_j the corresponding gain and T_1 indicates that the first devices will be the noise reference point.

2.4 Conclusion

In brief, this chapter we have presented the theoretical framework that describes and support the design, construction and characterization of the optical system for Band 1.

Chapter 3

Modeling and design

This chapter presents the design process of the prototypes of the horn and lens. First, a discussion of the elements that make the optical system and their mechanical limitations are presented. Later, the complete iterative design process of two horn antennas and three one-zoned lenses is shown. Regarding the horn antennas, the profile optimization, the resulting construction parameters and the analysis of the simulated radiation pattern are presented. The lens design includes the optimization process of the mechanical parameters and the analysis of the simulated radiation pattern of the horn and the lens subsystem (including the calculated efficiencies and noise temperature). Finally, for the best design a complete study of the effect of the infrared filter and a compatibility analysis of the 7 and 12-meters antennas is presented.

3.1 Baseline design of the optical system of ALMA Band 1

Figure 3.1 illustrates the mechanical design of the optical assembly consisting on a lens, holder of the lens, two infrared filter and a cold feed-horn antenna. The top device is a low-loss HDPE bi-hyperbolic one-zoned lens with anti-reflection grooves machined into both sides of the device. The lens diameter is set to the maximum possible 190 mm to minimize truncations of the lens without interfering with the water vapor radiometer. For this purpose it has been considered a minimal distance of 2.5 mm between the holder and the water-vapor radiometer. This is equivalent to a maximum distance between the top of the horn to the center of the lens of 190 mm. Moreover, the mount of the lens was modified to fully use the available space as shown in figure 3.2. The next device is the holder of the lens, it is symmetric regarding the optical axis which is tilted 87.52° from the top of the cryostat. The optical axis is defined between the center points of the horn and the cryostat hole.

In the middle of the optical system there are two infrared filters. They are a thin Gore-tex membrane and a grooved surface of the PolyTretaFluoroEthylene (PTFE) at 15 and 110 K stages, respectively. They have been provided by ALMA and designed by the Institute de radio Astronomie Millimétrique (IRAM). Their properties are summarized in table 3.1 [38]. They were designed to

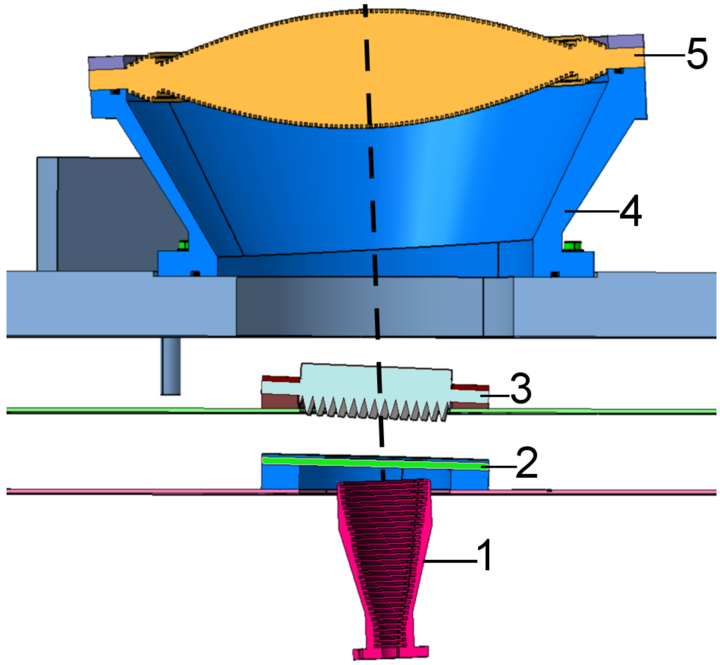

Figure 3.1: Cross-section of the baseline optical design. 1: Spline profile corrugated horn antenna, 2: 15 K infrared filter, 3: 110 K infrared filter, 4: lens holder and 5: one-zoned lens.

operate in the old frequency range of Band 1, 31.3–45 GHz, hence some inappropriate operation could be expected for frequencies higher than 45 GHz. Furthermore, the filters include top and bottom metal rings that contribute to the thermal equilibrium over the shields. The apertures of these rings are offset to the optical axis as shown in the figure 3.3, resulting in an small unobstructed path of only $1.98{\cdot}w_0$ at the lower frequency. Correspondingly, in order to avoid truncation in the infrared filters rings, the position of the horn is set to the minimal allowed distance, 4.51 mm to the 15 K infrared filter, or equivalent to 5.23 mm in the propagation axis. It is as close as possible without risking mechanical overlap during cool-down.

There is one last important point to consider in the design of the horn. If a standard corrugated feed horn is used, as presented in [13], the resulting narrow flare angle of the device will make it difficult (if not impossible) to machine it as a single piece. Moreover, it can be too long to be included easily in the cryostat. Accordingly, we propose to use a more compact configuration, a spline profiled corrugated horn. This device avoids the use of a more complex fabrication technology, and may be directly machined as a single piece on a CNC lathe if some mechanical constraints are included. Particularly for a horn of waveguide radio of 3.35 mm, as the one necessary for Band 1, it

Table 3.1: Main parameters of infrared filters.

Filter stage	Material	Distance to cryostat	Aperture radio	Thickness	Antireflection layer
15 K	Gore-tex	72.70 mm	20.00 mm	3.00 mm	None
110 K	PTFE	44.56 mm	30.50 mm	5 mm (central slab) 3.5 mm (grooves)	Triangular grooves

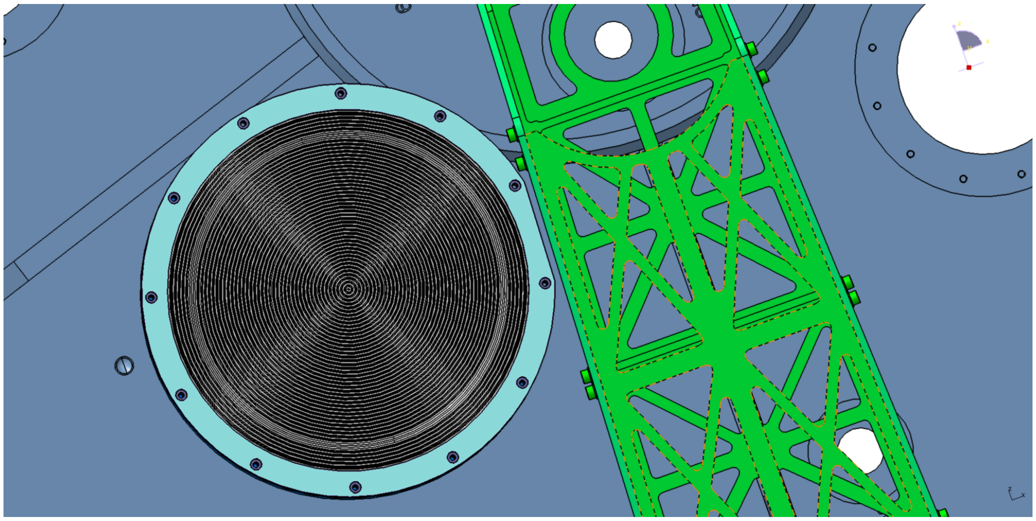

Figure 3.2: Top view of lens and water-vapor radiometer mounted on ALMA cryostat. The distance between the holder and the water-vapor radiometer is of 3.6 mm when the distance between the top of the cryostat to the center of the lens is 164 mm.

is required a maximum corrugation depth of 3.2 mm to provided enough space to the cutting tools. Moreover, it should be considered a total length less than 80 mm in order to avoid tool vibration during machining.

3.2 First horn design

The profile of the horn was optimized for achieving the desired performance using a mode matching software, Microwave Wizard, and a genetic algorithm. The optimization parameters are the depth, width and number of corrugations. A beam-waist of about 9.4 mm is required to achieve frequency independent illumination while minimizing truncation through the window of the cryostat and infrared filters according to the quasi-optical analysis. The characteristics of an ideal Gaussian feed were determined by optimizing a quasi-optical model of the Band 1 optics. The profiled horn was then optimized to match the Gaussian feed and achieve low cross-polarization and low reflected power. Additionally, different goals were used to force a good symmetry of the radiation pattern, the difference both in phase center location (PCL) and 10 dB point between the E and H planes

Table 3.2: Main optimization goals between 33-52 GHz to first spline profile corrugated horn design.

Freq(GHz)	33	35	38	42	42.5	44	47	50	52
10-dB point (°)	19.1	18.0	16.6	15.4	14.8	14.3	13.4	12.6	12.1
PCL (mm)	5.0	5.6	6.4	7.7	8.2	9.8	10.1	11.2	12.0
Crosspolarization (dB)	<–30	<–37							<–30
Reflected power (dB)	<–25	<–30							<–25
10-dB point difference E/H(°)	< 1	<0.3							<1
PCL difference (mm)	<2	<1							<2

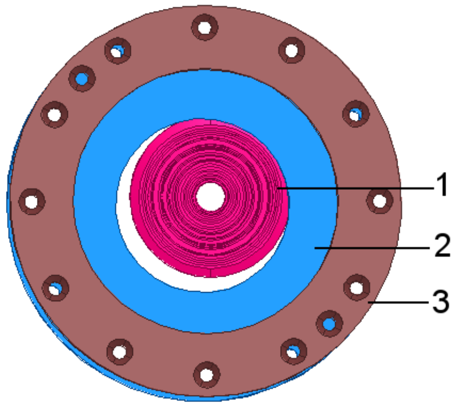

Figure 3.3: Top view of a horn of 15.84 mm aperture radio and infrared filter showing the offset of the infrared filters. 1: Spline profile corrugated horn antenna, 2: top metal ring of 15 K infrared filter, 3: top metal ring of 110 K infrared filter.

were set to be small. The optimization goals over the radiated beam pattern are shown in table 3.2. Using these optimization goals, after several weeks of optimization, a good horn was achieved. Its profile is shown in figure 3.4, while the main parameters are presented in table 3.3.

The resulted profile is a compact horn, with a length of 10 central wavelength. The profile does not follow any well known function and does not have a monotone behavior. The corrugations are less deep than a standard horn having smooth changes, less than 0.6 mm between two correlative corrugations, providing a good match impedance to propagate the modes that allow the Hybrid condition explained in 2.3.2.

The design was validated using HFSS. Simulations with 50 MHz resolution were conducted to study reflection loss. Figure 3.5 shows a comparison between HFSS and Microwave Wizard results. It is observed that the reflected power has a low level below –28 dB according to HFSS estimation and –29 dB according to MWW in the frequency range from 35–52 GHz. The structure of the curves are very similar with an average difference less than 1.5 dB.

Furthermore, a comparison between HFSS and MWW far-field radiation patterns at different frequencies are presented in figure 3.6. They are highly similar down to –20 dB with a maximum difference of 3° in the shoulder of the curve. The curves of cross-polarization exhibit greater variation

Table 3.3: Main mechanical parameters of horn design.

Horn design parameter	Value
Input circular WG radius ($R0$)	3.35 mm
Horn aperture radius ($r31$)	31.62 mm
Horn total length	70 mm
Number of corrugations	31
Width of corrugation	0.90 mm
Width of gap (G)	1.22 mm
Depth of gap ($R\mathrm{i} - r\mathrm{i}$)	1.53–2.97 mm

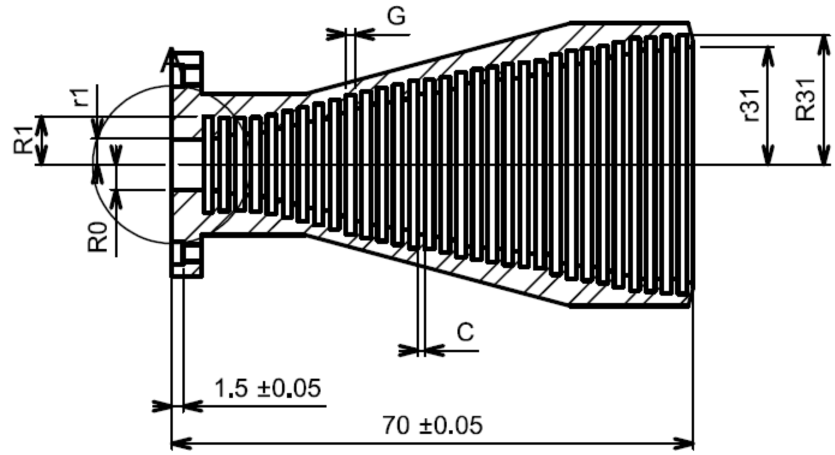

Figure 3.4: First spline profile corrugated horn design.

in shape, nevertheless, their maximum are similar with a difference lower than 5 dB and all of them better than –34 dB. It is important to note that, due to the different simulation methodologies, MWW should be more accurate that HFSS as a result of the convergence of all its simulations. In HFSS, the time-consuming and high computational resources required make difficult every extra iteration.

The main simulated parameters of the beam patterns, including the cross-polarization level, shoulders, symmetry, beam waist and phase center location, are summarized in table 3.4. The beam pattern presented good symmetry characteristics, a good PCL behavior, a low side lobe and crosspolar level. Although the side lobe are attached to the main lobe, could cause some increase in the reflection level and truncations due to their closed angle. This characteristic should be considered in the posterior analysis when the IR filters and lens shall be included in simulation.

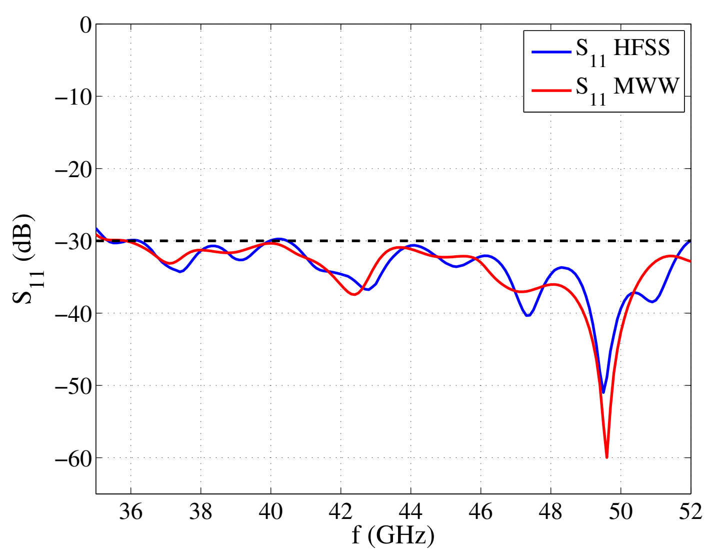

Figure 3.5: Comparison between HFSS and MWW reflection losses.

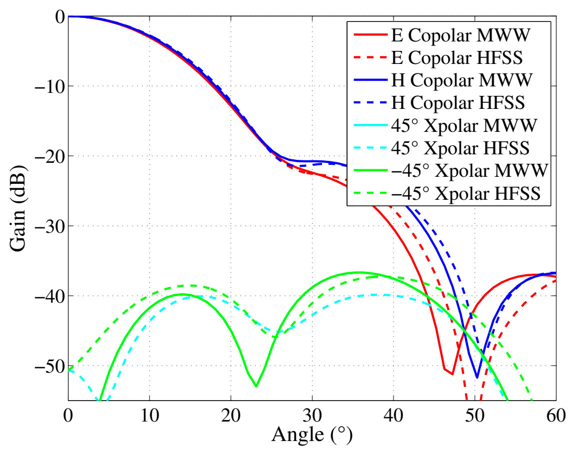

(a) Far-field Pattern at 35 GHz.

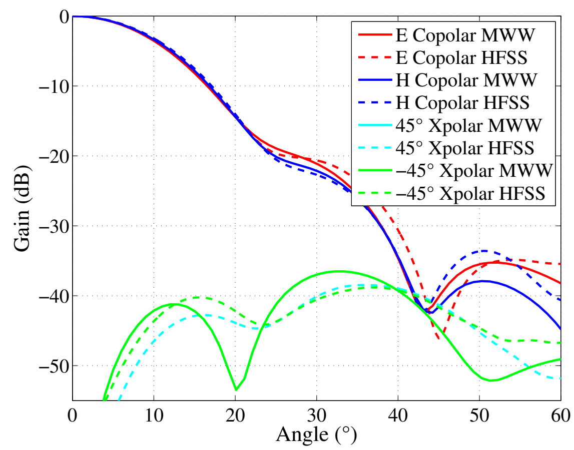

(b) Far-field Pattern at 38 GHz.

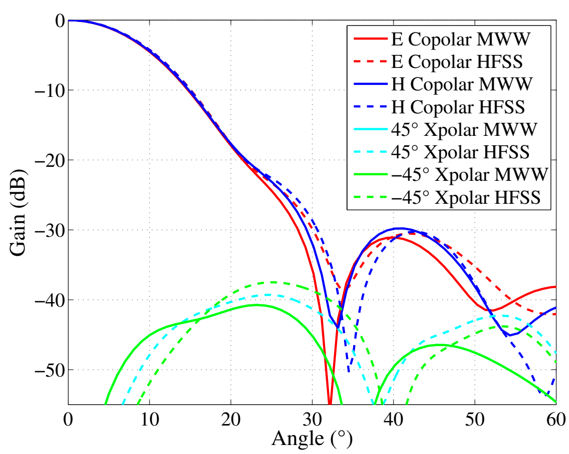

(c) Far-field Pattern at 42.5 GHz.

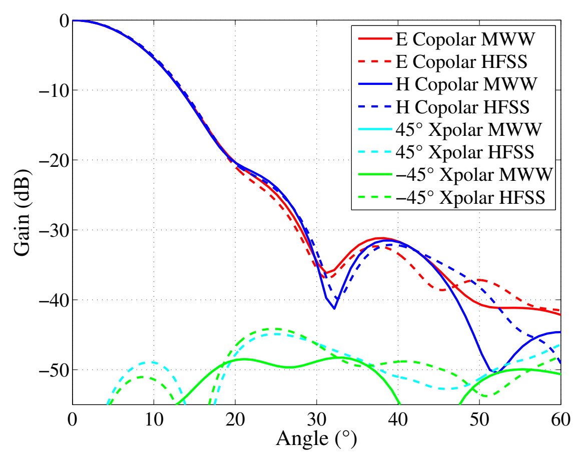

(d) Far-field Pattern at 47 GHz.

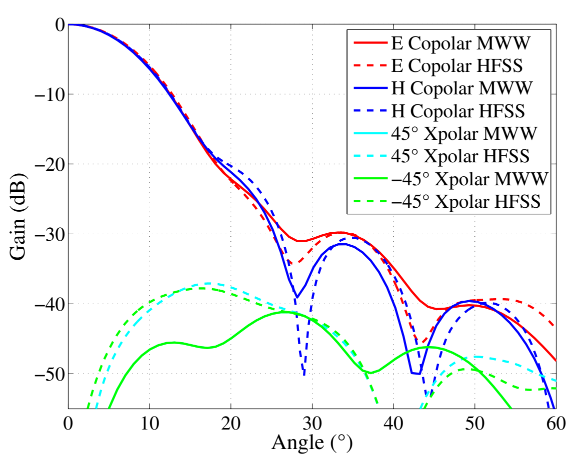

(e) Far-field Pattern at 50 GHz.

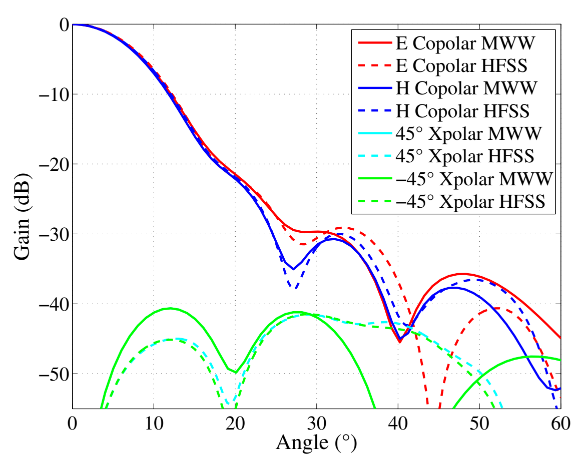

(f) Far-field Pattern at 52 GHz.

Figure 3.6: Comparison between HFSS and MWW simulated far-field patterns for 6 frequency point were calculated from 35 to 52 GHz for the first spline corrugated horn design.

Table 3.4: Main resulting parameters between 33–52 GHz of first spline-profile corrugated horn design from MWW simulations.

Freq (GHz)	Shoulder level (dB)	XPolar (dB)	10 dB point (dB)	BW E (mm)	BW H (mm)	PCL E (mm)	PCL H (mm)
35	−21.5	−36.7	17.9	9.52	9.36	6.22	5.52
38	−20.1	−36.5	16.8	9.40	9.27	6.35	7.14
42.5	−22.9	−40.8	14.8	9.46	9.40	7.78	8.70
47	−22.4	−48.3	13.4	9.21	9.25	10.22	9.80
50	−30.3	−41.2	12.5	9.45	9.52	11.10	11.41
52	−22.1	−40.6	12.0	9.43	9.63	12.81	11.38

3.3 Lens design procedure

In order to optimize the illumination of the sub-reflector with a single warm lens, a quasi-optical propagation script was used [39]. The inputs for this script are the beam-waist size and position of the designed horn, while the optimization parameters are the lens position, the focal distance, and the beam radius. The outputs are the distance from the horn aperture to the center of the lens and the focal length. The best solution was found with a lens located about 175 mm from the horn aperture and a focal length of 168 mm. Some quasioptical configuration examples are shown in table 3.5 where edge taper is used to simplified the comparison considering the relation between an ideal Gaussian beam and the edge taper shown in equation 2.16. Therefore, the initial analysis was done considering these parameters. Using a thin-lens approximation and a ideal Gaussian beam of the same parameter that the designed horn, the calculated aperture efficiencies is 81%, where the spillover efficiency is 94.1% and the amplitude is 86.1%.

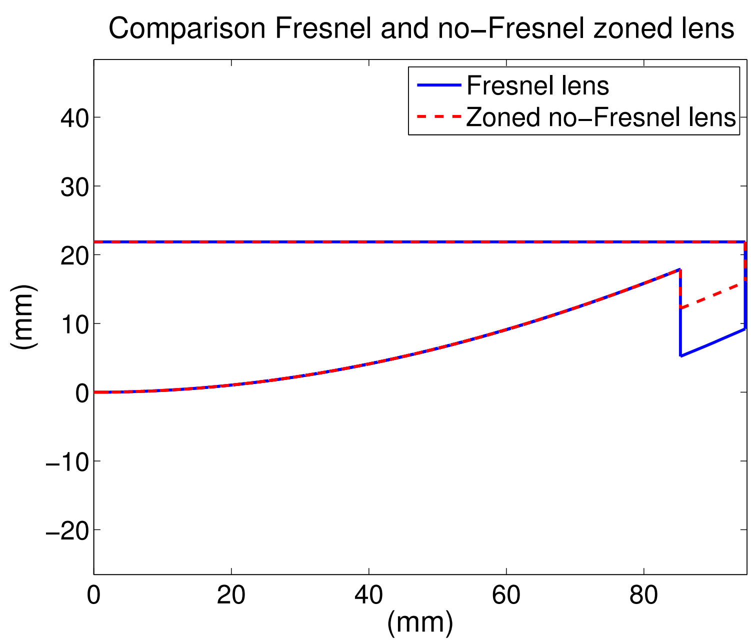

Figure 3.7: Comparison between Fresnel and no-Fresnel zoned lens.

Table 3.5: Quasioptical parameters

Focus (mm)	Distance horn-lens (mm)	Frequency (GHz)	Edge Taper (dB)
168	160	35	-12.0
		42.5	-12.3
		50	-12.2
	175	35	-11.5
		42.5	-11.5
		50	-11.2
	190	35	-8.1
		42.5	-8.7
		50	-8.9
160	175	35	-8.7
		42.5	-9.0
		50	-9.0
170		35	-12.1
		42.5	-12.1
		50	-12.1
180		35	-14.1
		42.5	-14.3
		50	-14.1

The initial design of the optical system, including a standard bi-hyperbolic lens has a noise temperature about 13 K [16]. As it was mentioned above, the lens thickness can be reduced using a zoned lens with only one step. If this design is implemented, the noise of the optics system can be lowered between 2 and 3 K. Unfortunately, the reduction in noise can be accompanied by a reduction in efficiency at some frequencies. Zoning limits the bandwidth operation of the lens introducing frequency dependence. As shown in the equation 2.42 for a Fresnel lens, the theoretical maximum independent frequency bandwidth to a one-zoned lens (K=1) is 25 % and the full Band 1 bandwidth is 44.7 %. Nevertheless, the lens was designed to place the zoned as far as possible from the center of the lens, in order to reduce the interaction between the the zones and the main lobe, allowing a greater bandwidth.

It is important to note that the first and second lens presented in this thesis do not correspond to a Fresnel lens due to a difference in the profile of the zone. The main hyperbola is the same, but the zone was created by moving a distance $\lambda = \frac{c}{f\sqrt{n}}$ the original hyperbola instead of using the Fresnel equation. Some simulations were performed in order to verify that the difference does not significantly alter the performance of the optical system. A minor influence is expected since the position of the zone is far to the center of the lens, where the energy of the pattern is concentrated. A comparison between both profiles is shown in figure 3.7

Some HFSS simulation was conducted using the procedure explain in section 3.3.1 in order to compared the bi-hyperbolic and zoned lens performance. In the first place, it was recognized that the simulated efficiencies were not frequency independent. Moreover, the edge tapers have a significant difference from the Gaussian model and, even more, they are not frequency independent as shown in 3.8(a). Furthermore, a standard no-zoned bi-hyperbolic lens was simulated. The calculated edge

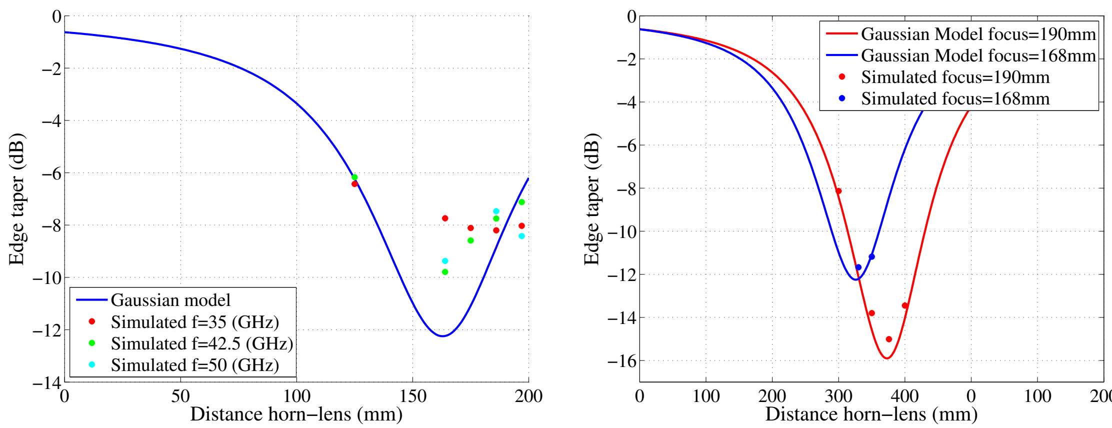

(a) (b)

Figure 3.8: Comparison between theoretical Gaussian model edge taper and HFSS-IE simulated results to zoned and no-zoned lens. (a) One-zoned lens with focus 168 mm and diameter 190 mm and (b) bi-hypertbolic lens focus 168 and 190 mm, diameter 190 mm.

taper matched well with the Gaussian model as shown in 3.8(b). Consequently, the Gaussian beam approximation for zoned lens design is useful only as a starting point of the design where we have to strongly consider the frequency difference in the beam patterns.

Considering the methodology used to create the zone in the lens, the parameters of hyperbola that create the zone depend on the frequency of design. Consequently, other degrees of freedom are the location of the vertex of the hyperbola and the position of the discontinuity. Particularly, the vertex moves away from the center of the lens when the design frequency are higher, increasing its thickness as shown in figure 3.9. The difference in thickness between a design at 35 GHz and 50 GHz is about 1.8 mm, which is equivalent to an addition of 0.6 K in noise temperature considering only the dielectric contribution. Hence, in order to minimize the noise temperature the best option is to design the zoned lens at 35 GHz. Furthermore, the position of the discontinuity was set as far as possible from the center axis of propagation to decrease the interference of the zone with the main lobe. It was defined considering the minimum allowable thickness, which is 8 mm, necessary to support the differential pressure under vacuum condition. [1].

Finally, an anti-reflection coating is required in order to reduce the power loss due to reflections and standing waves. The fabrication material of the lens was studied in Preliminary Design Review (PDR), the analysis can be found in [16]. The chosen material for the fabrication of the lens is High Density Polyethylene (HDPE), hence, a pattern can be directly machined on the surface of the lens. It was explained in section 2.3.1 that the anti-reflection coating can be an extra layer with a refraction index to minimize the lens-vacuum mismatch or can be produced controlling the index of the material by geometrical modifications. The modified index material is less expensive and more robust regarding the vacuum conditions. When manufacturing the lens with a CNC lathe, a groove profile was considered as first option. The design parameters are the pitch ratio and the depth of the corrugations. The former was calculated to a dielectric constant of 2.35 that required a pitch about 1 considering equations 2.46 and 2.47. The latter depends on the dielectrics constant and the frequency of operation, which in this case will correspond to the central frequency of the band

[1]Calculated by Miguel Sánchez, Mechanical Engineer from Instituto de Astrofsica de Andalucía and Universidad de Chile, using [40]

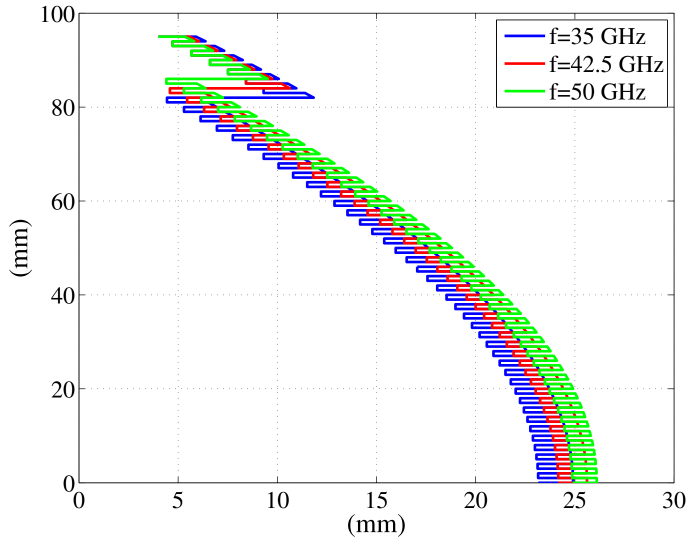

Figure 3.9: Comparison among profiles of zoned lens designed at different frequencies. Notice the different scales of x and y axes.

as shown in the equation 2.45.

3.3.1 Simulation procedure of the entire optical system

The system integrated by a spline corrugated horn, the zoned bi-hyperbolic lens and the structural metallic ring of the lens were simulated as a simplified design. For the lens a dielectric constant $\varepsilon = 2.347$ and loss tangent $\alpha = 2.33 \cdot 10^{-4}$ (corresponding to HDPE material we characterized) were used.

The horn was simulated using HFSS, Finite Element Method solver on frequency domain bases. The output radiated field is calculated over a near field sphere with a radius equal to the horn-lens distance using as excitation a multi-mode circular wave port. The boundary condition were set as Finite Element Boundary Integral (FE-BI), instead of the usual Absorbing Boundary Condition (ABC) or Perfectly Matched Layer (PML), since they present better results in the radiation simulations [41], reducing the dependence of the results on the boundary condition geometry.

As a result of the large separation between the horn antenna and the lens, an HFSS-IE project was inserted. This solver is based on the method of moments, therefore, it does not calculate the solution over the inter-space between the devices reducing the computation points. HFSS-IE simulates the fields of the lens using as excitation the near-field wave generated from the horn which is provide by traditional HFSS. This methodology has the constraint of not consider the electromagnetic effects between the devices that produce the excitation and the excited system as standing waves or couplings effects.

The output near-field pattern is calculated above a sphere centered in the nominal Casegrain focal position with a radius equivalent to the distance from focal point to the subreflector rim for the 12-meter antenna. The output radiation fields are exported and post-processed using MatLab. A script, according to [36], calculates the efficiencies, the cross-polarization, the reflections coefficient,

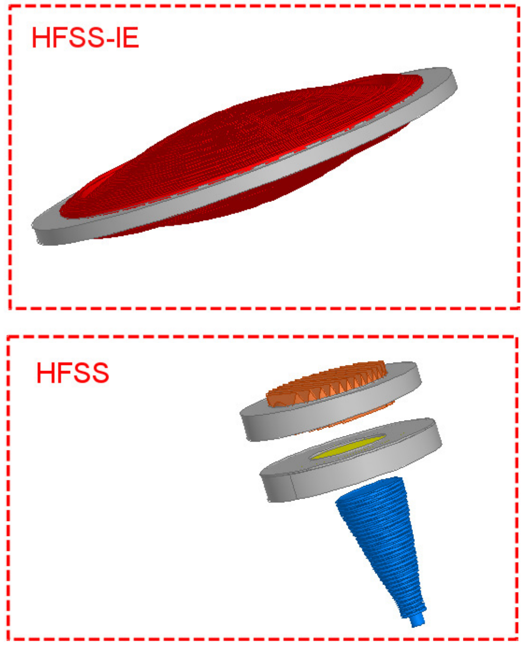

Figure 3.10: Example of a simulated model in HFSS and HFSS-IE.

the maximum sides-lobes level and the cross-section of the radiation beam. The total fields radiated over ϕ from 0° to 360° and θ from 0° to 90° are considered for calculations, it is equivalent to all the energy contained in the upper half radiation sphere, ie all the radiation propagated towards the lens. The angle subtended by the secondary is 3.57°.

Finally, the full optical system (including the horn, the lens, the IR filters and the support metal rings) was simulated. The subsystem formed by the horn and IR filters that was simulated in HFSS was the feed for the lens simulated in HFSS-IE. We assumed a dielectric constant $\varepsilon_r = 1.25$ [42] for the 15-K IR filter made of Goretex and a dielectric constant $\varepsilon_r = 2.08$ [19] for the 110-K IR filter made of Teflon.

Since the simulated devices are electrically large, HFSS-IE simulation was very time-consuming and required high computational resources. In the case of the horn and the lens system, the simulation time was from 8 to 12 hours depending on the frequency and it required about 40 GB of RAM. For the full system between 22 and 40 hours per frequency point were needed and required up to 120 GB of RAM. Hence, only a couple of points per model were simulated, considering only a couple of convergence steps.

Noise temperature

The total noise contribution was estimated considering all the components in the optical path between the horn and the sub-reflector. The components considered were the 15-K and 110-K infrared filters, the aperture of the cryostat, the lens, the aperture of vertex and the sub-reflector. Moreover, we computed the added noise by dielectric losses, truncation and reflections, where some

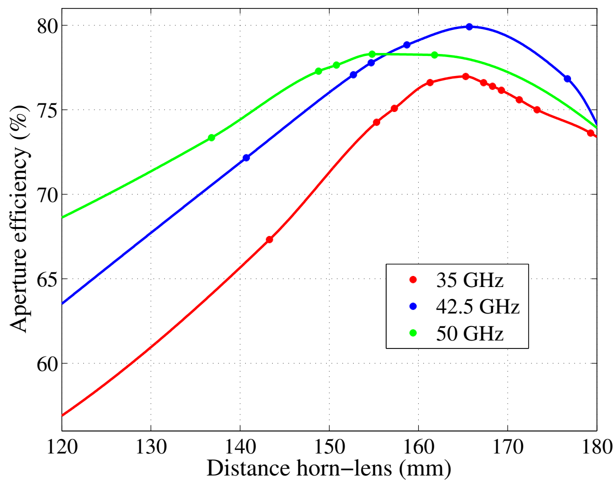

Figure 3.11: Aperture efficiency as function of distance at 35, 42.5 and 50 GHz. Dots are the simulated HFSS-IE aperture efficiencies and the lines are the spline interpolations.

simplifications were deemed in the model. The truncation losses were estimated using a high number of higher order modes through the Mode Matching approximation [2]; excluding the model tilt and the offset in infrared filters. For dielectric losses, the same dielectric constant and loss tangent shown in the simulation description were used, where the average of the thickness was used. In addition, reflection losses in lens and infrared filters was calculated assuming perfect anti-reflection treatment. Finally, the terminated temperature was calculated as the weighted sum of the previous and the next stages in the path. The truncation in the vertex hole was terminated at 300 K while the sub-reflector spillover was terminated at 3 K.

3.3.2 First lens prototype

Having decided to use a zoned lens, the main design parameters are the focus and lens position. Hence, a sensibility analysis about these parameters was performed using the HFSS- IE software. For this study, the procedure consisted on analyzing the aperture efficiency at different positions of the zoned lens for three frequency points. More simulations at the low frequency end were performed since it is part of the band that is the most affected by the zoned region. The results are shown in figure 3.11. Choosing the best lens position is not a obvious decision because each curve has a maximum in a different lens-horn distance. The best distance from the center of the lens to the aperture of the horn was estimated at 162.2 mm. This position has a good balance in aperture efficiency for the three frequency points, providing efficiencies near to the maximum to 35 and 50 GHz. For this distance of the horn, the main parameters are summarized in table 3.6.

The lens, including its metal ring support structure and horn, was simulated in order to calculate the aperture efficiencies. The radiation patterns at 35, 42.5 and 50 GHz are shown in figure 3.12 and the efficiencies in table 3.7. In the radiation patterns two important features can be noticed. Firstly, the 35 GHz pattern has some widening respect to a gaussian profile due to the truncation effects producing a decrease in the spillover efficiency. In addition to the impact on the aperture efficiency, low values in spillover efficiency could be increase the spillover noise if the diffraction

[2]Provided by Masahiro Sugimoto.

Table 3.6: Main design parameters to first lens design.

Principal design parameter	Value
Focus	168 mm
HDPE design dielectric constant	2.232
Distance aperture horn-center lens	162.2 mm
Radius lens	95 mm
Lens thickness	47.58 mm
Lens thickness + corrugations	50.44 mm
Frequency for zoned design	35 GHz
Frequency for corrugations design	42.5 GHz

in the secondary finishes at the ground [43]. Secondly, the cross-polarization level increases about 10 dB, just due to the lens effect. Hence, we must be careful about the contribution of the filters not exceeding the –23 dB to achieve the technical specifications.

The noise temperature of the optical system was estimated between 10 to 11.6 K, where the lens generates the largest contribution. The detail of the contribution of every element in the optical path is presented in figure 3.13.

Table 3.7: Simulated aperture efficiency including horn v1, one-zoned lens f=168 mm, d=162.2 mm and metal lens ring.

Frequency (GHz)	Spillover efficiency (%)	Polarization efficiency (%)	Amplitude efficiency (%)	Phase efficiency (%)	Aperture efficiency (%)
35	79.01	99.99	95.81	99.94	**75.65**
42.5	84.00	99.91	93.88	99.49	**78.39**
50	84.20	99.60	94.77	99.62	**79.18**

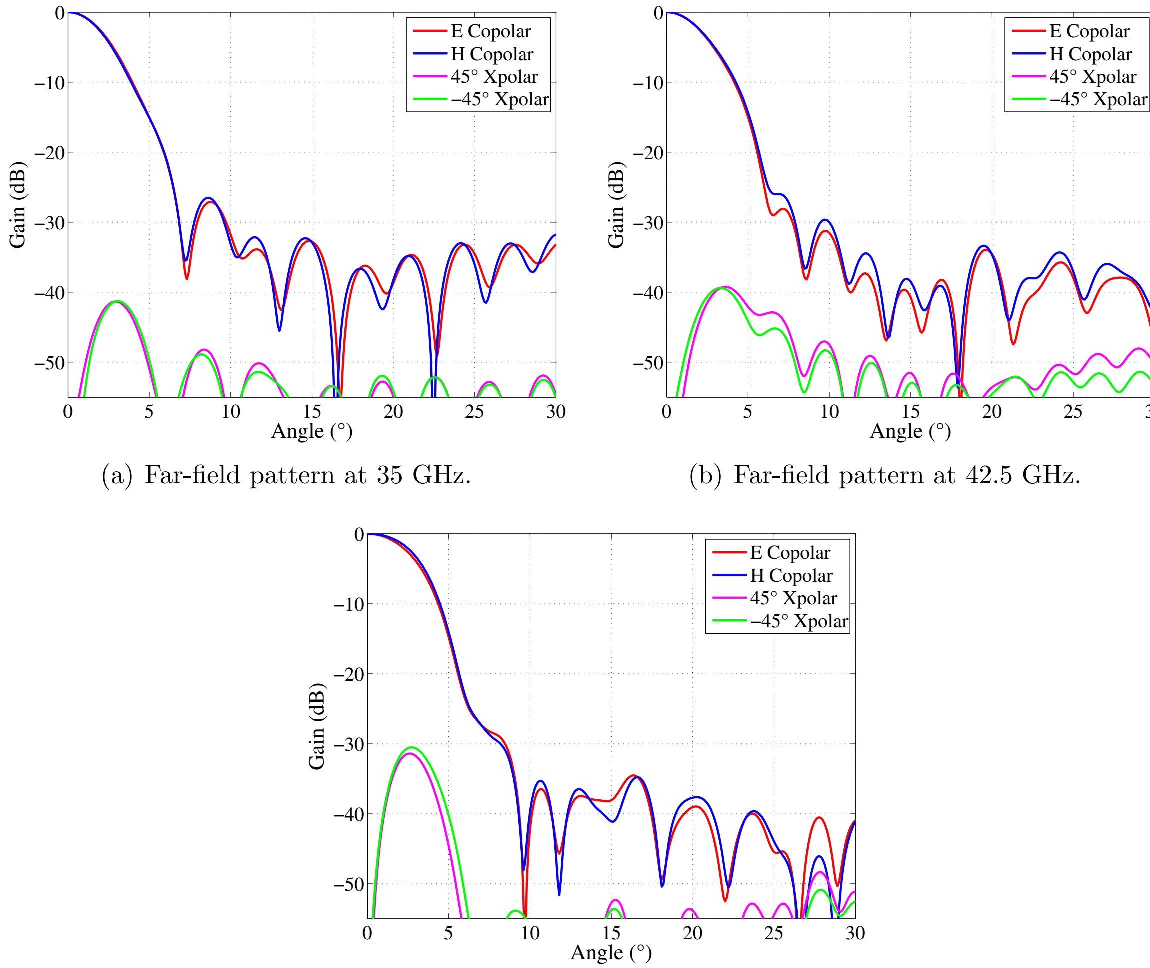

(a) Far-field pattern at 35 GHz.

(b) Far-field pattern at 42.5 GHz.

(c) Far-field pattern at 50 GHz.

Figure 3.12: Simulated far-field radiation pattern at 35, 42.5 and 50 GHz of lens v1 and horn v1.

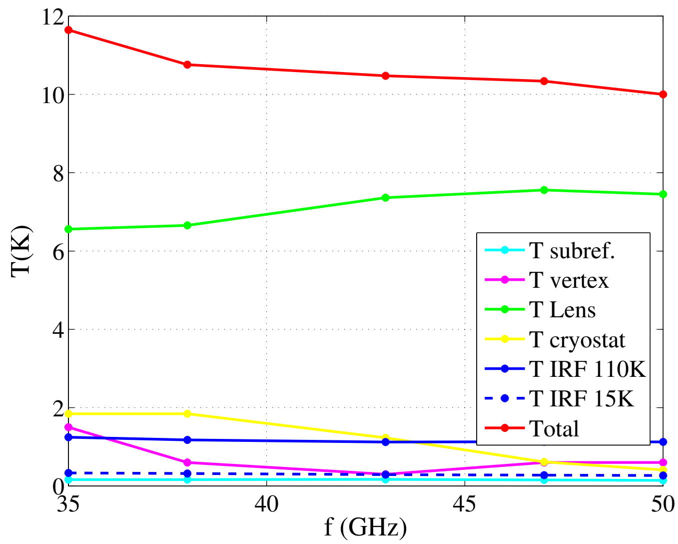

Figure 3.13: Simulated noise temperature of the full system, including horn v1 and lens v1. Dots are the simulated noise temperature and the lines these interpolate values.

3.3.3 Second lens prototype

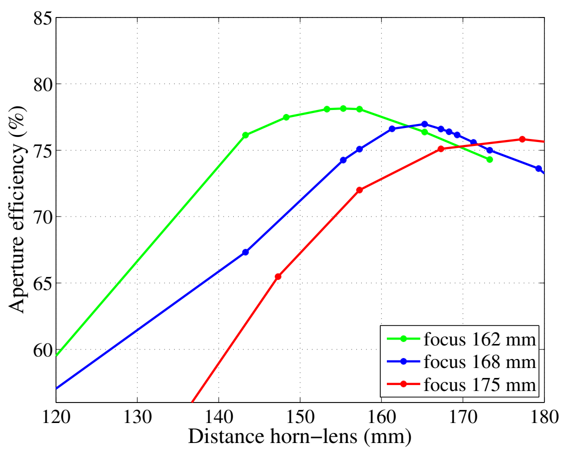

(a) Aperture efficiency at 35 GHz.

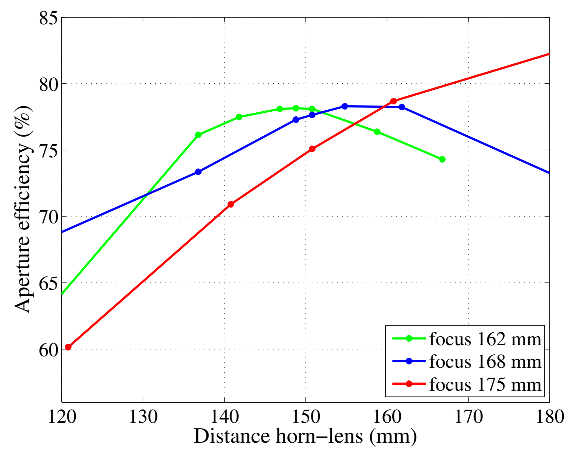

(b) Aperture efficiency at 50 GHz.

Figure 3.14: Simulated aperture efficiencies at 35, 42.5 and 50 GHz of the system composed by lens v2 and horn v1 for different focus and distances. Dots are the simulated HFSS-IE aperture efficiencies and the lines are interpolations.

Table 3.8: Main design parameters to second lens design.

Principal design parameter	Value
Focus	165 mm
HDPE design dielectric constant	2.347
Distance aperture horn-center lens	164.2 mm
Radius lens	95 mm
Lens thickness	44 mm
Lens thickness + corrugations	46.86 mm
Frequency for zoned design	35 GHz
Frequency for corrugations design	42.5 GHz

A second lens was designed since the first prototype did not achieve the efficiency requirements. Compared to the first prototype, the second one includes a retuned focal length and horn-lens distance. Moreover, the features of the zone step position and angle were improved in order to reduce shadowing due to the zone step. The principal design parameters are summarized in table 3.8.

Several HFSS simulations were conducted to find a better aperture efficiency. These aperture efficiencies versus focus and distance are shown in figure 3.14. It can be noticed at 35 GHz that the maximum in the curves that represent different focus decrease when the distance horn-lens is longer, contrary to the simulation at 50 GHz. Hence, the best balance was found at a focus of 165 mm and a distance of 164.2 mm. The simulation included the effect of the corrugation in the lens. The estimated efficiencies are shown in table 3.9.

The subsystem that include lens, its metal ring support structure and horn was simulated to calculate the aperture efficiencies. The radiation pattern at 35, 42.5 and 50 GHz are shown in the figure 3.15 and the efficiencies are shown in table 3.9. The patterns are less affected by truncation effects and has better spillover efficiencies that the first one. Moreover, they present low shoulders or side lobes and a good symmetry with differences lower than 0.3° to –20 dB. The cross-polarization of the sub-system is high at 50 GHz considering that the filters effect were not considered in the simulation. The noise temperature was estimated between 9.9 to 11.6 K, where the lens generates the largest contribution. The detail of the contribution of every element in the optical path is shown in figure 3.16.

Table 3.9: Simulated aperture efficiency including horn v1, one-zone lens f=165 mm d=164.2 mm and lens metal ring.

Frequency (GHz)	Spillover efficiency (%)	Polarization efficiency (%)	Amplitude efficiency (%)	Phase efficiency (%)	Aperture efficiency (%)
35	82.89	99.99	94.61	99.71	**78.19**
42.5	89.18	99.99	90.03	99.94	**80.77**
50	89.32	99.94	89.86	99.28	**79.64**

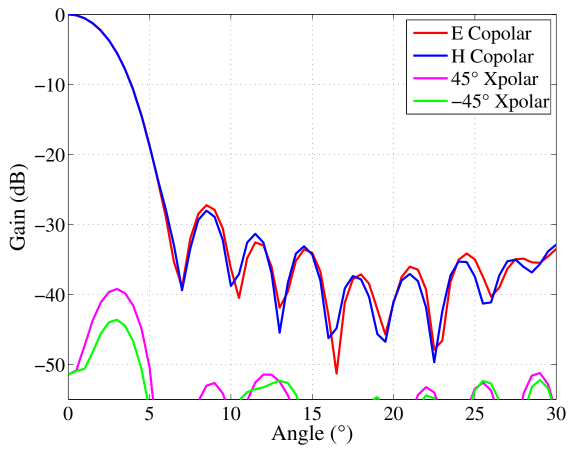

(a) Far-field pattern at 35 GHz.

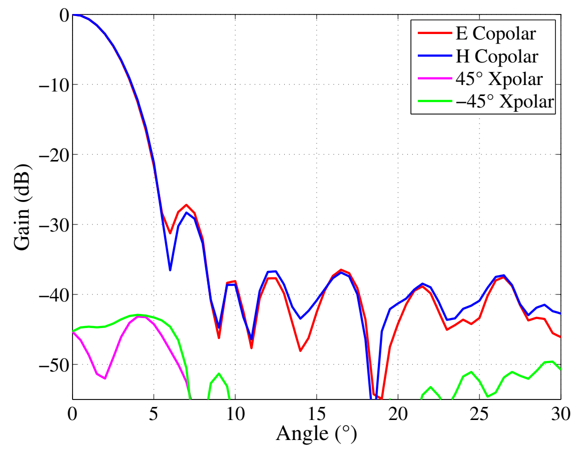

(b) Far-field pattern at 42.5 GHz.

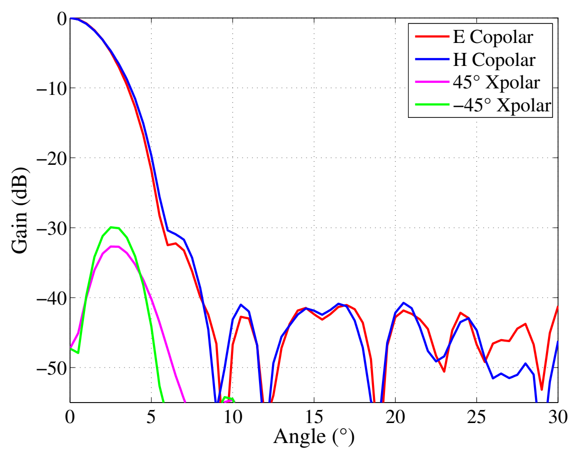

(c) Far-field pattern at 50 GHz.

Figure 3.15: Simulated far-field radiation pattern at 35, 42.5 and 50 GHz to lens v2 and horn v1.

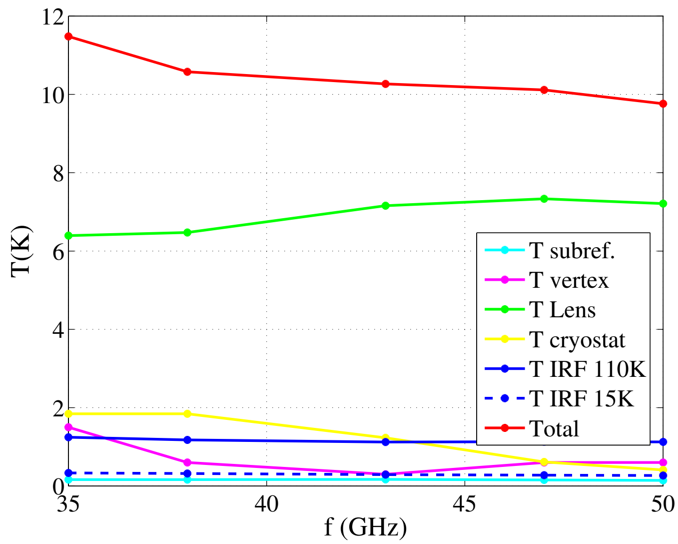

Figure 3.16: Simulated noise temperature of the full system, including horn v1 and lens v2. Dots are the simulated noise temperature and the lines these interpolate values.

3.4 Second horn design

A second iteration was conducted in the design process aiming to achieve better aperture efficiencies. The main difficulty with the first system was that it reached low spillover efficiencies. For this reason, the second prototype changed the optimization goals to produce a constant aperture illumination with very low side lobes along with a performance more similar to the Gaussian mode than the hybrid mode of the usual corrugated horns. Concretely, strict restrictions were included to the desired angle at 10, 20 and 25 dB. Moreover, the goals related to the symmetry, reflected power and PCL are more ambitious. In addition, the widths of the first 6 corrugations were included as optimization parameters. It have been incorporated to improve the mode converter that takes place in the corrugations next to the input waveguide. The converter mode is highly relevant since it achieves the matching of impedance to transform the TE_{11} incoming from the waveguide and the HE_{11} mode propagate into the horn [44]. The main goals are summarized in table 3.10

The resulting profile has deeper corrugations of variable width in the mode converter than the first designed horn, providing a better match between the input and propagated modes into the

Table 3.10: Main optimization goals between 33–52 GHz to second spline profile corrugated horn design.

Freq(GHz)	33	35	38	41	42.5	44	47	50	52
10 dB Point (°)	19.1	18.0	16.6	15.4	14.9	14.3	13.4	12.6	12.1
20 dB Point (°)	-	25.5	23.5	21.8	21.0	20.3	19.0	17.9	-
25 dB Point (°)	-	28.5	26.3	24.3	23.5	22.7	21.3	20.0	-
Crosspolarization (dB)	<–30				<–37				<–30
Reflected power (dB)	<–25				<–32				<–25
10 dB point difference E/H(°)	< 1				<0.1				<1
PCL difference (mm)	<1				<0.3				<1

Table 3.11: Main mechanical parameters of horn v2 design.

Horn design parameter	Value
Input circular WG radius (R_0)	3.35 mm
Horn Aperture radius ($r31$)	31.26 mm
Horn total length	70 mm
Number of corrugations	31
Width of corrugation (Ci)	0.80–0.93 mm
Width of gap (G)	1.06–1.35 mm
Depth of gap ($R\mathrm{i} - r\mathrm{i}$)	1.46–3.17 mm

antenna. The aperture radius is slightly smaller than the first horn, nevertheless, the corrugation in the transition zone between the antenna and the free space has a higher angle which allows lower side-lobes as seen in similar devices presented in [35].

The design was validated using HFSS. Simulations with a resolution of 50 MHz were performed to study reflection losses. Figure 3.18 shows a comparison between the result obtained with HFSS and MWW. It is observed that the reflected losses have a low value, below –30 dB according to HFSS and –28 dB according to MWW in the frequency range from 35–52 GHz. The structure of the curve is very similar with an offset of 0.4 GHz in the peak of the curve.

A comparison between the far-field radiation patterns at different frequencies calculated with HFSS and MWW is presented in figure 3.19. They are identical down to –20 dB with minor difference in the side lobes. They are better than -23 dB. The cross-polarization curves have similar shape, but exhibit substantial differences. Nevertheless, their maximum are similar to a difference lower than 5 dB and also all of them are better than –35 dB. The main parameters of the beam patterns, calculated with MWW are summarized in table 3.12.

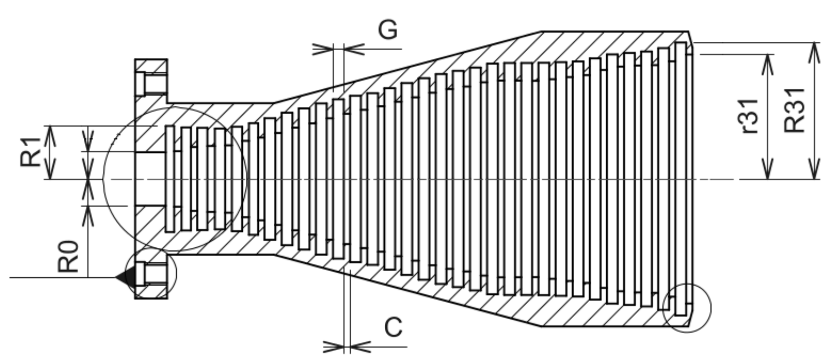

Figure 3.17: First spline profile corrugated horn design.

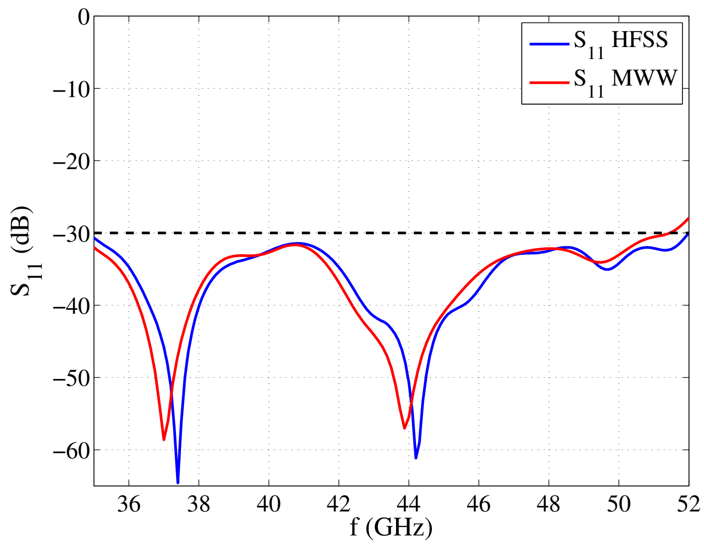

Figure 3.18: Comparison between HFSS and MWW reflection losses, horn v2.

It is clear that the changes in the horn profile have a positive influence in the radiation patterns, providing a better start point to achieve higher aperture efficiencies. In comparison with the first horn designed, the copolar patterns present a shape more similar to a gaussian beam. The side lobes are totally detached of the main lobe and are lower values specially at the initial frequencies of the band where the truncation phenomena has more concernment. The crosspolar and beamwaist values are very similar to the obtained in the first horn; they presented a good behavior. Finally, the PCL values are nearer to the aperture of the horn, presenting a more constant increase respect to the frequency and have a better symmetry. It was expected due to the stricter goals.

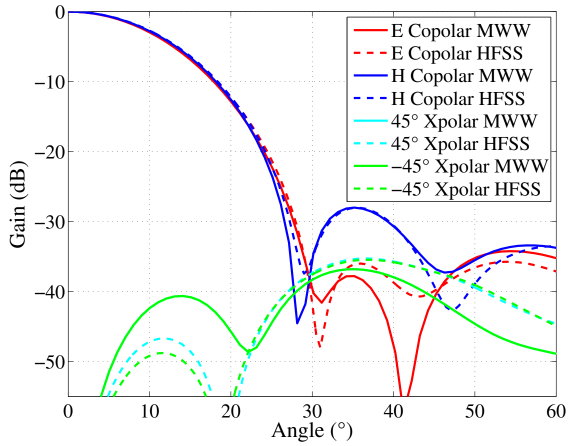

(a) Far-field Pattern at 35 GHz.

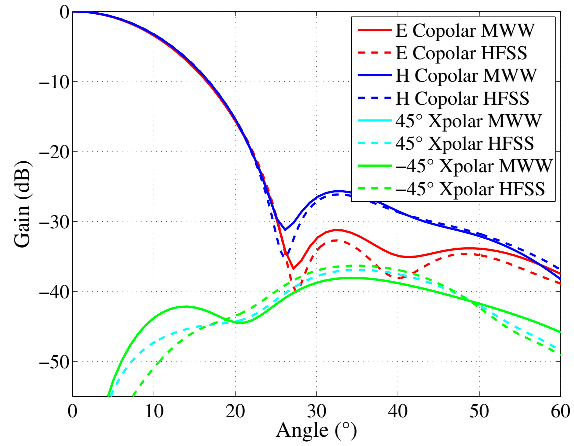

(b) Far-field Pattern at 38 GHz.

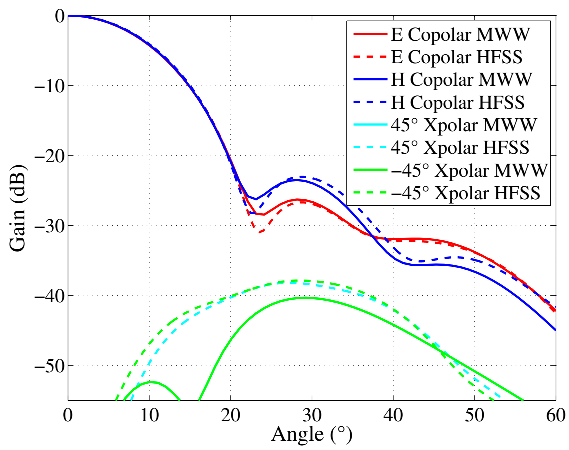

(c) Far-field Pattern at 42.5 GHz.

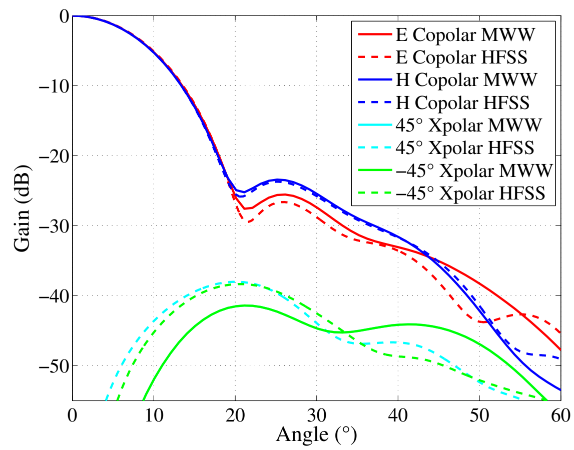

(d) Far-field Pattern at 47 GHz.

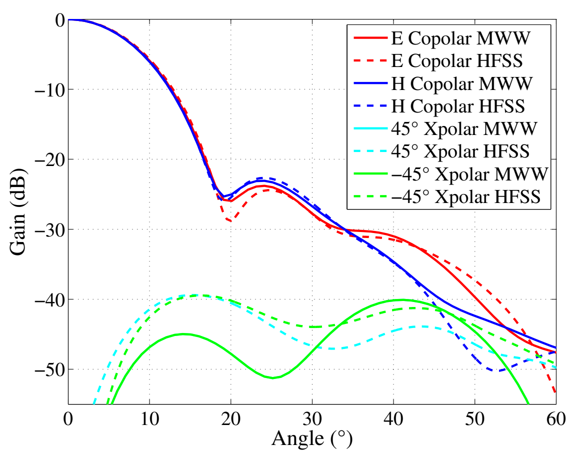

(e) Far-field Pattern at 50 GHz.

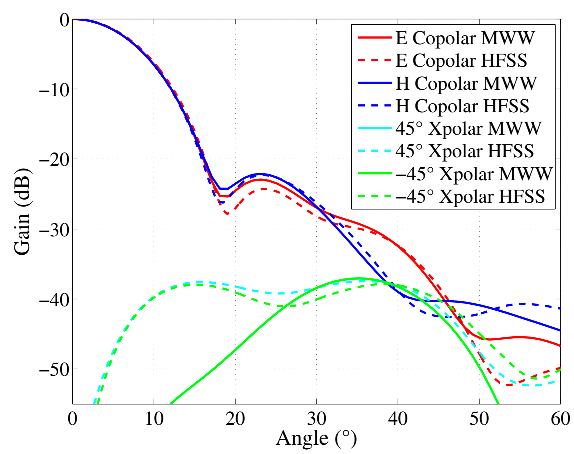

(f) Far-field Pattern at 52 GHz.

Figure 3.19: Comparison between HFSS and MWW simulated far-field patterns for 6 frequency point were calculated from 35 to 52 GHz for the second spline corrugated horn design.

Table 3.12: Main resulting parameters between 33–52 GHz to second spline profile corrugated horn design, MWW simulations.

Freq (GHz)	Sidelobes level (dB)	XPolar (dB)	10 dB point (dB)	BW E (mm)	BW H (mm)	PCL E (mm)	PCL H (mm)
35	−28.0	−36.8	18.03	9.47	9.33	1.66	1.12
38	−25.7	−38.1	16.62	9.45	9.33	3.68	4.04
42.5	−23.5	−40.3	14.88	9.39	9.37	5.24	5.17
47	−23.4	−41.4	13.48	9.33	9.40	7.09	7.20
50	−23.1	−40.1	12.64	9.33	9.45	6.79	6.89
52	−22.1	−37.1	12.14	9.41	9.39	7.35	7.55

3.5 Third lens design

In order to improve the current aperture efficiency, new parameters to the one-zoned lens were proposed by Álvaro González from NAOJ. The best distance and focus length of the lens was sought conducting a sweep of frequency and computed all the efficiencies. The simulation procedure was done through WaspNET, a commercial software that combines different simulation methodologies. Particularly, the lens and horn subsystem was simulated using a combination of mode matching technique and method of moments, exploiting the rotational symmetry tools to generate very fast simulation, taking just a couple of minutes per frequency point. Moreover, Wasp-net is enabled to consider standing wave and impedance coupling between all the elements including the simulation. The best result was achieved at a focus length of 181 mm and a distance between the center of the lens to the aperture of the horn of about 175 mm. The aperture efficiencies for 6 frequencies are shown in table 3.13, where the integration solid angle was consider from θ from -30° to 30°.

Table 3.13: Aperture efficiency including Horn v2, one-zoned lens f=181 mm, d=175 mm and metal lens ring, WaspNET simulation.

Frequency (GHz)	Spillover efficiency (%)	Polarization efficiency (%)	Amplitude efficiency (%)	Phase efficiency (%)	Aperture efficiency (%)
35	90.56	99.97	90.84	99.95	**82.20**
38	91.38	99.93	89.79	99.89	**81.91**
42	91.85	99.92	90.33	99.87	**82.79**
47	92.60	99.78	90.40	99.66	**83.24**
50	91.75	99.87	90.38	99.55	**82.45**
52	90.90	99.83	90.93	99.02	**81.71**

3.5.1 HFSS Verificaton

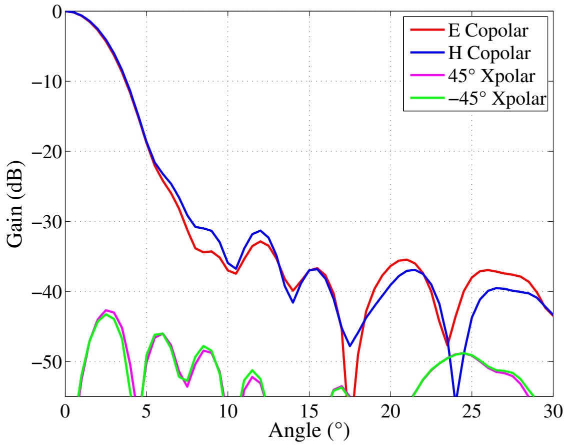

(a) Far-field pattern at 35 GHz.

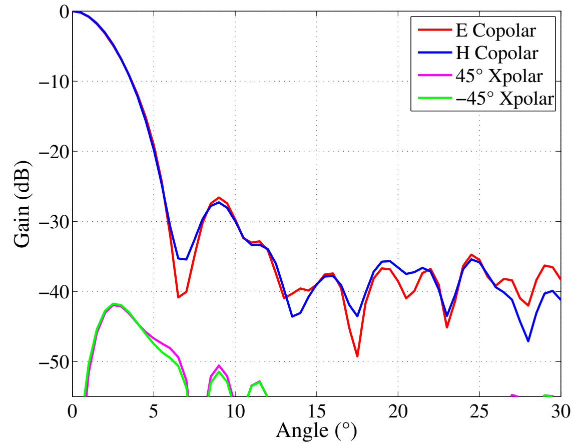

(b) Far-field pattern at 42.5 GHz.

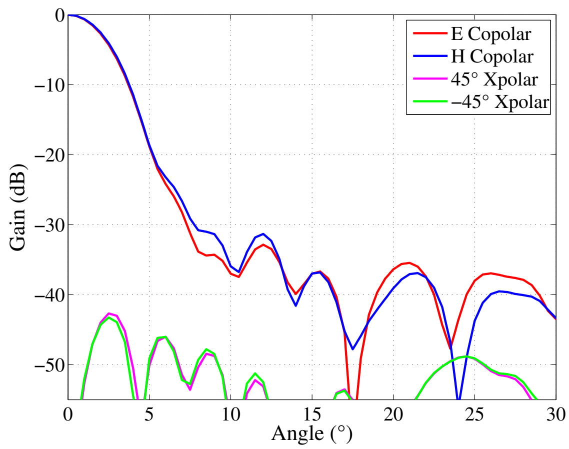

(c) Far-field pattern at 50 GHz.

Figure 3.20: Far-field radiation pattern at 35, 42.5 and 50 GHz with lens v3 and horn v2, HFSS simulation.

In order to verify in the same way as the rest of the models presented in this thesis, a full electromagnetic analysis was performed using HFSS. Figure 3.20 shows the far-field beam pattern at 35, 42.5 and 50 GHz. The computed aperture efficiencies are shown in table 3.14. All the simulated apertures efficiencies are better than 80%, which is the especification from ALMA. Nevertheless, differences of 2.5% in the calculated spillover and amplitude efficiencies can be found. They produce differences higher than 1% in the computed aperture efficiencies. The differences can be explained by the resolution methodologies mentioned in section 3.3.1. The HFSS simulations do not consider the standing wave and impedance coupling between horn and lens, since they are simulated in separate modules. Moreover, HFSS consider the full 3D model, requiring long time and computational resources, and also allowing only a couple of convergence steps per model.

Table 3.14: Aperture efficiency including horn v2, one-zone lens f=181 mm, d=175 mm and metal lens ring, HFSS simulation.

Frequency (GHz)	Spillover efficiency (%)	Polarization efficiency (%)	Amplitude efficiency (%)	Phase efficiency (%)	Aperture efficiency (%)
35	87.50	99.99	92.53	99.75	**80.76**
42.5	88.93	99.99	91.27	99.45	**80.77**
50	86.73	99.98	93.91	98.68	**80.36**

3.5.2 Effects of infrared filters

Although the system was designed considering a minimum effect of the mechanical rings structures, it is necessary to evaluate their impact on the performance produced by truncation and the infrared filters dielectric. An initial quasi-optical analysis was conducted in order to have a good estimation of the level of the truncation. We considered a fundamental Gaussian beam using the beam-waist resulting in the HFSS simulation shown in table 3.12 and the mechanical parameter of the lens v3. Moreover, we assumed that the center of the infrared filters is in the axis of propagation. The estimated values are shown in table 3.15. The most critical truncation was found in the metallic ring of the lens at 35 GHz. Nevertheless, the ring that presents higher truncation at all frequencies is the ring of the 15-K infrared filter. These values are acceptable, if we notice that a truncation in –34.7 dB in a ideal gaussian beam represents a free pass of 99.97% of the energy [19]. Nevertheless, in real patterns that include sidelobes a deformation of the beam pattern will be present.

FEM simulations was conducted with FE-BI boundary conditions in HFSS, in order to study the effect of the filters in a more realistic way. The first step consisted on analyzing the effect of the metallic ring of the 15-K infrared filter. A comparison between the radiation pattern of the horn and horn plus rings of the 15-K infrared filter is shown in figure 3.21. The truncation effects are small, having an incidence of a few dB in the level of the shoulder and side lobes and a slight widening at 35 GHz. All these effects are lower than –20 dB. Moreover a maximum increase of 5 dB was found in the cross-polarization.

In a second step we included in the simulation the metallic rings of the 110-K filter. A comparison between the horn only and horn plus all the rings is shown in figure 3.22. This configuration presents more substantial changes in the shape of the beam. The main-lobe shows a ripple in the

Table 3.15: Truncation level due to mechanical support structures.

Frequency (GHz)	15 K filter (dB)	110 K filter (dB)	Cryostat (dB)	Lens (dB)
35	–34.7	–34.2	–36.5	–33.2
38	–35.4	–37.7	–42.0	–38.8
42.5	–36.2	–42.8	–50.7	–47.9
47	–36.9	–47.4	–59.6	–57.8
50	–37.0	–50.2	–65.9	–65.1
52	–37.1	–52.0	–70.1	–70.2

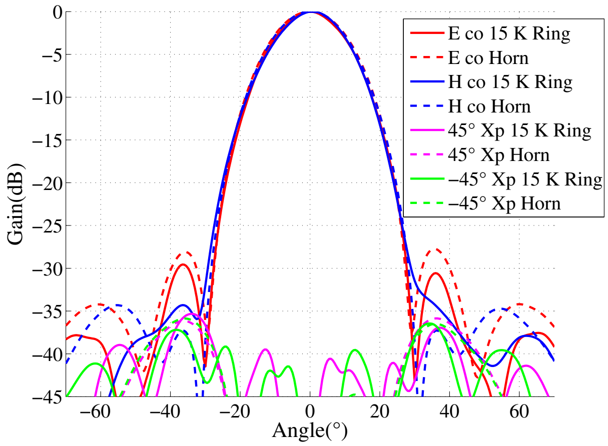

(a) Far-field pattern at 35 GHz.

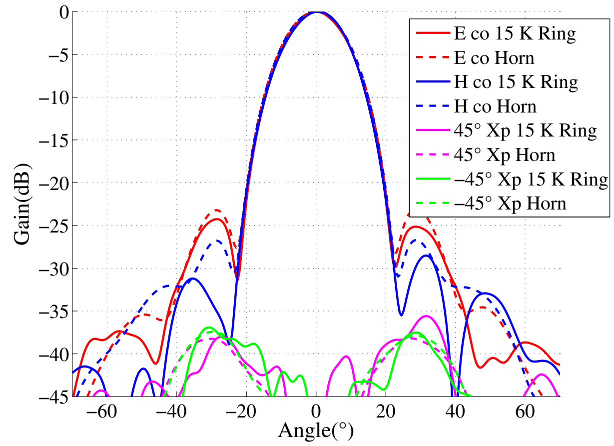

(b) Far-field pattern at 42.5 GHz.

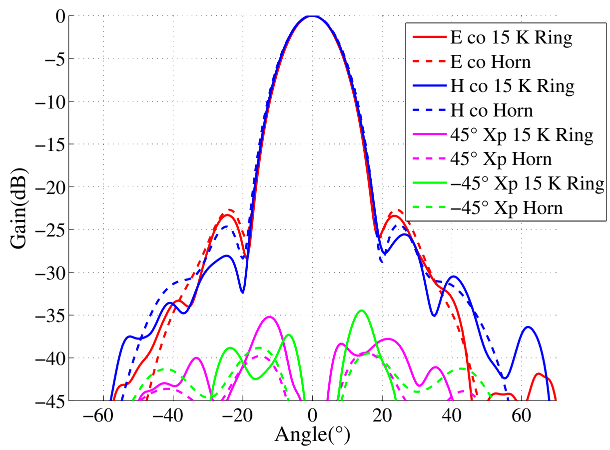

(c) Far-field pattern at 50 GHz.

Figure 3.21: Simulated far-field radiation pattern at 35, 42.5 and 50 GHz for the horn v2 (dotted line) and of the horn plus rings of 15 K filter (solid line).

top, especially in the beam pattern at 50 GHz. The deformation in the beam appears to involve reflections in the 110-K metal ring, considering the position of the deformation, the tilt angle of the ring, the characteristics of the estimated widening and side-lobe level. Besides, the crosspolarization level increase more than 10 dB, but is lower than –30 dB.

Later, the dielectrics of the filters were included in the simulation model. A comparison between the horn and the horn both infrared filters are shown in figure 3.23. The shape in the main lobe is similar to the case with only the rings of the infrared filters. The main difference is the level of the crosspolarization, wich anyway, is better than –29.5 dB.

Finally, the full optical system was compared with the system composed by only the horn and lens. As it was expected, the beam patterns of the full system are wider and also present higher side lobes due to effects of the infrared filter. The cross-polarization level increases, but stays below –30 dB. The reflection effects are present in the slight asymmetries that presents the beam. Moreover, we compared the apertures efficiencies for both scenarios, table 3.16 shows the results. The differences are lower than 0.01%

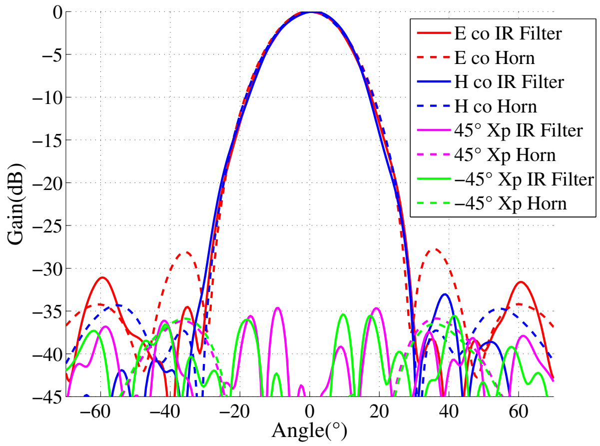

(a) Far-field pattern at 35 GHz.

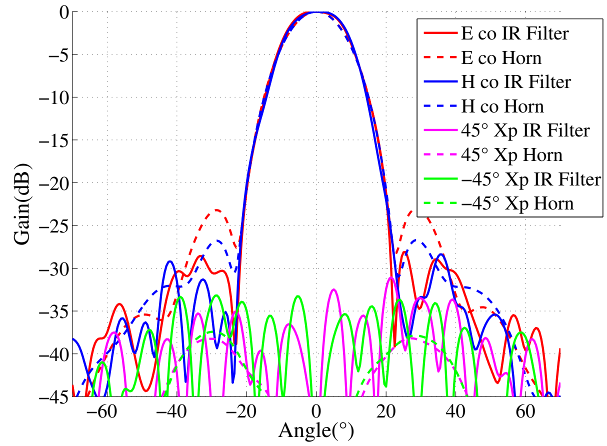

(b) Far-field pattern at 42.5 GHz.

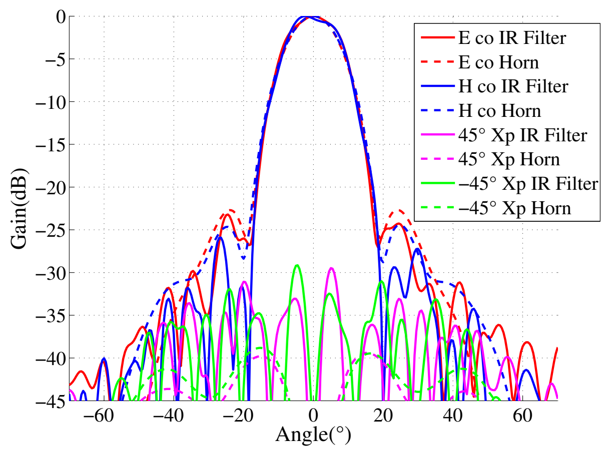

(c) Far-field pattern at 50 GHz.

Figure 3.22: Simulated far-field radiation pattern at 35, 42.5 and 50 GHz for the horn v2 (dotted line) and the horn plus infrared filter rings (solid line).

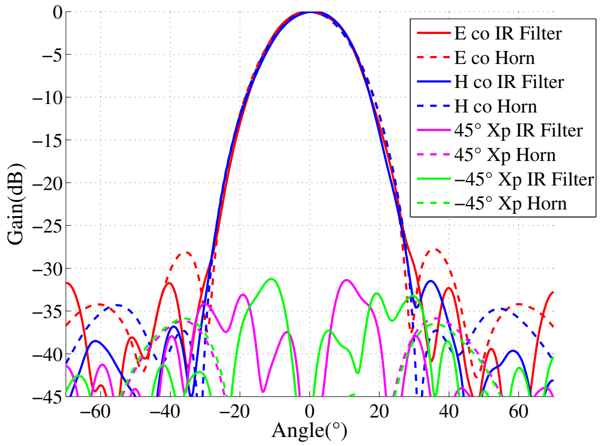

(a) Far-field pattern at 35 GHz.

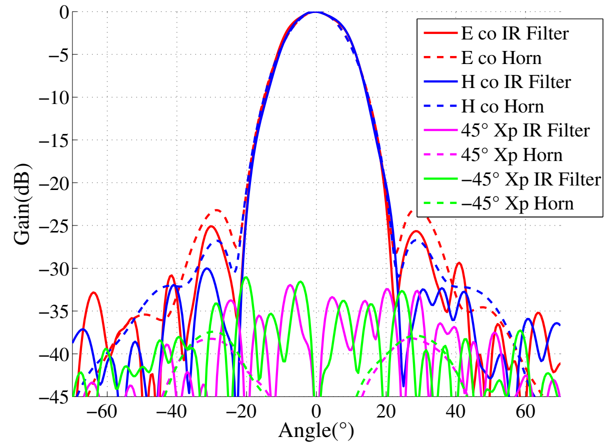

(b) Far-field pattern at 42.5 GHz.

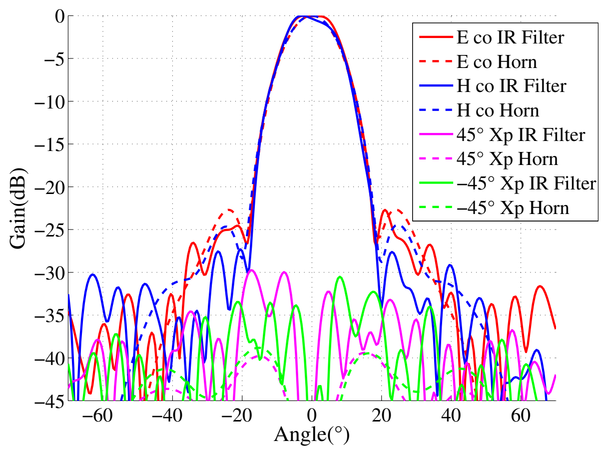

(c) Far-field pattern at 50 GHz.

Figure 3.23: Simulated far-field radiation pattern at 35, 42.5 and 50 GHz for the horn v2 (dotted line) and both infrared filters and rings (solid line).

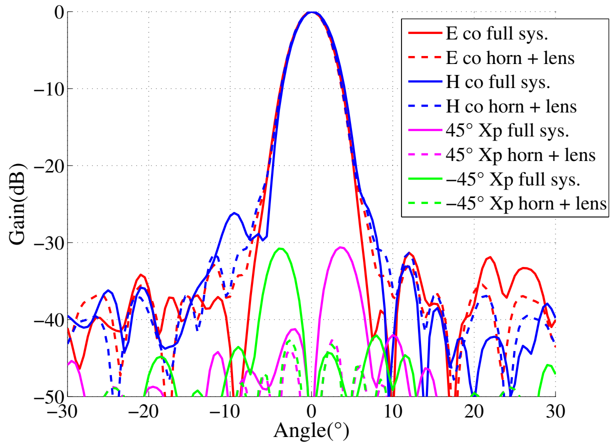

(a) Far-field pattern at 35 GHz.

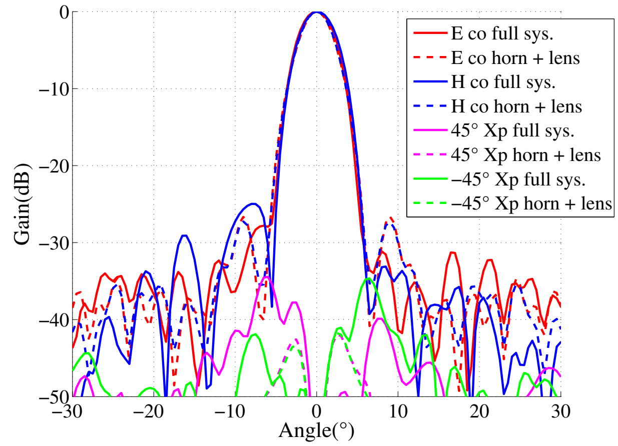

(b) Far-field pattern at 42.5 GHz.

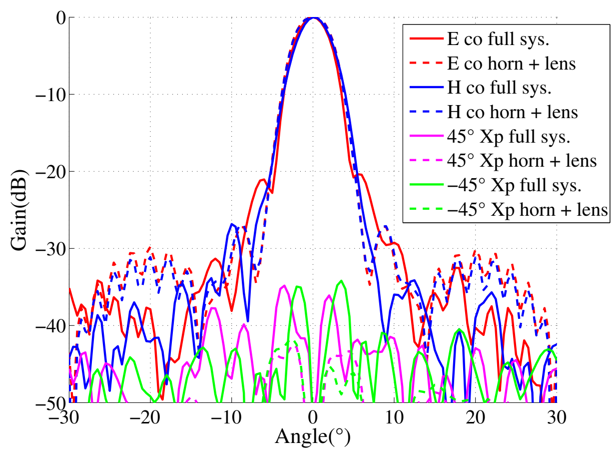

(c) Far-field pattern at 50 GHz.

Figure 3.24: Simulated far-field radiation pattern at 35, 42.5 and 50 GHz for horn plus lens (dotted line) and full system (solid line).

3.5.3 Noise temperature

The noise temperature of the optical system was estimated between 9.5 and 11.3 K, where the lens generates the largest contribution. The detail of the contribution of every element in the optical path is presented in figure 3.25.

Table 3.16: Simulated aperture efficiency including horn v2, one-zone lens f=181 mm, d=175 mm and metal lens ring.

Frequency (GHz)	Spillover efficiency (%)	Polarization efficiency (%)	Amplitude efficiency (%)	Phase efficiency (%)	Aperture efficiency (%)
35	86.79	99.95	93.15	99.80	**80.64**
42.5	89.98	99.99	92.27	98.62	**81.87**
50	87.76	99.97	92.07	99.26	**80.26**

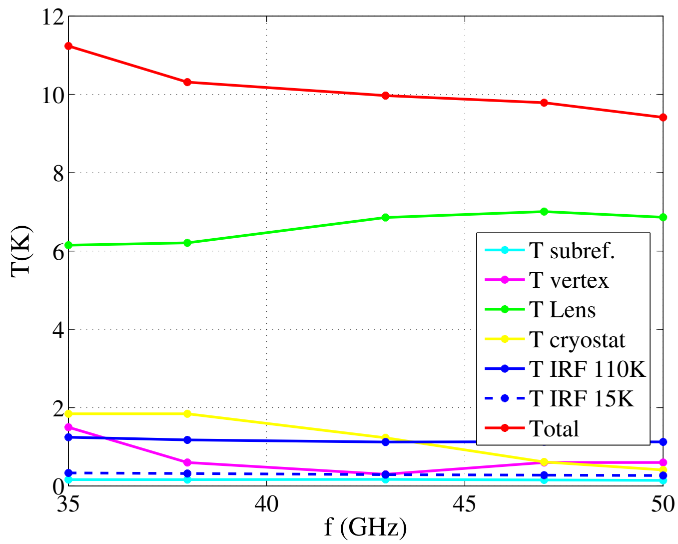

Figure 3.25: Simulated noise temperature of the full system, including horn v2 and lens v3. Dots are the simulated noise temperature and the lines the interpolated values.

3.6 Compatibility between 7 and 12-meter antennas of the optical system

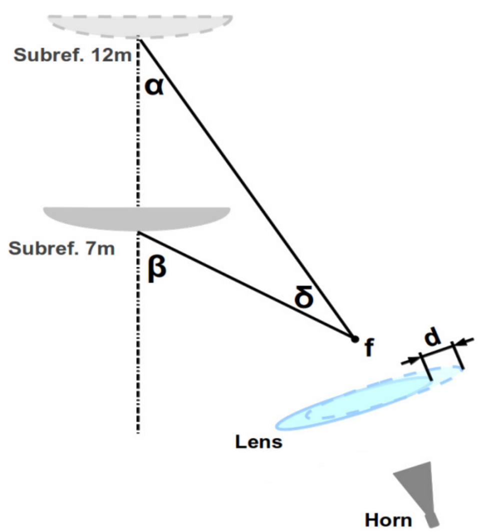

Figure 3.26: Schematic sub-system for antenna 7 and 12-meter. Where $\alpha = 2.48°$, $\beta = 4.28°$, $\delta = 1.8°$ and d=5.61 mm.

Table 3.17: Simulated aperture efficiency including horn v2, one-zone lens f=181 mm, d=175 mm and metal lens ring.

Frequency (GHz)	Spillover efficiency (%)	Polarization efficiency (%)	Amplitude efficiency (%)	Phase efficiency (%)	Aperture efficiency (%)
35	86.94	99.98	92.44	99.72	**80.13**
42.5	90.57	99.91	91.34	98.42	**81.35**
50	88.95	99.96	90.64	99.38	**80.09**

As already mentioned in section 1.2, the system must be compatible with the 7 and 12-meter antennas, which have different angles of projection on the sub-reflector. The beam angle for the 7-meter antenna is 4.28° and 2.48° for the 12-meter antenna. The baseline solution proposed in [45] is a prism placed in the middle of lens and the calibration devices. This prism can be installed when the front end is used in 7-meters antennas, contrary to the 12-meters antennas where it is removed. Although the prism contributes to the noise temperature in several Kelvins and introduces extra reflection losses, it is easy to handle and does not interfere with the vacuum in the cryostat.

Alternatively, the same tilt effect can be achieved by offsetting the lens position. This solution can be implemented using a different holder for 7 and 12-meters antennas causing no extra noise contribution. In order to produce a deflection of 1.8°, it is necessary an offset of 5.66 mm perpendicular to the axis of propagation as shown in figure 3.26. The exact number was obtained simulating with HFSS several models at the lowest frequency with different offset in the lens position. Once the appropriate offset was known, other frequencies were simulated. The aperture efficiencies at 35, 42.5 and 50 GHz as shown in table 3.17. Even if some degradation can be noticed respect to 12-m antennas, all the aperture efficiencies are higher than 80%. Nevertheless, it should be considered that the simulations have not included filter effects, so extra degradation in aperture efficiency could be found in the real system.

3.7 Conclusions

We have presented three optical systems for ALMA Band 1. All the optical systems consists of a compact spline-profile corrugated horn (designed to be machined from a single block); a thin gore-tex membrane and a grooved surface of PTFE as infrared filters at the 15 and 110-K stages, and a low loss HDPE biconvex one-zone lens.

HFSS full system simulations have shown that the best design has an aperture efficiency better than 80.26%, polarization efficiencies better than 99.95% noise temperature contribution lower than 11.3 K and compatible with 7-meter antenna. With these characteristics, it fully complies ALMA specifications.

Chapter 4

Implementation and measurements

This chapter starts with a complete analysis of the main components and error sources of the measurement system. Then, we present the characterization of the material with which the lens was fabricated. In this way, the dielectric constant and the loss tangent will be determined accurately. Later, we present the characterization of the first horn antenna including the radiation pattern. Furthermore, the characterization of two full systems, consisting of the first horn, the infrared filter, the metal rings and the first or second prototype lens are presented. The second horn and the third lens prototypes were under construction at the moment of writing this thesis.

4.1 Implementation

We have implemented the first design of the horn and the first and second designs of the lens using a CNC lathe machine. The spline-profile corrugated horn was machined from a single block of Duralumin. The two one-zone lenses were made of HDPE. The infrared filters were provided by ALMA. The 15-K filter is made of a 3-mm gore-tex membrane while the 110-K filter is a 8.5-mm grooved surface of Polytetrafluoroethylene (PTFE, also called Teflon).

4.2 Measurement procedure

The optical system and its components were characterized in a beam-pattern scanner. The complete setup was assembled in an optical table in order to ensure the correct position, angle and alignment of all the components. The setup was enclose in an Anechoic chamber and uses a near-field planar beam scanner setup built specifically for this work. The system consists on a transmitting 30–50 GHz probe attached to a $XY\theta$ scanner, an XY scan controller, an Agilent 50-GHz Performance Network Analyzer (PNA) and a PC, as shown in figure 4.1.

The probe antenna assembled in the $XY\theta$ scanner samples a perpendicular plane with respect to the axis of propagation while the DUT is fixed. The reference point to calculate the equidistant

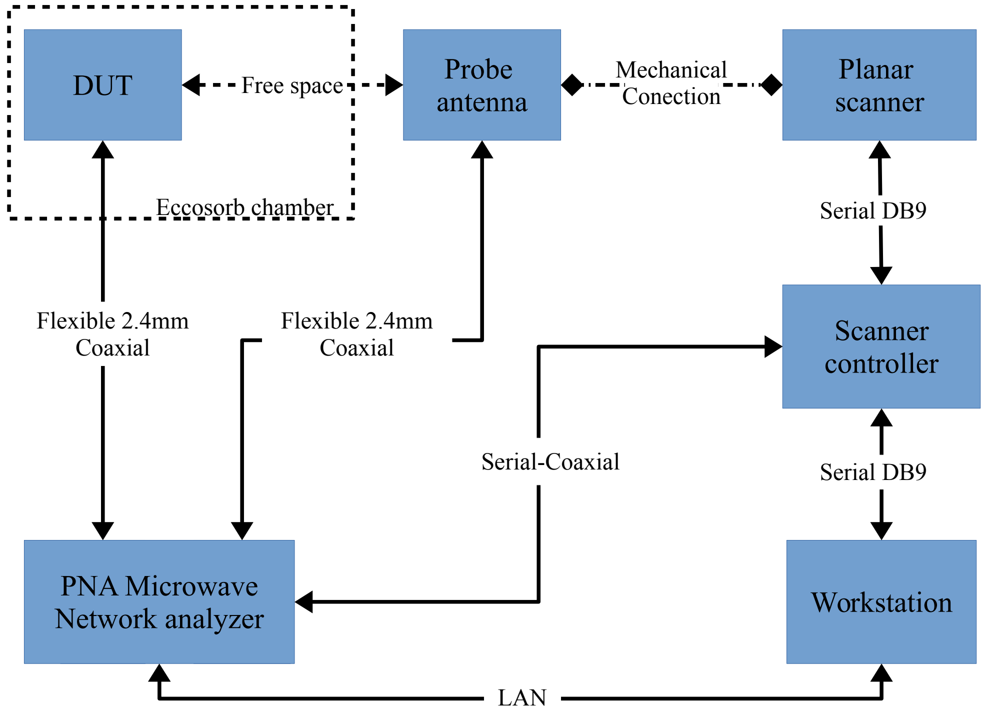

Figure 4.1: Beam scanner schematic. The system consist in a beam-pattern setup at 30–50 GHz. It is divided in five subsytems, the anechoic chamber including the DUT, the planar scanner including the probe antenna, the scanner controller, the PNA Microwave network analyzer and a workstation including Labview and MatLab softwares.

square plane of measurement was chosen colinear to the center of the horn and lens. This plane is defined by the distance between the aperture of antenna and the top of the lens, as well as the angle for measuring at least the first side lobe. Each sampled point is separated by $0.48 \cdot \lambda$ in order to meet the Nyquist criterion. [1] The PNA reads and saves the S-parameters and sends a trigger signal to the scanner controller at the end of the process. When the controller receives the trigger signal, it waits 0.5 s and then provides the instructions to go to the next position. The wait time between a measuring point and the next one was calculated for the cables stop moving and minimize phase errors. The probe antenna moves in horizontal lines, starting from the top-right point and changing direction after finishing each line. The complete process is automatically controlled by a software developed in Labview. When the measurements are finished, the PNA sends all the data at the workstation where they are post-processed. The near-field data transformed into far-field data using an algorithm based on Fast Fourier Transform [48]. The final far-field data from the beam scanner software has a resolution of 0.2°.

4.2.1 Alignment error sources

There are several possible sources of error in the measurement of the beam pattern due to the

[1]The Nyquist criterion establishes that the minimum sampling rate to preserve the signal information is two times the signal bandwidth, or equivalently, half its wavelength [46] [47].

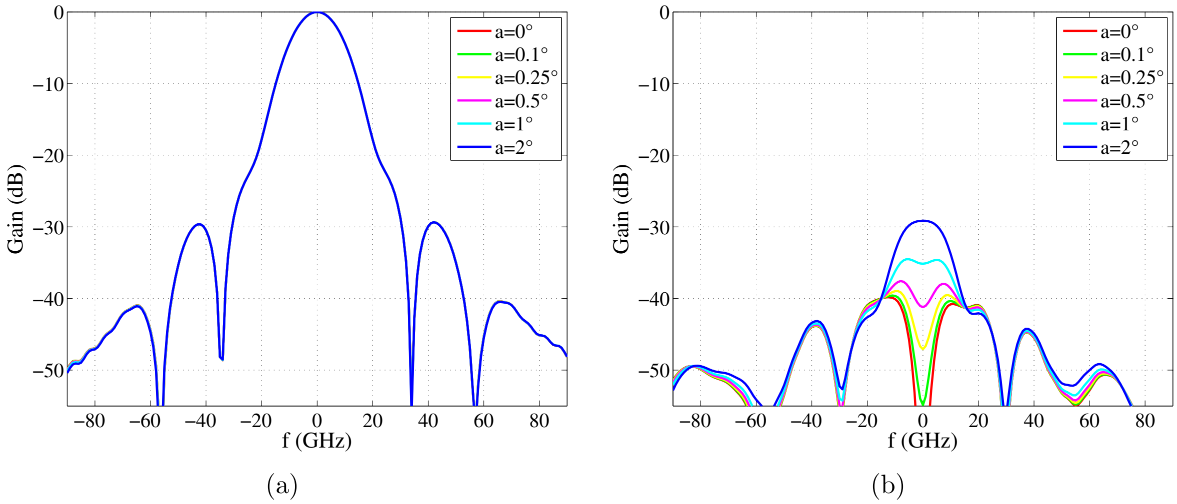

Figure 4.2: Simulated effect in radiation pattern due to error in the probe antenna rotation (a) co-polarization and (b) cross-polarization pattern.

setup. The alignment between optical devices is guaranteed by the test bench. However, the center point and alignment of the beam scanner are set manually (using traditional tools as level, plumb and square) which can lead to errors in centering and beam scanner-test bench planarity. We estimated that the planarity error is $\pm 0.5°$. Moreover, the probe is rotated manually to measure cross-polarization. By simulation it was estimated that an error of 1° introduces 5 dB extra in the measurement as shown figure 4.2.

4.2.2 Stability of the measurement

A test was conducted to study the stability of the measurement system. It consisted on measuring at a fixed point the S-parameter for 16 hours saving samples every second and also registering the temperature with a sensor in the table where the setup was mounted. This measurement started at 6 pm and ended at 10 am and the results are summarized in figure 4.3. It can be clearly seen that there is a dependence phase on the room temperature. In contrast, it was found that the same variations in temperature did not produce any important variation in the amplitude, only a variation of 0.21 dB was registered in 16 hours and a maximum fluctuation second to second of 0.06 dB. Usual measurements take around 5 hours per polarization, so less than 0.1 dB should be considered. The change in temperature, on the contrary, produces an important systematic variation in the phase measurement. The worst case in a standard 5-hours measurement should consider a maximum variation of around 6° and a maximum fluctuation second to second of 0.6°. In principle the offset can be corrected considering the recorded change in temperature.

The results shown in this thesis do not have the phase correction since the optical systems were measured before discovering this source of error, hence, the temperatures were not registered. In any case, for calculating efficiencies the useful area of the measured radiation pattern is small, consequently it is expected that the phase error is minor. Anyway, a phase correction procedure will be implemented in future measurements.

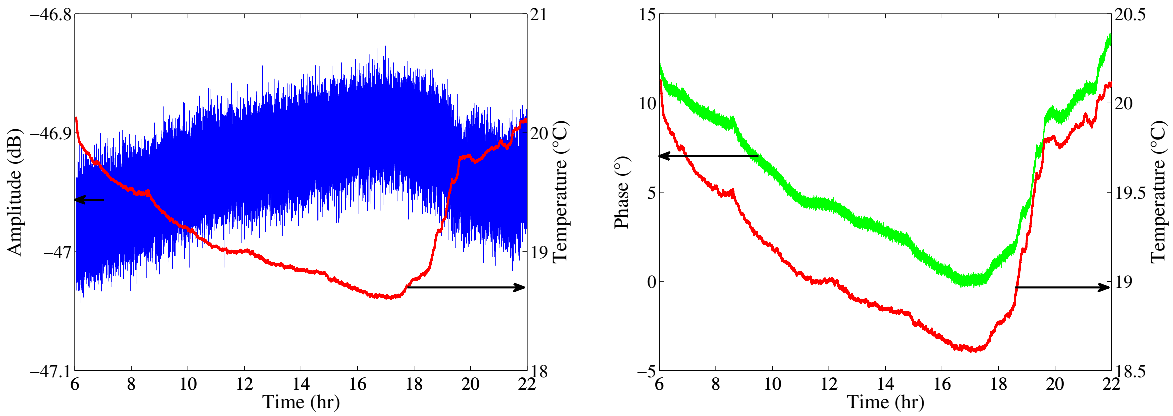

(a) (b)

Figure 4.3: Stability for 16 hours of the measurement. (a) Amplitude and (b) phase stability.

4.2.3 Other assumptions

Some assumptions were made regarding the post-processing analysis. First, the plane in the transformation is assumed to be infinite when obviously, the measurement was made in a finite plane; hence, only a limited section of the plane was useful. Another error comes from the shape of the pattern of the probe. Even though the probe antenna has a very isotropic radiation pattern, it is convoluted with the pattern to be measured producing some distortions and requiring to be compensate to obtain error-free patterns.

4.3 HDPE characterization

The characteristics of the used HDPE is critical in the design of the lens, since the dielectric constant affects the focus of the devices and the loss tangent determines the addition of noise temperature by dielectric losses. Using the procedure presented in section 2.3.1 for a waveguide WR–22 of 40 mm and the same PNA of the beam scanner setup, several samples of the HDPE were measured.

A sample of material was measured for the first lens giving $\varepsilon_r = 2.232$ and a $\tan\delta = 2.33 \cdot 10^{-4}$. Some differences between simulation and measurement were found when the lens was characterized. A more careful analysis of the samples showed that small air gaps changed the estimated value. Simulations were conducted in order to estimate the impact on the properties of the lens due to an error in the estimation of the dielectric constant. Figure 4.6 shows the change in efficiency when the lens is designed to $\varepsilon_r = 2.232$ but the real dielectric value is different. An important conclusion of that is the allowable error in the dielectric constant is ± 0.01 which degrades the aperture efficiency less than 0.2%.

For the second lens new samples of material were measured. The material comes from the same batch as the first one. The samples were taken from different positions of the same face of the block of HDPE, and the construction procedure of the sample was improved. The mean values obtained

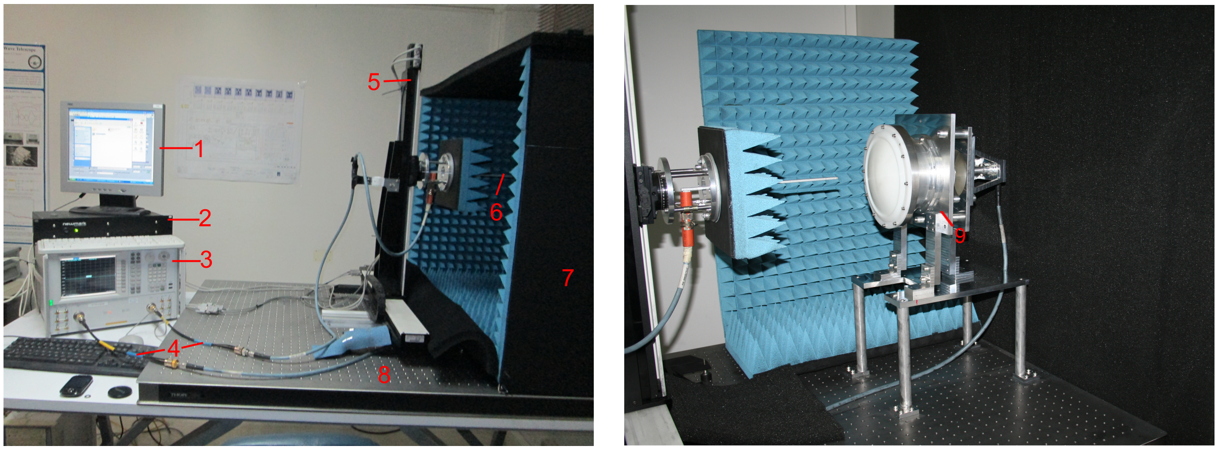

(a) Full Setup. (b) Test-bench including lens, infrared filters and horn antenna.

Figure 4.4: Nearfield beam scanner setup. 1: Workstation (PC including MATLAB and LabVIEW software), 2: XY scanner controler, 3: Agilent 10-MHz-50-GHz PNA, 4: flexible coxial cable, 5: XYθ scanner, 6: probe antenna, 7: Eccosorb chamber, 8: optical table, 9:DUT (test-bench).

were $\varepsilon_r = 2.347$ and $\tan\delta = 2.23 \cdot 10^{-4}$.

Finally, a new batch of material was bought for the last lens design. In this case 12 samples were measured. They were selected more independently, including variations in position and angle, as shown figure 4.5. Also, each sample was measured twice, performing the full assembly, in order to ensure the repeatably of the measure and reduce the random error. The mean values obtained were $\varepsilon_r = 2.347$ and $\tan\delta = 2.23 \cdot 10^{-4}$.

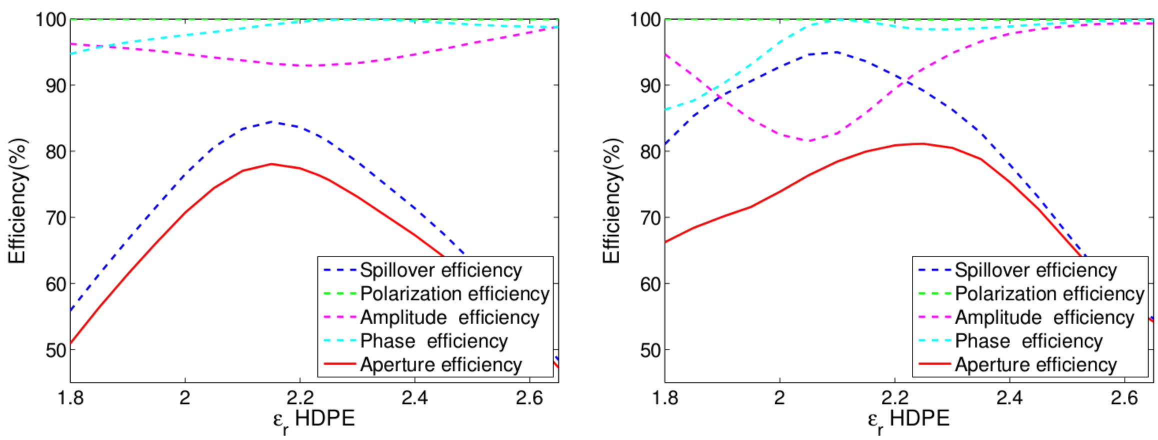

(a) Simulated at 35 GHz (b) Simulated at 50 GHz

Figure 4.6: Impact of error in the dielectric constant estimation to the aperture efficiency. (a) Simulations at 35 GHz and (b) Simulations at 50 GHz.

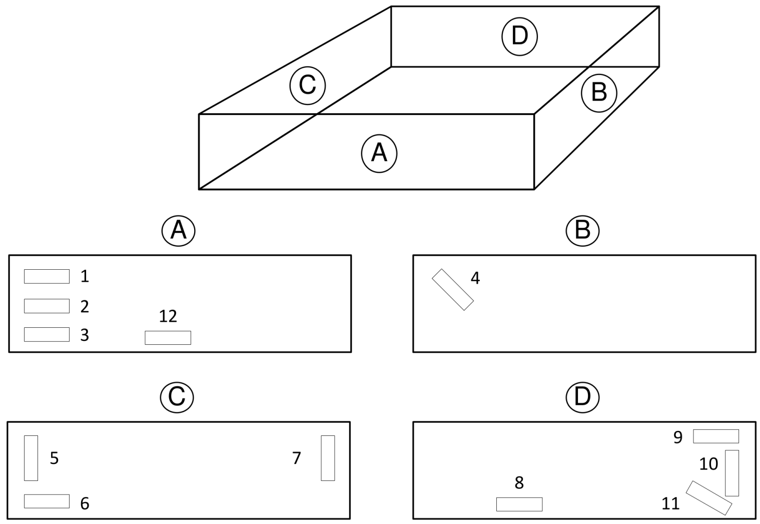

Figure 4.5: Position and orientation of HDPE samples.

4.4 Horn v1

4.4.1 Construction procedure

The antenna was constructed using a block of duralumin in a CNC lathe. The manufacture was in charge of Consmat, a Chilean company dedicated to the metal-mechanic manufacture. Several prototypes were constructed and cut to perform metrological analyses in order to ensure the correct manufacture of the antenna. A comparison between the first and the last test prototype are shown in figure 4.7. The first prototypes presented errors in the dimension of teeth, gaps and depths, and major deformations in the geometry of the corrugation. The last test prototype showed a better performance avoiding dimension errors, but including a small deformation in the teeth slightly on tolerance of construction. This deformation is generated due to the fact that the machining tool has a radius of curvature that produces a non-straight cut at the end of the teeth. It can be easily corrected if the tool exceeds the limit end of the teeth. This instruction was given to the construction company. It was corrected then in the final prototype in order to be measured in the beam scanner. Figure 4.8 shows the constructed prototype ready to be electromagnetically characterized.

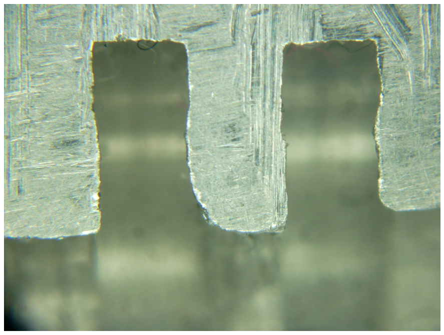

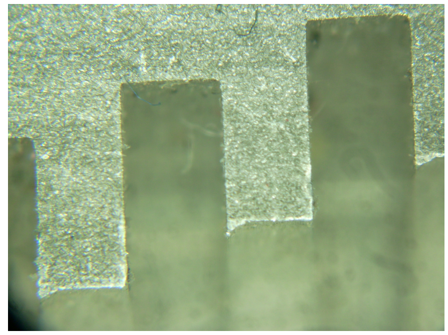

(a) (b)

Figure 4.7: Zoom to the cross-section of constructed horn v1 to analysis fabrication quality.(a) First test prototype (b) Last test prototype

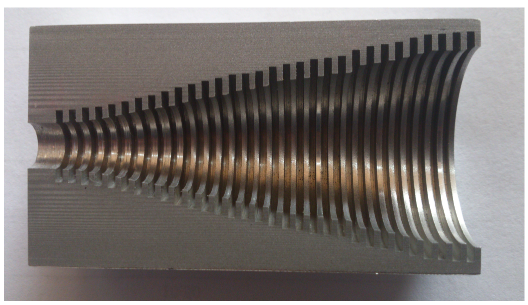

(a) (b)

Figure 4.8: Constructed horn v1.(a) Cross-section of horn v1 (b) Prototype of horn v1

4.4.2 Electromagnetic characterization of horn v1

The simulated and measured radiation patterns of horn v1 are pretty similar. They are identical up to –20 dB with minor differences between the level of the shoulders. The co-polarization patterns have also very good symmetry. In contrast, mayor differences can be noticed in cross-polarization. The largest difference between the maximums is about 4 dB. The cross-polarization measurement is very sensitive, large variations in their level are produced by any small error in the measurement setup, as explained above in section 4.2.1. The PCL was calculated using a phase model with weighting correction [49][14], the calculated values agree very well with simulation with ±1 mm. In table 4.1 a summary of the main measured parameters is presented.

The simulated and measured reflection losses between 35–50 GHz are shown in figure 4.10. The measurement was performance with 50 MHz resolution in the maximum frequency range allowed by the PNA. The measured S_{11} is better than –28 dB. HFSS simulations predicted reflection losses better than –29 dB and MMW a maximum of –28 dB. Although the curves are different at some frequencies, they present a similar structure. The most important difference are the bumps between 36.5 and 38.5 which is 3 dB about the predicted value, overpassing the design goals of –30 dB. This suggests small differences between the designed horn and the constructed one. Nonetheless, the measured values present excellent reflection losses for the full band of interest.

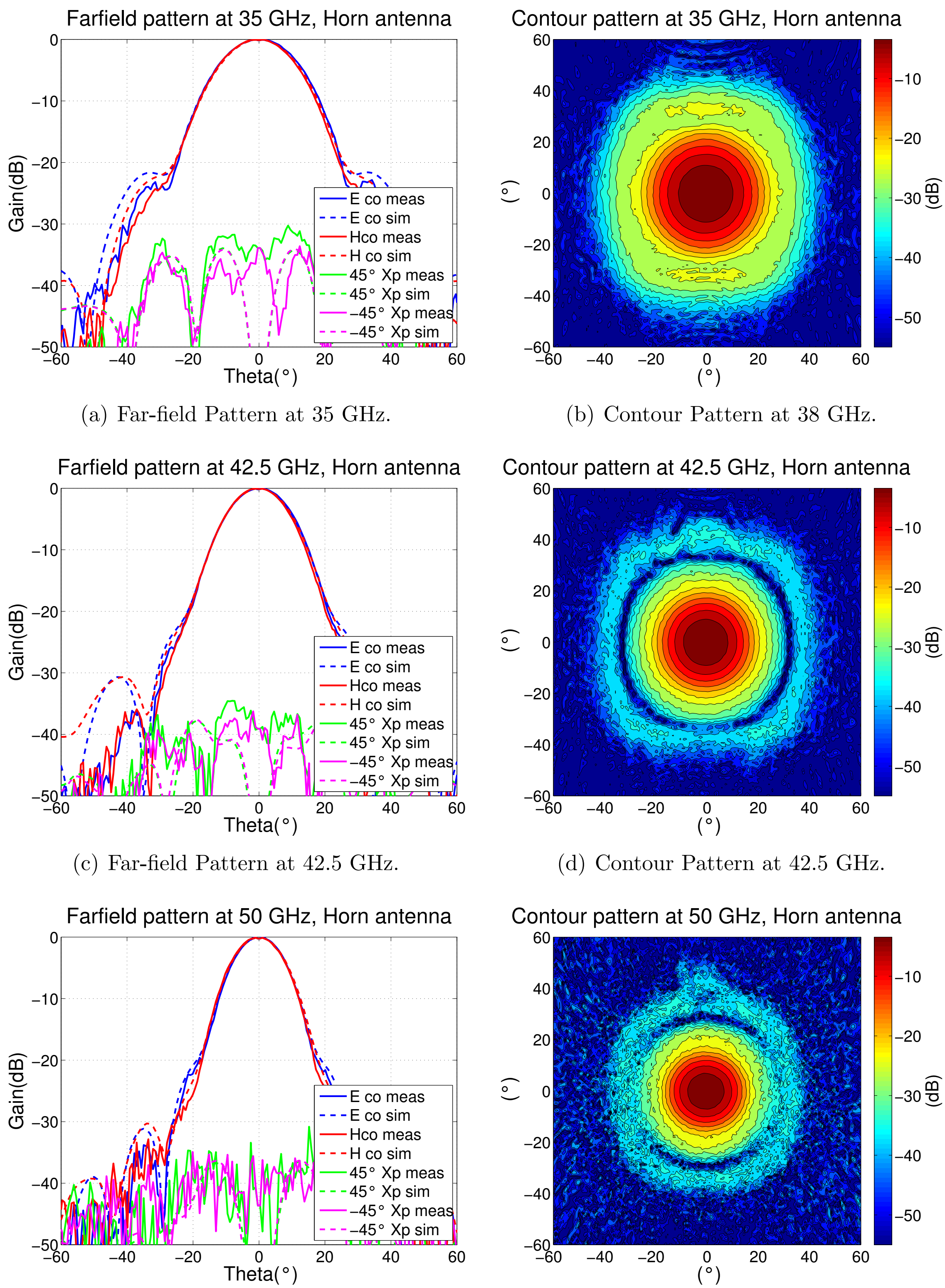

(a) Far-field Pattern at 35 GHz.

(b) Contour Pattern at 38 GHz.

(c) Far-field Pattern at 42.5 GHz.

(d) Contour Pattern at 42.5 GHz.

(e) Far-field Pattern at 50 GHz.

(f) Contour Pattern at 50 GHz.

Figure 4.9: Measured far-field patterns at 35, 42.5 and 50 GHz for the first spline corrugated horn design.

Table 4.1: Main resulting parameters at 35, 42.5 and 50 GHz of first spline-profile corrugated horn.

Freq (GHz)	Shoulder level (dB)	XPolar (dB)	10 dB point (dB)	BW E (mm)	BW H (mm)	PCL E (mm)	PCL H (mm)
35	−22.9	−30.3	18.1	9.52	9.36	6.30	5.31
42.5	−19.8	−34.3	14.8	9.46	9.40	8.91	8.25
50	−17.7	−30.8	12.4	9.45	9.52	11.17	12.19

4.5 Full System

4.5.1 Lens construction

The lenses was construted in a CNC lathe using a block of HDPE that was previously characterized as shows section 4.3. The manufacture was provided for Pimet, a chilean company dedicated to highly specialized instrumentation manufacture. Unlike the procedure in the horn construction, no iterations were performed. We do not have a system that allows fully dimensional characterization of the lenses. Instead, partial measurement were performed such as thickness, radius, planarity of the mechanical support flange and dimension of some corrugations. Considering these measurement, the constructed lenses have the requested tolerances. Figure 4.11 shows the constructed prototype ready to be electromagnetically characterized.

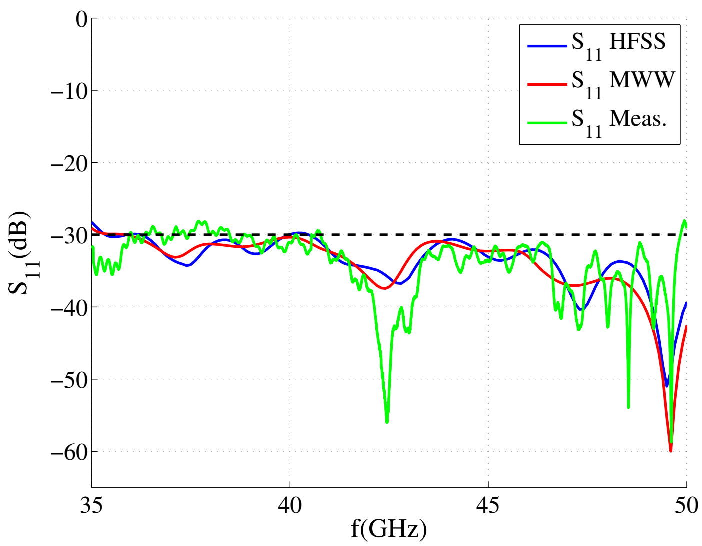

Figure 4.10: Simulated and measured reflection Losses to horn v1 between 35–50 Ghz.

(a)

(b)

Figure 4.11: Constructed lenses mounting in the holder structure. (a) Lens v1 (b) Lens v2

4.5.2 Electromagnetic characterization of full system (lens v1 and horn v1)

The measurements presented here correspond to the full optical system, including lens, infrared filters, horn antenna and all the metal rings. In this case the distance between the aperture probe antenna and the top of the lens was set to 55 cm and it swept a plane of 50×50 cm. The final far-field data from the beam scanner software had a resolution of 0.2°.

Some differences can be noticed respect the simulation results. It must be noticed the effect of the truncation over the 35-GHz pattern in the E-plane, making it considerably wider than the H-plane. The truncation effects are not critical at other frequencies. However, all the patterns present an increase in the cross-polarization level being the largest at 50 GHz.

The phase of the near-field pattern shows some deformations. Asymmetries and bumps between the plane E and H can be observed, and also between the positive and negative side of the curves, presumably caused by the phase instability originated in the temperature variation during the measurements. Moreover, an inclination respect the x-axis can be seen in the H-plane curves, mainly corresponding to misalignment in planarity. All the pattern have phase irregularities, but they are most obvious at the lower frequencies as shown in figure 4.12(e).

The simulated and measured aperture efficiencies are shown in table 4.2. The maximum difference in the calculated aperture efficiency is 1.42%. The discrepancy can be explained by several reasons. As mentioned above, the measurements have some error sources and simulations have some limitations. Moreover, the simulations do not include the full system (they only include the horn, lens and metallic ring). Finally, the simulation and measured was calculated using a different integration area, the reasons have been explained in section 3.3.1 and 4.2 respectively.

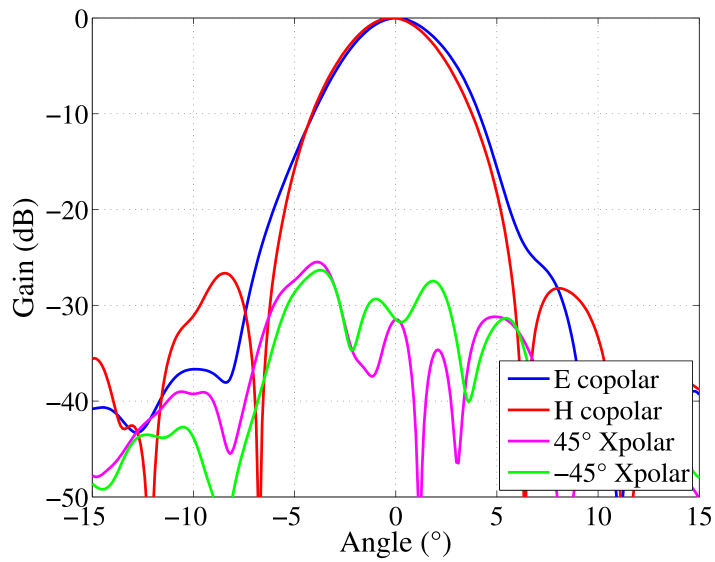

(a) Far-field Pattern at 35 GHz.

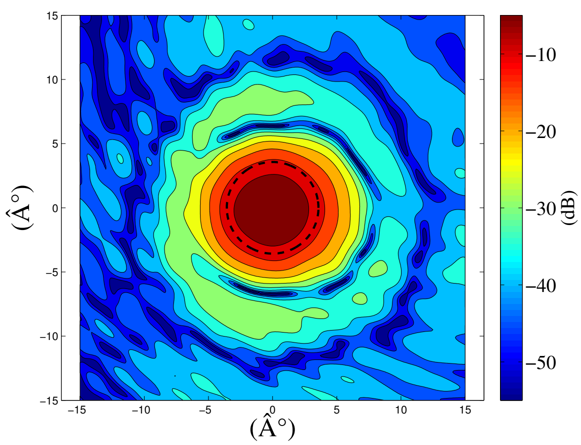

(b) Co-polar Pattern at 35 GHz.

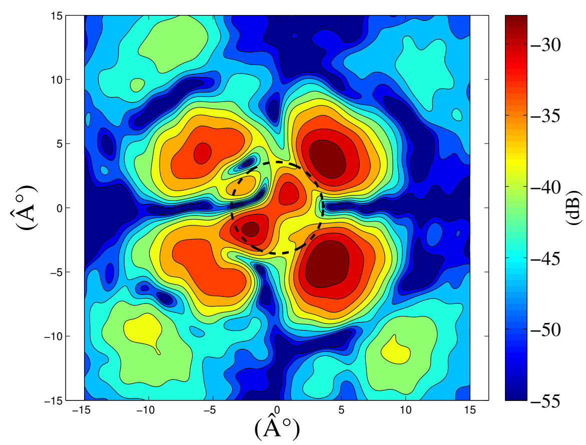

(c) Cross-polar Pattern at 35 GHz.

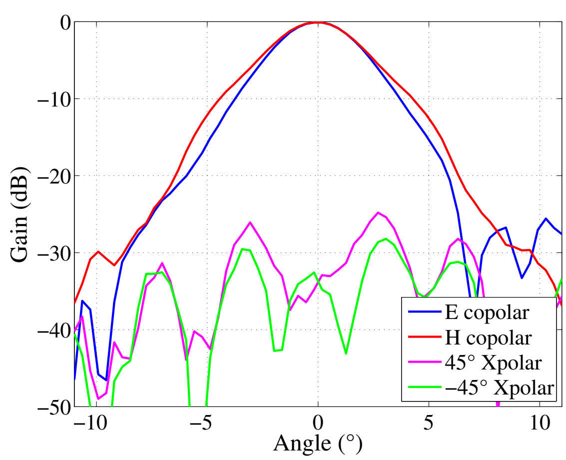

(d) Near-field pattern at 35 GHz.

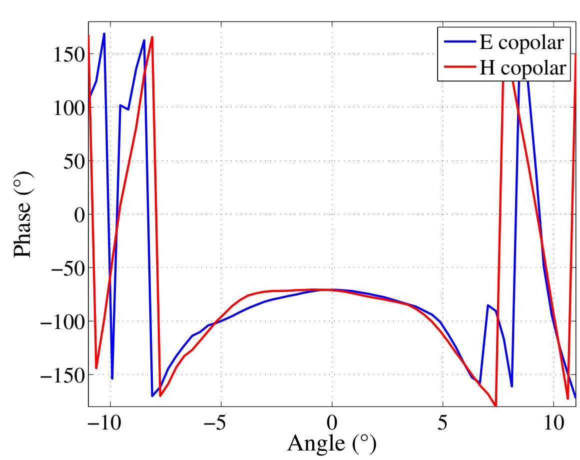

(e) Near-field phase at 35 GHz.

Figure 4.12: Measured far-field patterns at 35 for the horn v1 and lens v1. The black dot circle represent the subreflector dish.

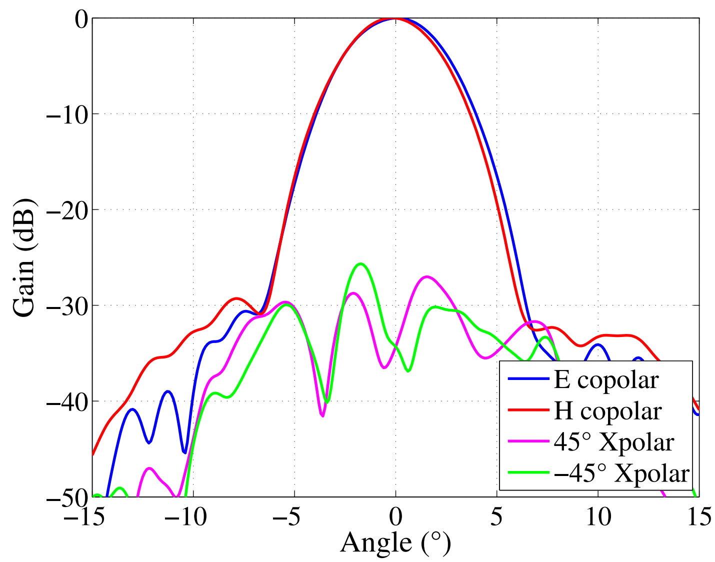

(a) Far-field Pattern at 42.5 GHz.

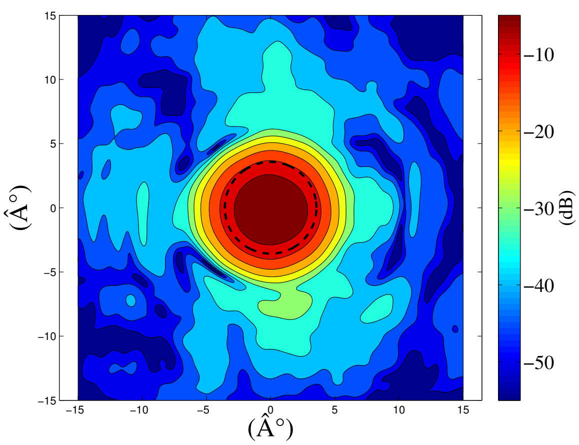

(b) Co-polar Pattern at 42.5 GHz.

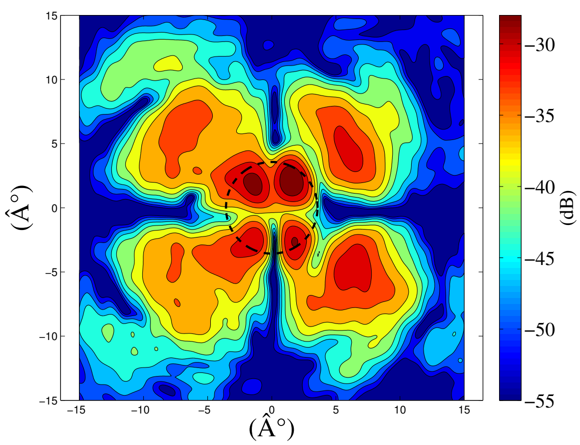

(c) Cross-polar Pattern at 42.5 GHz.

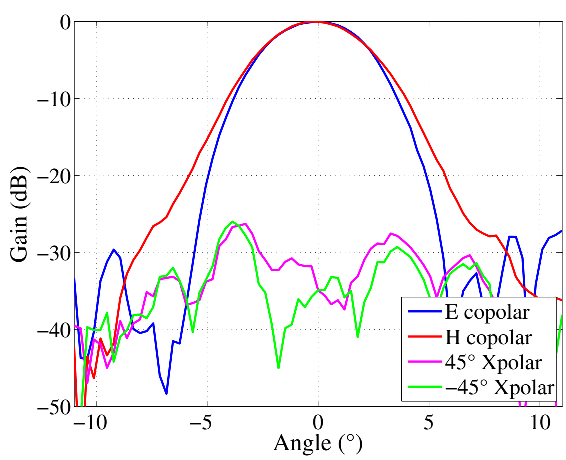

(d) Near-field pattern at 42.5 GHz.

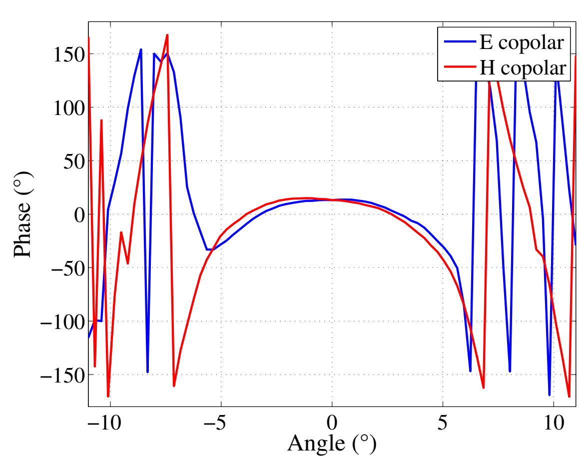

(e) Near-field phase at 42.5 GHz.

Figure 4.13: Measured far-field patterns at 42.5 for the horn v1 and lens v1. The black dot circle represent the subreflector dish.

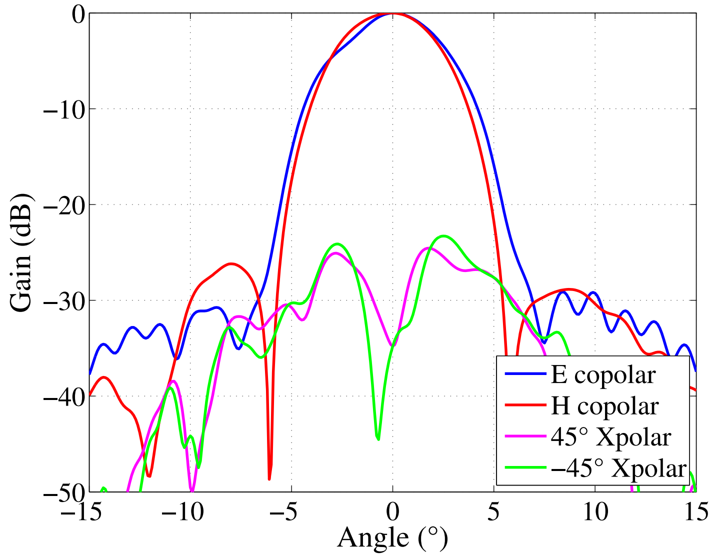

(a) Far-field Pattern at 50 GHz.

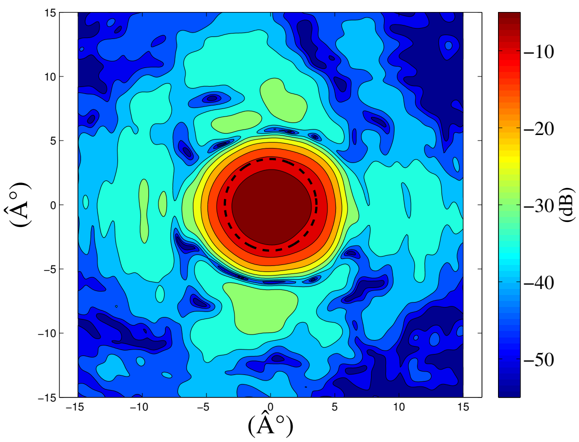

(b) Co-polar Pattern at 50 GHz.

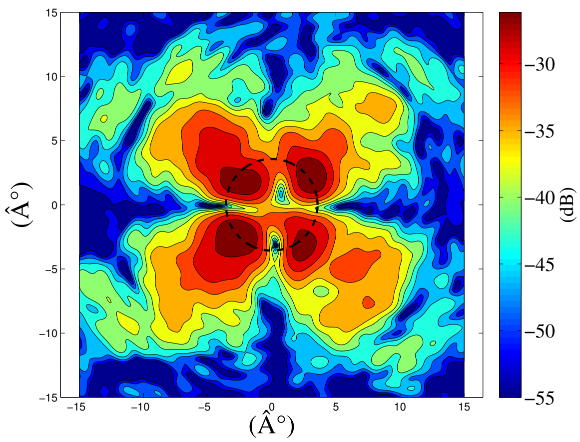

(c) Cross-polar Pattern at 50 GHz.

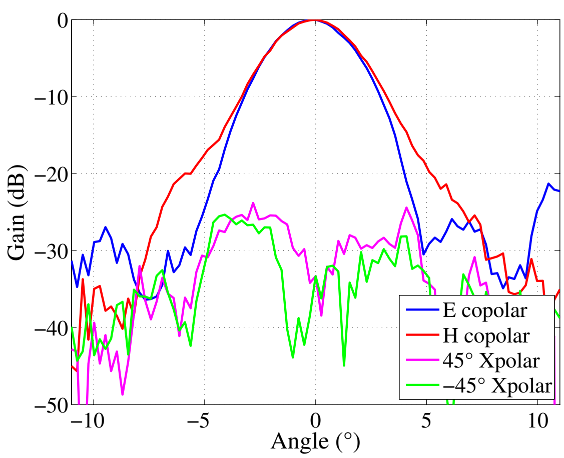

(d) Near-field pattern at 50 GHz.

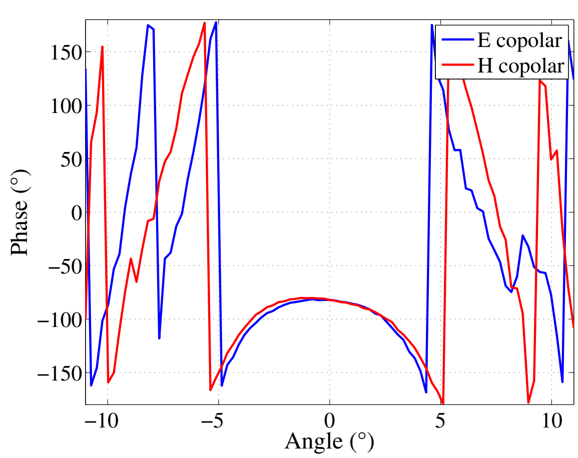

(e) Near-field phase at 50 GHz.

Figure 4.14: Measured far-field patterns at 50 for the horn v1 and lens v1. The black dot circle represent the subreflector dish.

Table 4.2: Measured aperture efficiency including Horn v1, One-Zoned Lens f=168 mm d=162.2 mm and metal lens ring.

	Frequency (GHz)	Spillover efficiency (%)	Polarization efficiency (%)	Amplitude efficiency (%)	Phase efficiency (%)	Aperture efficiency (%)
Measured	35	81.18	99.84	93.71	99.88	**75.86**
	42.5	84.32	99.79	93.75	99.65	**78.61**
	50	82.34	99.59	95.13	99.68	**77.76**
Simulated	35	79.01	99.99	95.81	99.94	**75.65**
	42.5	84.00	99.91	93.88	99.49	**78.39**
	50	84.20	99.60	94.77	99.62	**79.18**

4.5.3 Electromagnetic characterization of full system (lens v2 and horn v1)

The measurements presented here correspond to the full optical system, including lens, infrared filters, horn antenna and all the metal rings. In this case the distance between the aperture probe antenna and the top of the lens was set to 83 cm (slightly larger than the distance for the first full system measurement since the new lens has a largest focal length) and it was swept a plane of 75×75 cm. The final far-field data from the beam scanner software had a resolution of 0.2°.

Once more, as predicted by the simulations for this configuration, the truncation effects are lower than the first one. Nevertheless, some deformations can be seen in the pattern of 50 GHz, presumably since the filters were not designed to operate at this frequency. The main difference between the simulation and the measurements are the increment in the cross-polarization level, being critical at 50 GHz.

The near-field phase shows lower errors in phase instability than the first measurement, the bumps are smaller and the curves more symmetric. Nevertheless, the phases present a 1-degree offset in plane-E curve, but do not have any tilt that suggest misalignment in planarity. This can be explained by a small offset of the initial positioning of the probe antenna.

The simulated and measured aperture efficiency are shown in table 4.2. The maximum difference of aperture efficiency is 2.02%. Once more, the discrepancy can be explained by error sources in measurements, the limitations in simulations and also the differences in the used integration area to calculate the efficiencies.

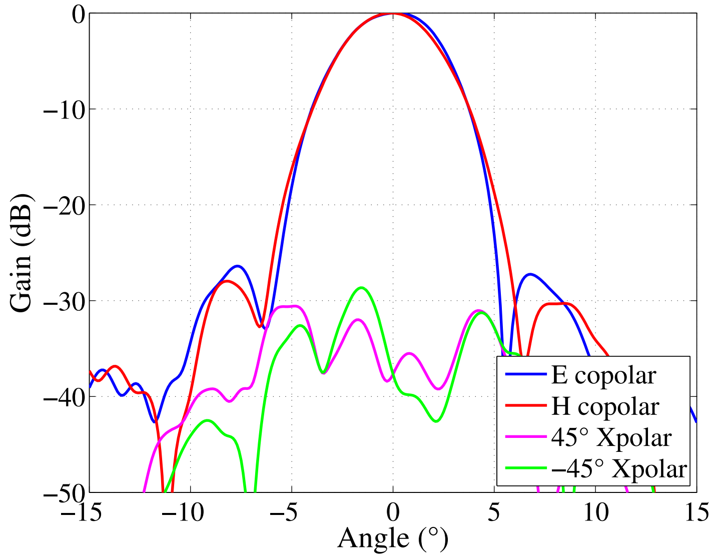

(a) Far-field pattern at 35 GHz.

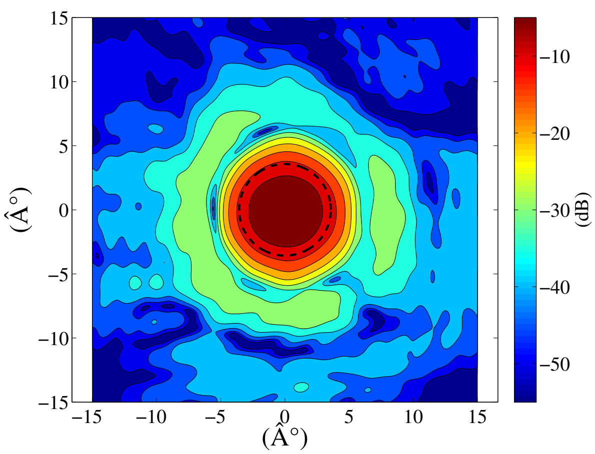

(b) Co-polar pattern at 35 GHz.

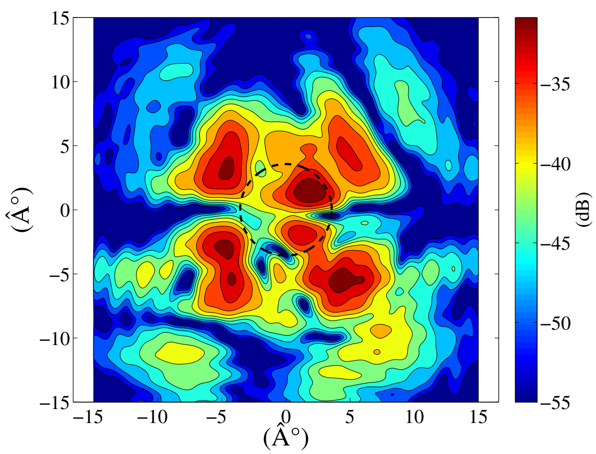

(c) Cross-polar pattern at 35 GHz.

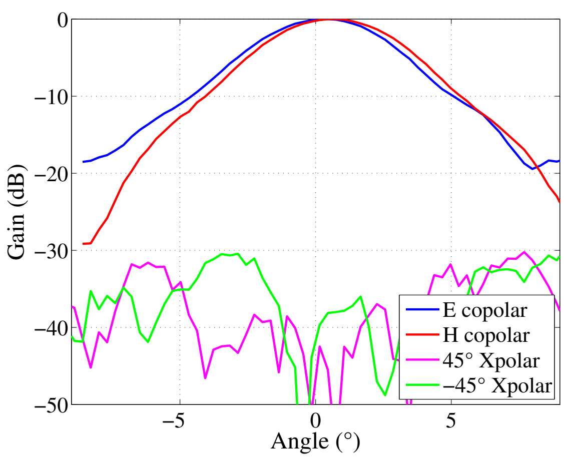

(d) Near-field pattern at 42.5 GHz.

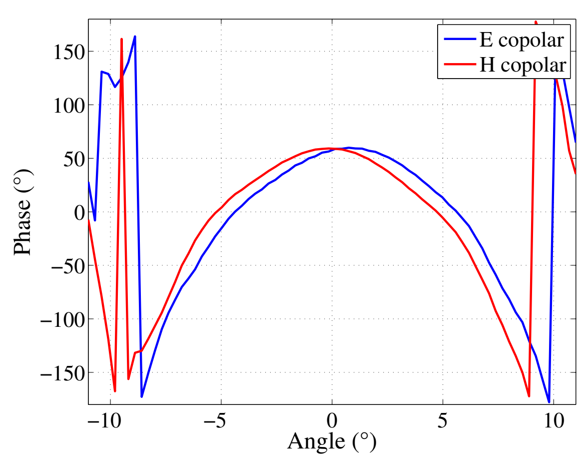

(e) Near-field phase at 42.5 GHz.

Figure 4.15: Measured far-field and near-field patterns at 35 for the horn v1 and lens v2. The black dot circle represent the subreflector dish.

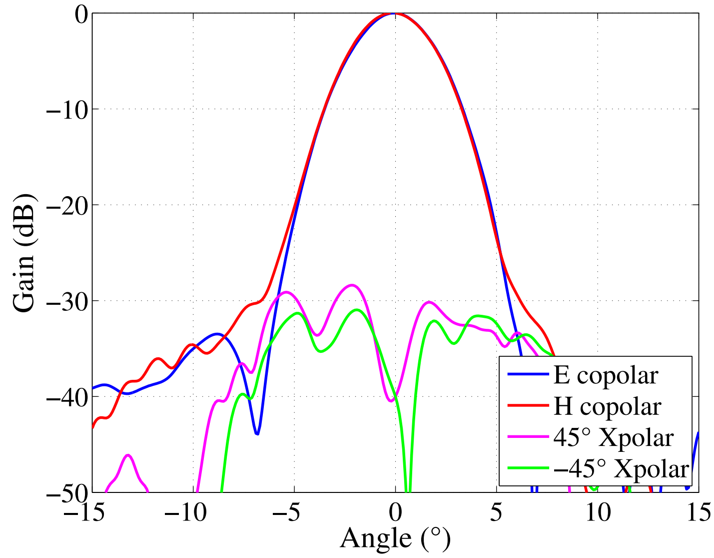

(a) Far-field Pattern at 42.5 GHz.

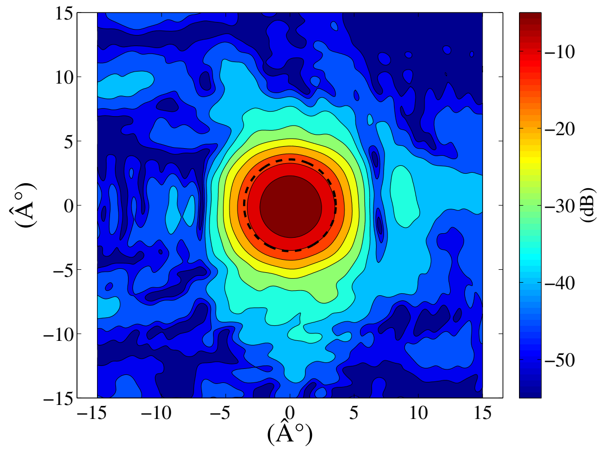

(b) Co-polar Pattern at 42.5 GHz.

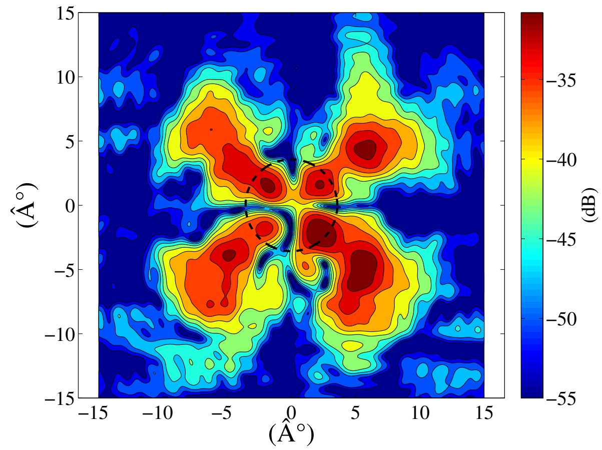

(c) Cross-polar Pattern at 42.5 GHz.

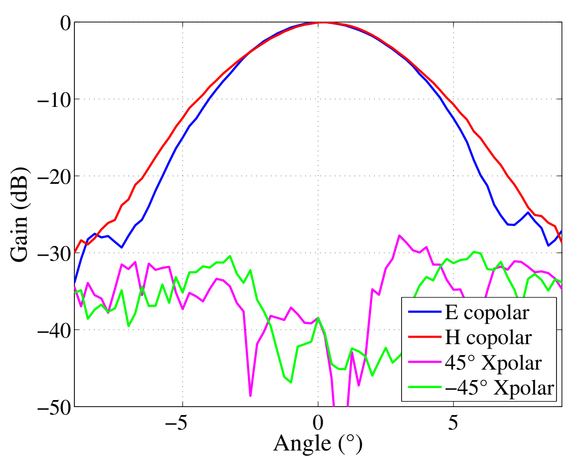

(d) Near-field pattern at 42.5 GHz.

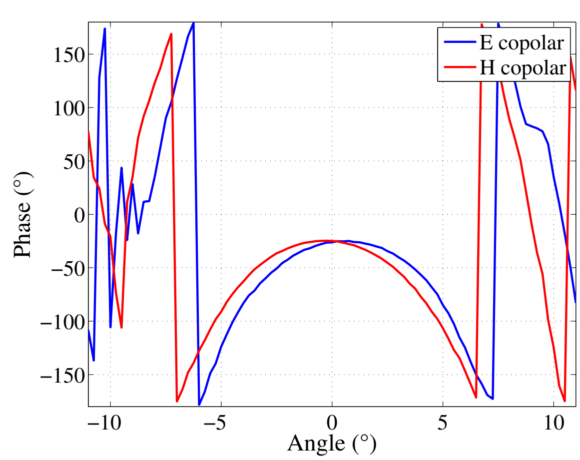

(e) Near-field phase at 42.5 GHz.

Figure 4.16: Measured far-field patterns at 42.5 for the horn v1 and lens v2. The black dot circle represent the subreflector dish.

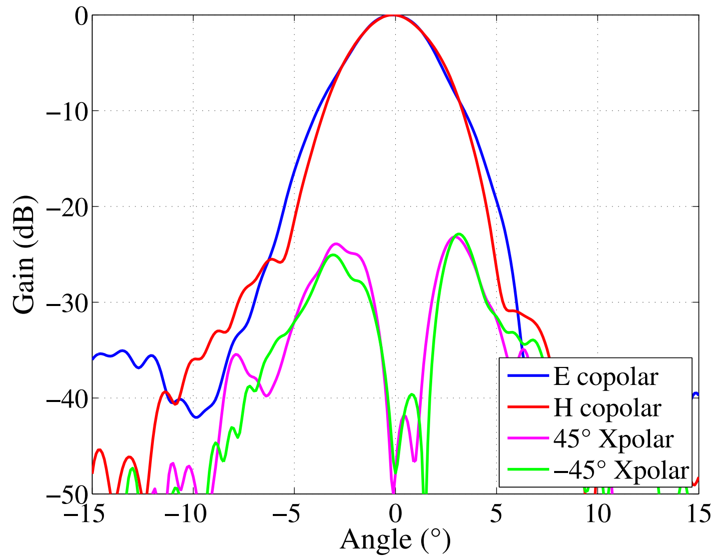

(a) Far-field Pattern at 50 GHz.

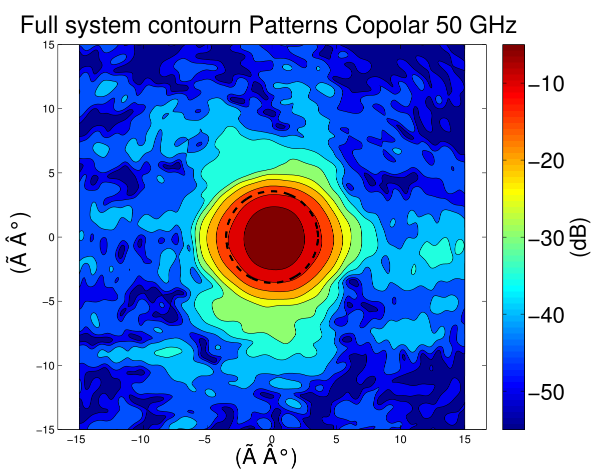

(b) Co-polar Pattern at 50 GHz.

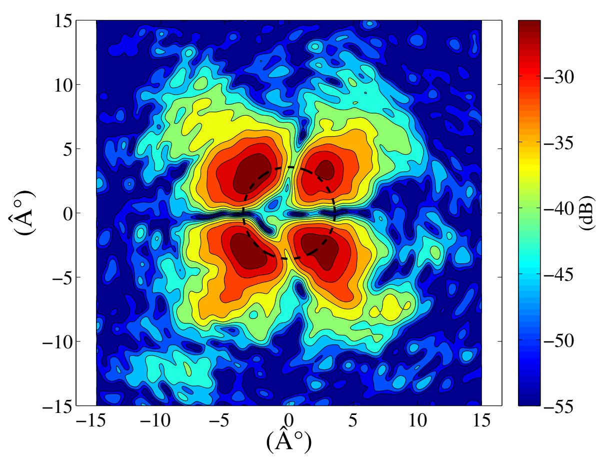

(c) Cross-polar Pattern at 50 GHz.

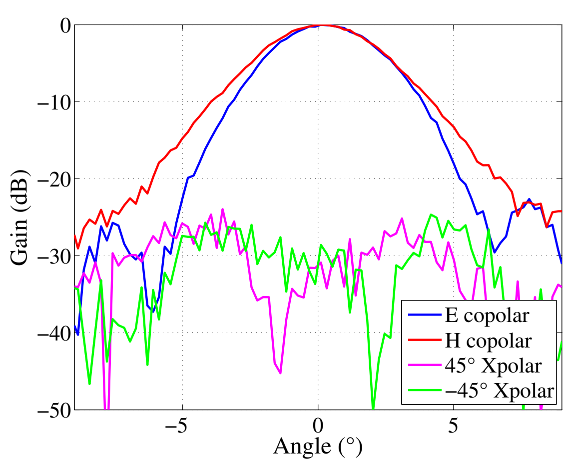

(d) Near-field pattern at 50 GHz.

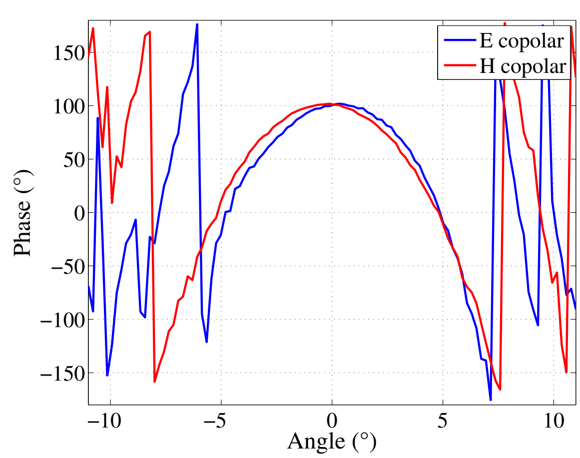

(e) Near-field phase at 50 GHz.

Figure 4.17: Measured far-field patterns at 50 for the horn v1 and lens v2. The black dot circle represent the subreflector dish.

Table 4.3: Measured aperture efficiency including Horn v1, One-Zoned Lens f=165 mm d=164.2 mm and metal lens ring.

	Frequency (GHz)	Spillover efficiency (%)	Polarization efficiency (%)	Amplitude efficiency (%)	Phase efficiency (%)	Aperture efficiency (%)
Measured	35	86.81	99.66	92.72	99.99	**80.21**
	42.5	90.20	99.91	89.28	99.99	**80.45**
	50	89.59	99.84	88.58	99.99	**79.23**
Simulated	35	82.89	99.99	94.61	99.71	**78.19**
	42.5	89.18	99.99	90.03	99.94	**80.77**
	50	89.32	99.94	89.86	99.28	**79.64**

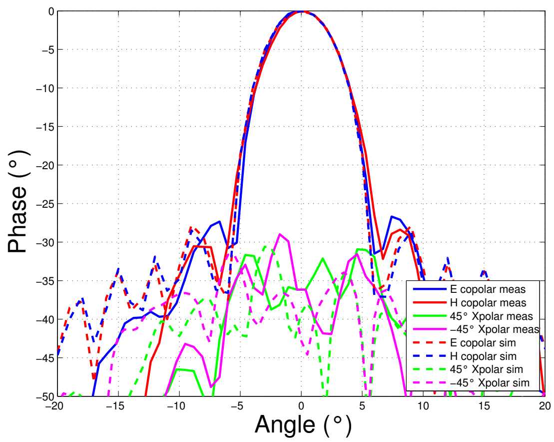

(a) Far-field pattern at 35 GHz.

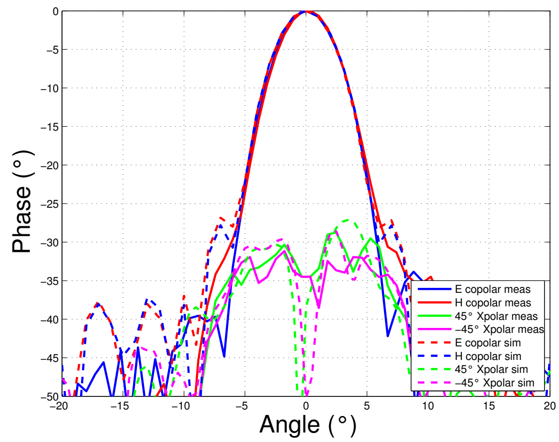

(b) Far-field pattern at 42.5 GHz.

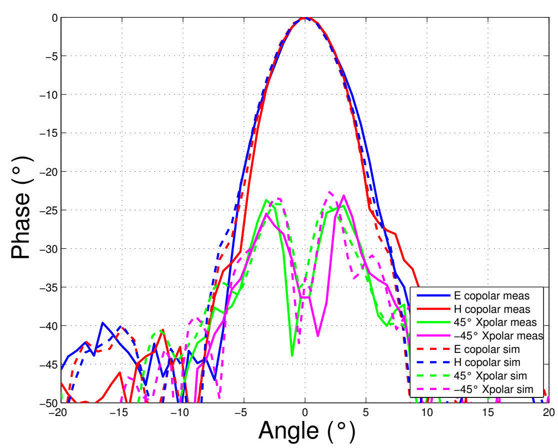

(c) Far-field pattern at 50 GHz.

Figure 4.18: Comparison between HFSS simulated and measured far-field radiation patterns.

Comparison between HFSS simulations and measured farf-field patterns

A comparison between full system HFSS simulations and measured is shown in figure 4.18. The patterns are similar, having a maximum difference of 0.5° in copolar pattern up to –20 dB and a maximum difference between the crosspolar peaks of 3 dB. Nevertheless, it can be appreciated that there are differences in the side lobes, specially at 42.5 GHz in the shoulders. Moreover, at 35 GHz and 50 GHz the measurements present a widening compared to the simulated patterns. These dissimilarity can be attributed to the devices in the path that are not included in the simulation (the holder of the lens and support structures of the IR filters), the sources of error in measured explained in section 4.2 and the simplification in the simulation mentioned in 3.3.1.

4.6 Conclusion

In this chapter we have presented the characterization results of the HDPE used to make the lens, the prototype spline-profile corrugated horn and two zoned bi-hyperbolic lenses. The measured values of the HDPE samples were $\varepsilon_r = 2.347$ and $\tan\delta = 2.23 \cdot 10^{-4}$ using 12 independent samples.

The simulated and measured beam patterns of the horn are pretty similar including good symmetry and lower side lobes. The differences to –20 dB between the copolar are lower than 1° and the difference between the maximums crosspolar about 4 dB.

The measured aperture efficiency was better than 79.2% across the band, and above 80% for most of the band. Moreover, the HFSS simulation and measurements matched within 1.5%.

Furthermore, we have identified the main sources of error in the measurements, they are the instability of phase and alignment error. We have proposed to correct the first one using an additional measurement of the temperature. The second correction requires more careful assembling strategies and equipment.

Chapter 5

Conclusions and further work

We have presented the design, implementation and characterization of the optical system for ALMA Band 1 that covers the frequency range of 35–50 GHz fully complain the ALMA specifications. The optical system consists of a compact spline-profile corrugated horn (machined from a single block of dura-aluminum), a thin gore-tex membrane and a grooved surface of PTFE as infrared filters at the 15 and 110-K stages respectively, and a low-loss HDPE biconvex one-zone lens.

In order to achieve the final design, several iterations were performed. In the process the main constraints and possible improvements were identified and included in the final prototypes. The major limitations were the electrical small apertures and the limited space between horn and lens. Moreover, an extra difficulty was found, usual softwares for electromagnetic design do not exhibit optimum performance for large electrical structures being excited by radiation.

An important result of this thesis consisted on demonstrating that it is possible to achieve excellent performance in broad bandwidth, using compact horns that can be easily machined in a CNC lathe. Another import result was to show that properly choosing the parameters of the lens, a zoned lens can provide a very good performance at reduced noise temperature, even in broad bandwidth designs.

Two horn antennas and three one-zoned lenses were presented. The best configuration presented consisted on the second spline corrugated horn and the third version of the lens. For this configuration, the simulated aperture efficiencies were greater than 80.4%, considering HFSS simulations, and better than 81.5%, according WaspNET simulations. These values fully complies ALMA specifications.

We have prototyped a spline-profile corrugated horn and two one-zoned bi-hyperbolic lenses. The measured aperture efficiency was better than 79.2% across the band, and above 80% for most of the band for the best configuration. Moreover, the HFSS simulation and measurements matched within 1.5%. Nevertheless, important upgrades in the measurement system are required in order to guarantee accurate results.

The estimated noise temperature was 10.4 K in average, where the lens is the principal contributing device (about 7 K). Accordingly, we have taken all the possible measures to reduce its noise contribution. Those measures included reducing the thickness of the lens, using a one-zone and choosing a low-loss material.

Although the resulting models using HFSS achieved reasonably good designs, the amount of RAM memory and time required for each simulation limited the design process. More exotic designs could be explored with faster simulation tools and more computing resources.

As future work, we must, first, implement the best design achieved and characterize it. Then, it is necessary to implement the appropriate improvements in the measuring system in order to produce more accurate far-field patterns. Finally, it is important to note that the results presented in this thesis and the future work will be included in the Critical Design Review (CDR) of ALMA Band 1 to be held in Taiwan in December 2015.

Appendix A

Horn v1, technical drawing

N°	R mm	r mm	Ro mm	G mm	C mm
1	6.47	3.50			
2	6.28	3.96			
3	6.24	4.06			
4	6.32	4.33			
5	6.67	4.80			
6	7.15	5.29			
7	7.70	5.82			
8	8.13	6.22			
9	8.70	6.91			
10	9.34	7.58			
11	9.87	8.13			
12	10.32	8.44			
13	10.74	8.79			
14	11.26	9.45			
15	11.40	9.69			
16	11.80	10.13	3.35	1.22	0.9
17	12.43	10.97			
18	12.81	11.16			
19	13.15	11.39			
20	13.54	11.60			
21	13.73	12.02			
22	13.97	12.09			
23	14.82	13.26			
24	15.35	13.55			
25	15.61	13.71			
26	15.92	14.33			
27	16.50	14.86			
28	16.99	15.40			
29	17.08	15.32			
30	17.29	15.32			
31	17.37	15.84			

Horn granet Rrm9_1_N

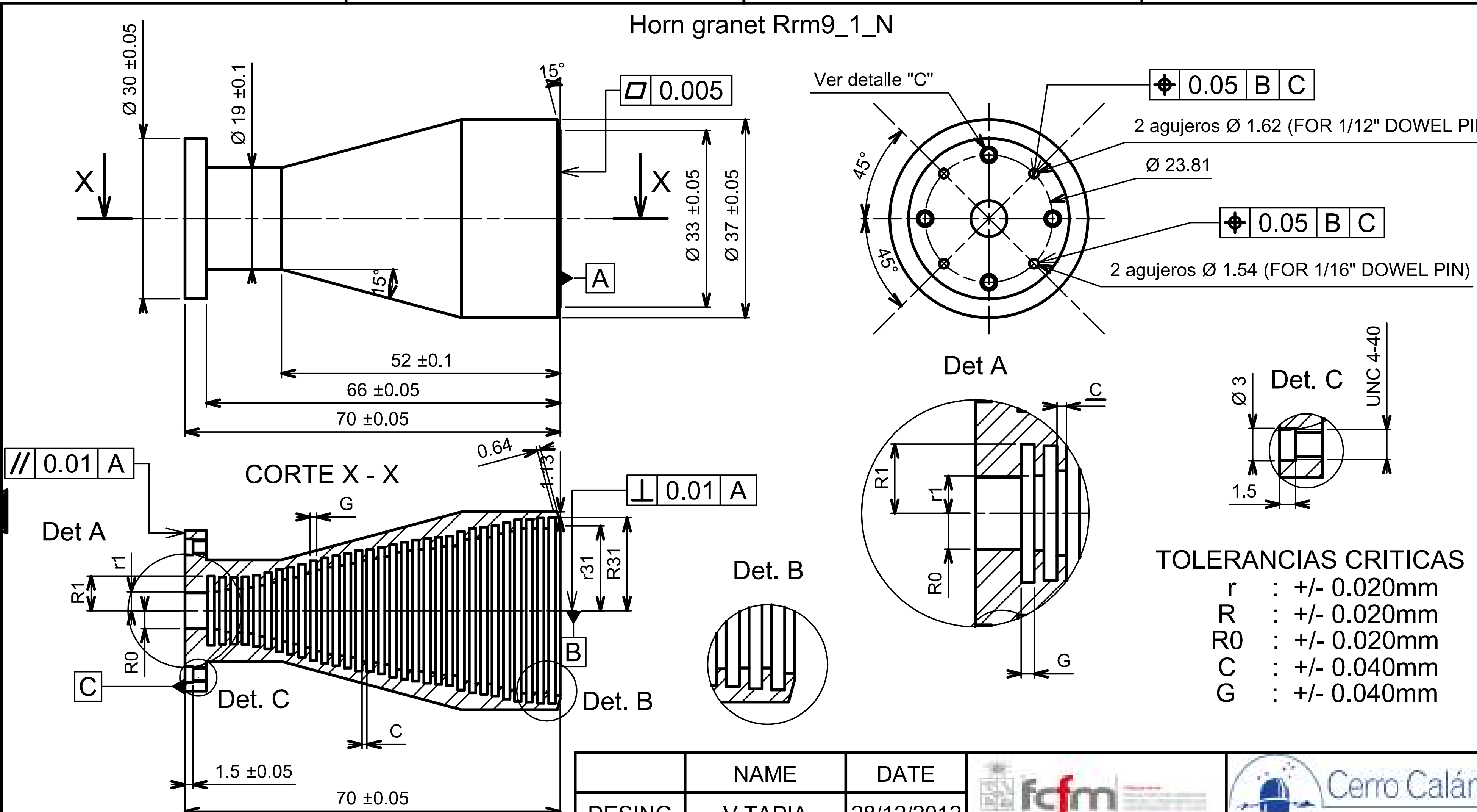

TOLERANCIAS CRITICAS

r	:	+/- 0.020mm
R	:	+/- 0.020mm
R0	:	+/- 0.020mm
C	:	+/- 0.040mm
G	:	+/- 0.040mm

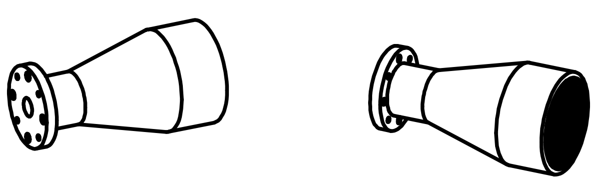

	NAME	DATE
DESING	V.TAPIA	28/12/2012
DRAWN	J.PIZARRO	24/04/2013
REVISED	N.REYES	24/04/2013

Material: Duraluminio

fcfm — Cerro Calán, Observatorio Astronómico Nacional

TITLE: BANDA 1

DWG N° HORN

SCALE 1:1

SHEET 1 OF 1

Appendix B

Horn v2, technical drawing

N°	R mm	r mm	Ro mm	G mm	C mm
1	6.65	3.49		0.93	1.06
2	6.47	4.01		0.8	1.17
3	6.41	4.14		0.93	1.28
4	6.33	4.23		0.83	1.3
5	6.55	4.79		0.85	1.3
6	7.01	5.19		0.8	1.16
7	7.63	5.77		0.8	1.35
8	8.31	6.45		0.8	1.35
9	8.86	6.98		0.8	1.35
10	9.48	7.62		0.8	1.35
11	10	8.17		0.8	1.35
12	10.44	8.68		0.8	1.35
13	10.77	9.13		0.8	1.35
14	11.39	9.69		0.8	1.35
15	12.03	10.25		0.8	1.35
16	12.65	10.82	3.35	0.8	1.35
17	13.17	11.28		0.8	1.35
18	13.57	11.6		0.8	1.35
19	13.98	12.13		0.8	1.35
20	14.48	12.35		0.8	1.35
21	14.56	12.34		0.8	1.35
22	14.56	12.31		0.8	1.35
23	14.58	12.52		0.8	1.35
24	14.66	12.79		0.8	1.35
25	14.75	13.04		0.8	1.35
26	15.13	13.68		0.8	1.35
27	15.64	14.1		0.8	1.35
28	15.81	14.24		0.8	1.35
29	16	14.29		0.8	1.35
30	16.42	14.77		0.8	1.35
31	17.13	15.63		0.8	1.35

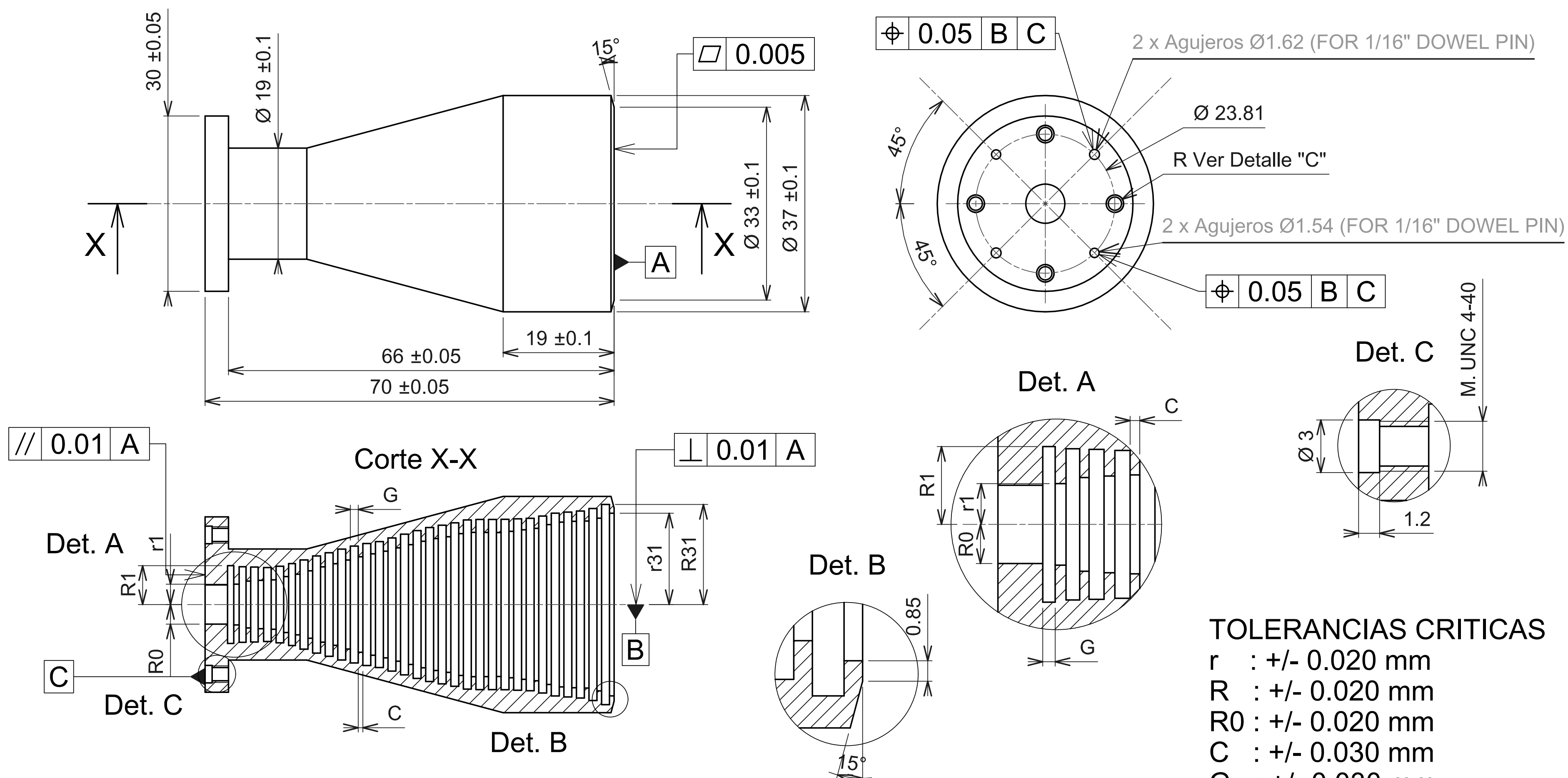

TOLERANCIAS CRITICAS

r : +/- 0.020 mm
R : +/- 0.020 mm
R0 : +/- 0.020 mm
C : +/- 0.030 mm
G : +/- 0.030 mm

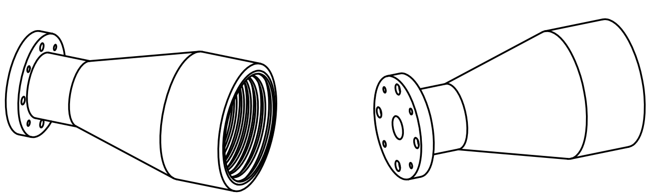

	NAME	DATE	
DESING	V.TAPIA	24/11/2014	fcfm Astronomía, Facultad de Ciencias Físicas y Matemáticas, Universidad de Chile — Cerro Calán Observatorio Astronómico Nacional
DRAWN	J.PIZARRO	25/11/2014	TITLE BANDA 1
REVISED	---	---	
	Material Duraluminio		DWG N° Horn
			SCALE 1:1 — SHEET 1 OF 1

Appendix C

Lens v1, technical drawing

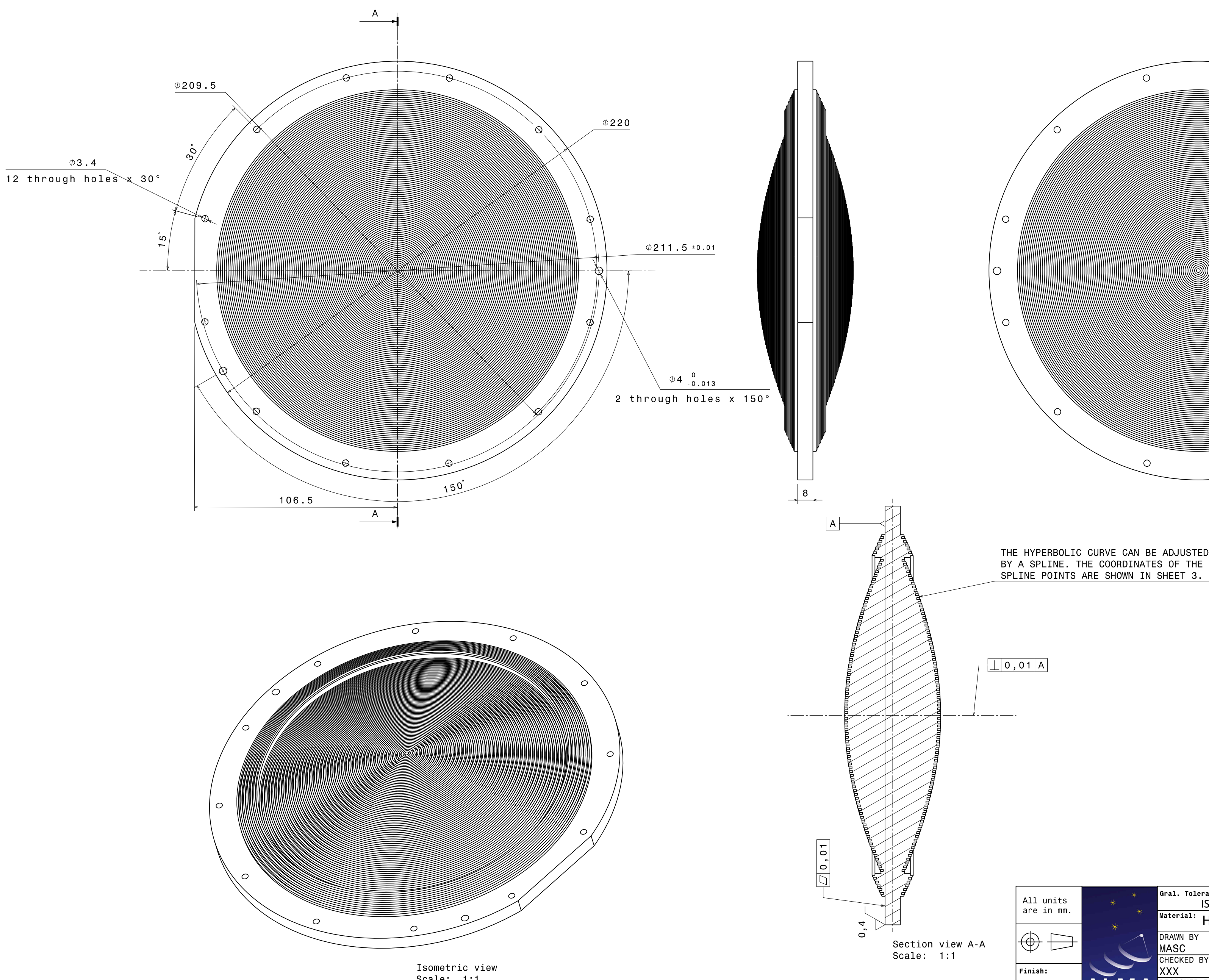

All units are in mm.	Gral. Tolerances: ISO 2768-fH		
	Material: HDPE		
	DRAWN BY MASC	DATE 17/12/2013	DRAWING TITLE BAND 1 LENS
	CHECKED BY XXX	DATE XXX	SIZE A1 / DRAWING NUMBER 40.01.01.01-010 / REV 1.0
Finish: CLEAN/REMOVE ALL BURRS	DESIGNED BY XXX	DATE XXX	SCALE 1:1 / WEIGHT(kg) 0.76 / SHEET 1/3

ALMA

Cerro Calán
Observatorio Astronómico Nacional

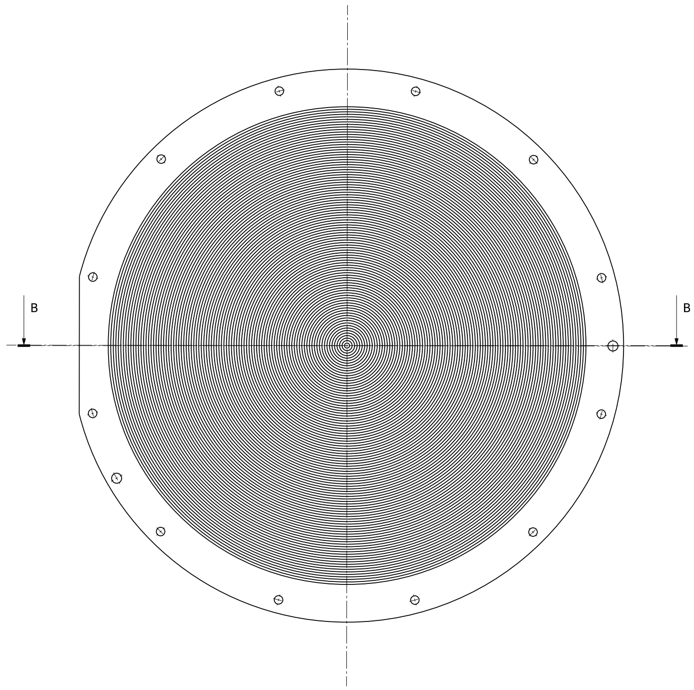

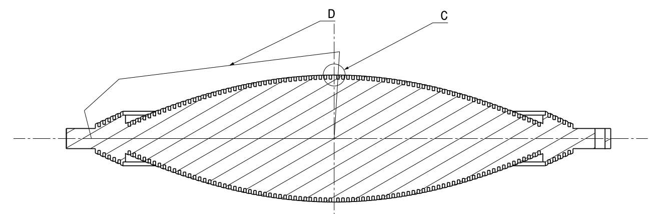

Section view B-B
Scale: 1:1

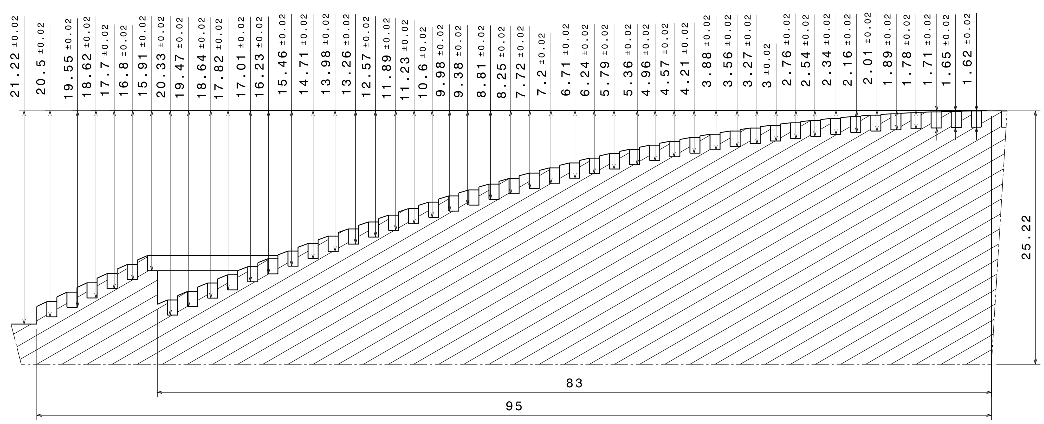

Detail D
Scale: 4:1

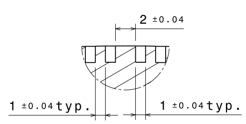

Detail C
Scale: 4:1

All units are in mm.	Gral. Tolerances: ISO 2768-fH		Cerro Calán Observatorio Astronómico Nacional	
	Material: HDPE		DRAWING TITLE: BAND 1 LENS	
	DRAWN BY: MASC	DATE: 17/12/2013	SIZE: A1	DRAWING NUMBER: 40.01.01.01-010	REV: 1.0
Finish: CLEAN/REMOVE ALL BURRS	CHECKED BY: XXX	DATE: XXX	SCALE: 1:1	WEIGHT(kg): 0.76	SHEET: 2/3
ALMA	DESIGNED BY: XXX	DATE: XXX			

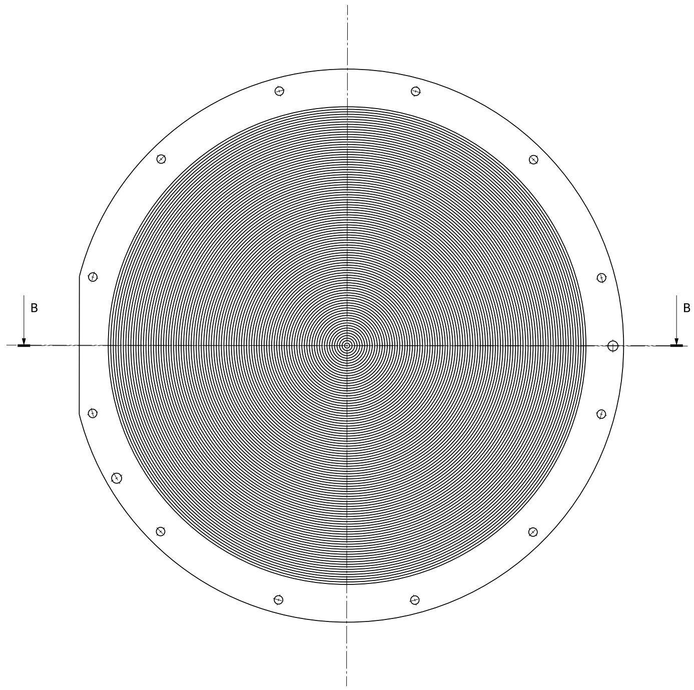

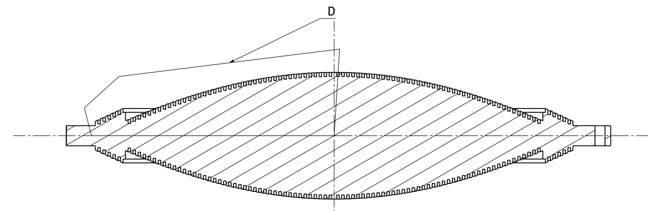

Section view B-B
Scale: 1:1

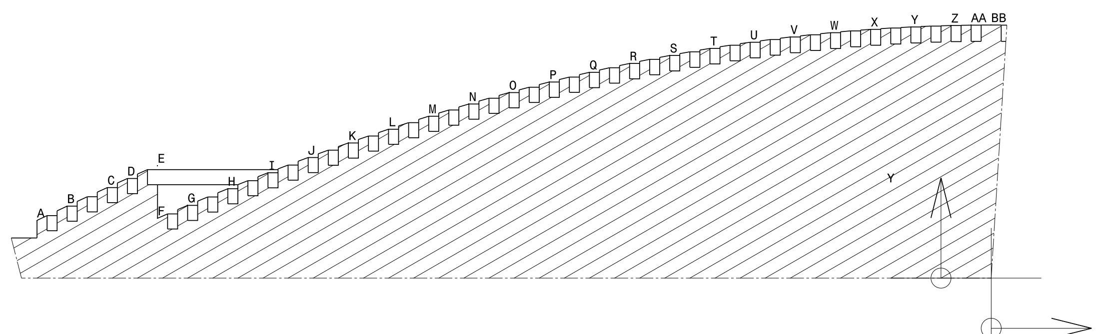

Detail D
Scale: 4:1

Spline Point Coordinates		
REF.	X	Y
A	-95	5,75
B	-92	7,18
C	-88	9,03
D	-86	9,93
E	-83	11,21
F	-83	5,97
G	-80	7,25
H	-76	8,91
I	-72	10,5
J	-68	12,02
K	-64	13,47
L	-60	14,84
M	-56	16,14
N	-52	17,35
O	-48	18,49
P	-44	19,54
Q	-40	20,51
R	-36	21,4
S	-32	22,19
T	-28	22,89
U	-24	23,51
V	-20	24,03
W	-16	24,46
X	-12	24,79
Y	-8	25,03
Z	-4	25,18
AA	-2	25,21
BB	0	25,22

All units are in mm.

Finish: CLEAN/REMOVE ALL BURRS

ALMA

Gral. Tolerances: ISO 2768-fH

Material: HDPE

DRAWN BY	DATE
MASC	17/12/2013
CHECKED BY XXX	DATE XXX
DESIGNED BY XXX	DATE XXX

fcfm

Cerro Calán
Observatorio Astronómico Nacional

DRAWING TITLE
BAND 1 LENS

SIZE	DRAWING NUMBER	REV
A1	40.01.01.01-010	1.0

SCALE 1:1 | WEIGHT(kg) 0.76 | SHEET 3/3

Appendix D

Lens v2, technical drawing

REV	DATE	DESCRIPTION	INIT
2.0	21-08-2014	MODIFICATION OF THE HYPERBOLA	MASC

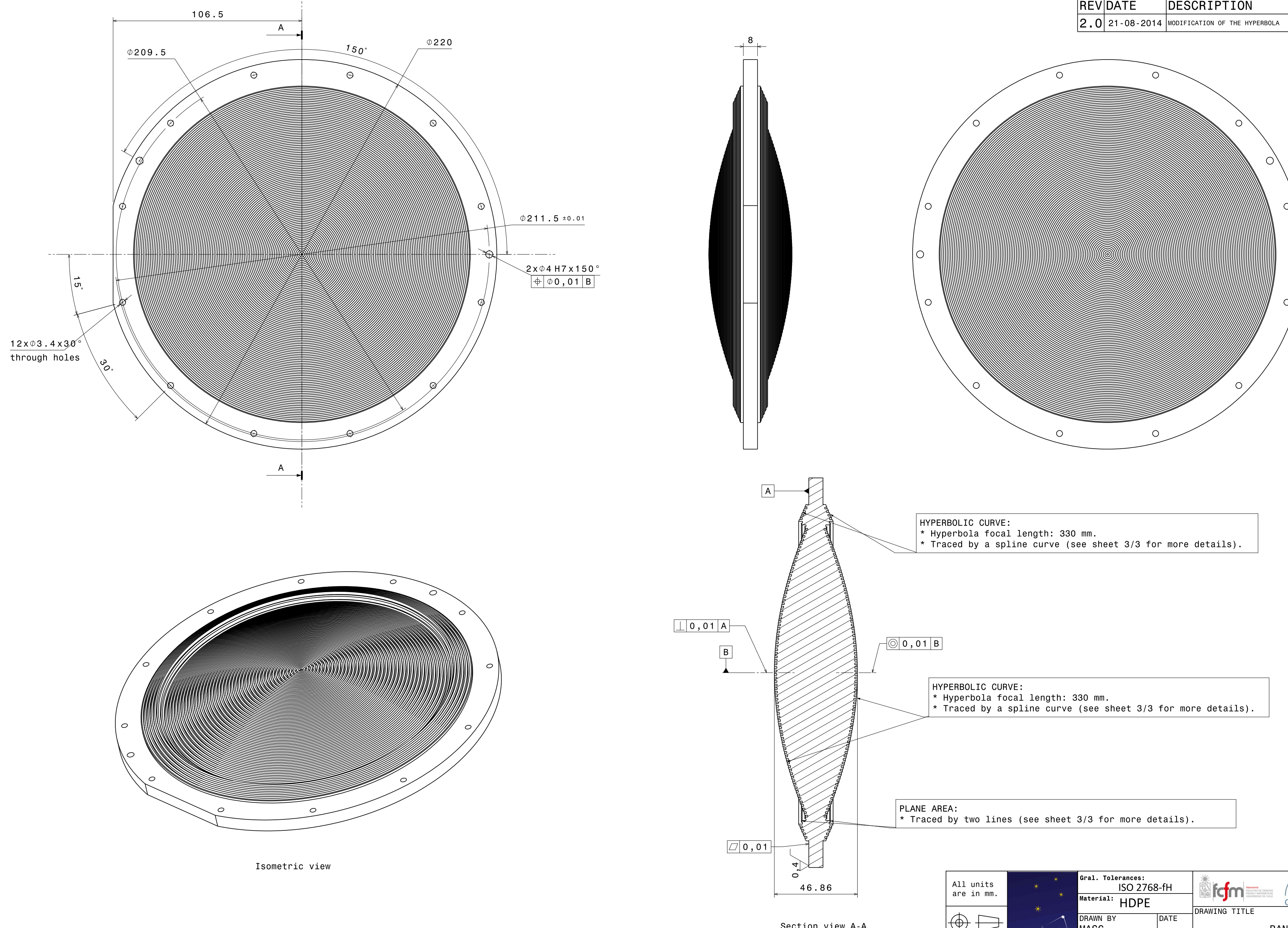

All units are in mm.	Gral. Tolerances: ISO 2768-fH		Cerro Calán Observatorio Astronómico Nacional
	Material: HDPE		DRAWING TITLE: BAND 1 LENS
	DRAWN BY: MASC	DATE: 21-08-2014	SIZE: A1 — DRAWING NUMBER: 40.01.01.01-010-v2 — REV: 2.0
Finish: CLEAN/REMOVE ALL BURRS	CHECKED BY: JP	DATE: xxx	SCALE: 1:1 — WEIGHT(kg): 0,72 — SHEET: 1/3
ALMA	DESIGNED BY: VT	DATE: 20-08-2014	

REV	DATE	DESCRIPTION	INIT
2.0	21-08-2014	MODIFICATION OF THE HYPERBOLA	MASC

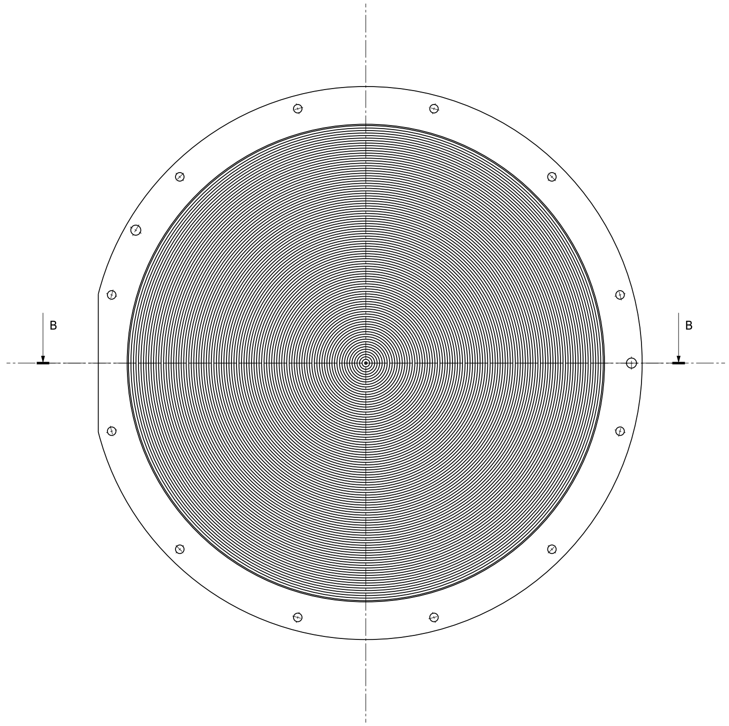

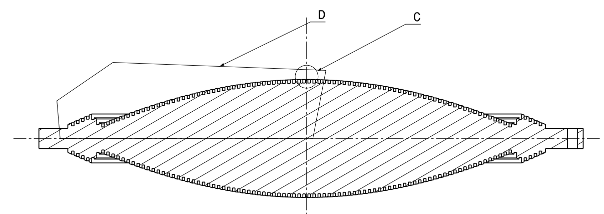

Section view B-B
Scale: 1:1

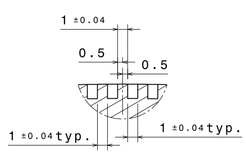

Detail C
Scale: 4:1

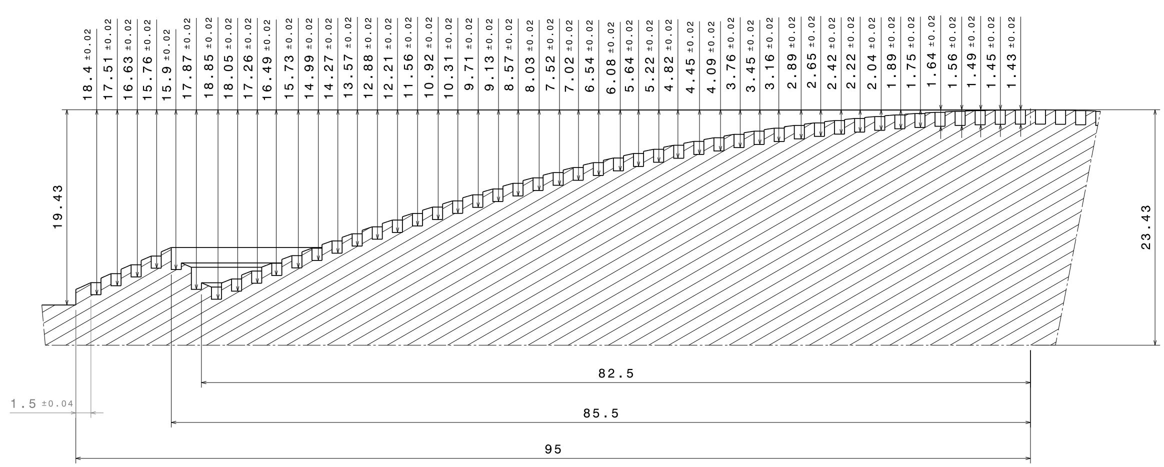

Detail D
Scale: 4:1

All units are in mm.	Gral. Tolerances: ISO 2768-fH	Cerro Calán Observatorio Astronómico Nacional	
Finish: CLEAN/REMOVE ALL BURRS	Material: HDPE	DRAWING TITLE BAND 1 LENS	
ALMA	DRAWN BY MASC	DATE 21-08-2014	
	CHECKED BY JP	DATE XXX	
	DESIGNED BY VT	DATE 20-08-2014	

SIZE	DRAWING NUMBER	REV
A1	40.01.01.01-010-v2	2.0

SCALE	1:1	WEIGHT(kg)	0,72	SHEET	2/3

REV	DATE	DESCRIPTION	INIT
2.0	21-08-2014	MODIFICATION OF THE HYPERBOLA	MASC

Spline Point Coordinates		
REF.	X	Y
A	-95	5,55
B	-92,5	6,67
C	-90,5	7,56
D	-88,5	8,44
E	-85,5	9,72
F	-84,5	8,19
G	-83,5	7,75
H	-82,5	6,22
I	-81,5	5,78
J	-80,5	6,19
K	-78,5	6,99
L	-76,5	7,77
M	-74,5	8,54
N	-72,5	9,29
O	-70,5	10,02
P	-68,5	10,74
Q	-66,5	11,44
R	-64,5	12,12
S	-62,5	12,78
T	-60,5	13,43
U	-58,5	14,06
V	-56,5	14,67
W	-54,5	15,26
X	-52,5	15,83
Y	-50,5	16,38
Z	-48,5	16,92
AA	-46,5	17,43
BB	-44,5	17,93
CC	-42,5	18,4
DD	-40,5	18,86
EE	-38,5	19,29
FF	-36,5	19,7
GG	-34,5	20,09
HH	-32,5	20,47
II	-30,5	20,82
JJ	-28,5	21,14
KK	-26,5	21,45
LL	-24,5	21,74
MM	-22,5	22
NN	-20,5	22,24
OO	-18,5	22,46
PP	-16,5	22,66
QQ	-14,5	22,83
RR	-12,5	22,99
SS	-10,5	23,12
TT	-8,5	23,22
UU	-6,5	23,31
VV	-4,5	23,37
WW	-2,5	23,41
XX	-0,5	23,43
YY	0	23,43

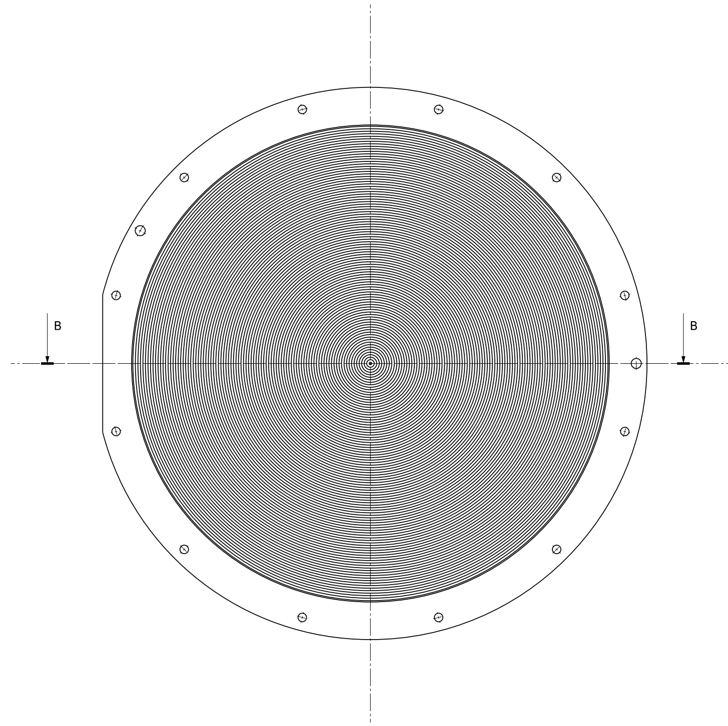

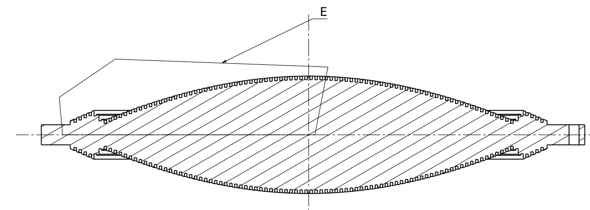

Section view B-B
Scale: 1:1

NOTE:
* The line between the points F-G and HI are not a spline,
they are two straight lines.

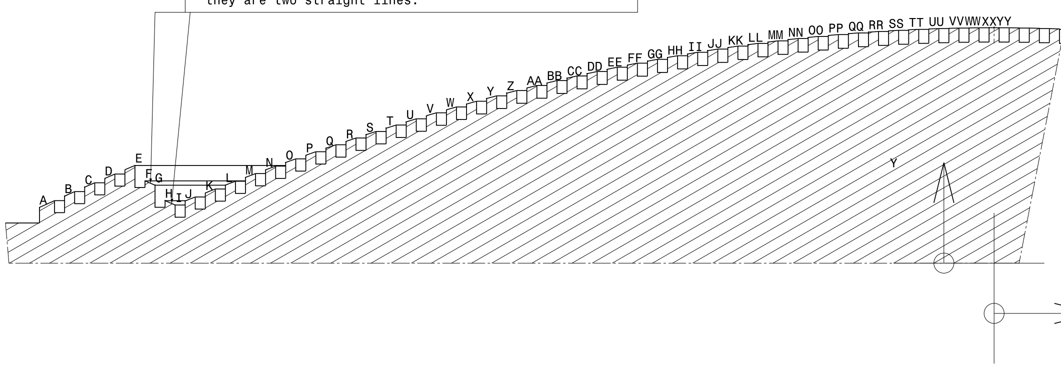

Detail E

All units are in mm.

X

Finish:
CLEAN/REMOVE ALL BURRS

ALMA

Gral. Tolerances: ISO 2768-fH
Material: HDPE

DRAWN BY	DATE
MASC	21-08-2014
CHECKED BY	DATE
JP	xxx
DESIGNED BY	DATE
VT	20-08-2014

fcfm

Cerro Calán
Observatorio Astronómico Nacional

DRAWING TITLE
BAND 1 LENS

SIZE	DRAWING NUMBER	REV
A1	40.01.01.01-010-v2	2.0

SCALE 1:1 | WEIGHT(kg) 0,72 | SHEET 3/3

Appendix E

Lens v3, technical drawing

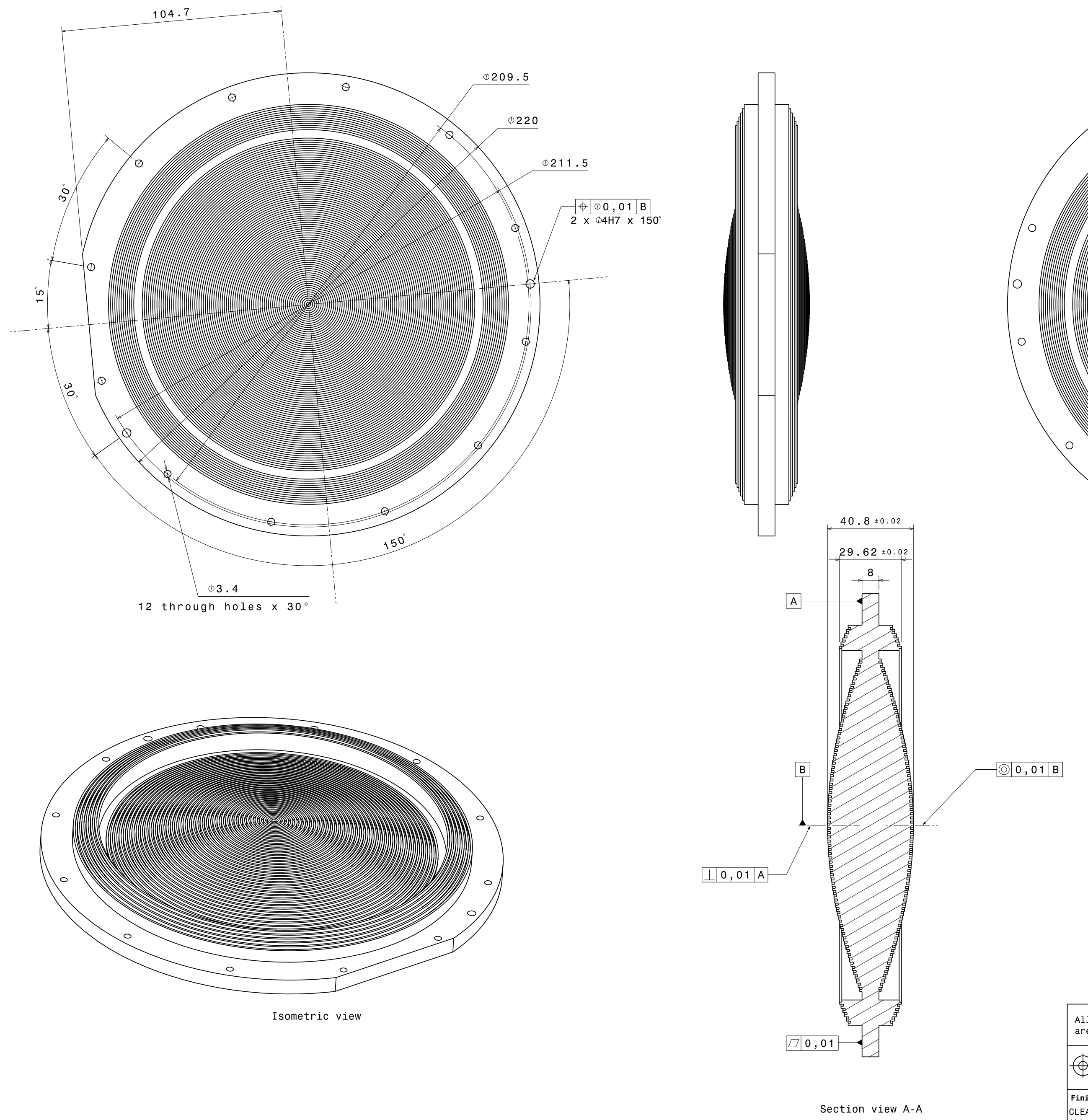

All units are in mm.	Gral. Tolerances: ISO 2768-fH		Cerro Calán Observatorio Astronómico Nacional	
Finish: CLEAN/REMOVE ALL BURRS	Material: HDPE		DRAWING TITLE BAND 1 LENS	
	DRAWN BY MASC	DATE 16/12/2014	SIZE A1	DRAWING NUMBER 40.01.01.01-010
	CHECKED BY JP	DATE 17/12/2014	REV 3.0	
	DESIGNED BY VT/AG	DATE 12/12/2014	SCALE 1:1	WEIGHT(kg) 0.683
			SHEET 1/2	

ALMA

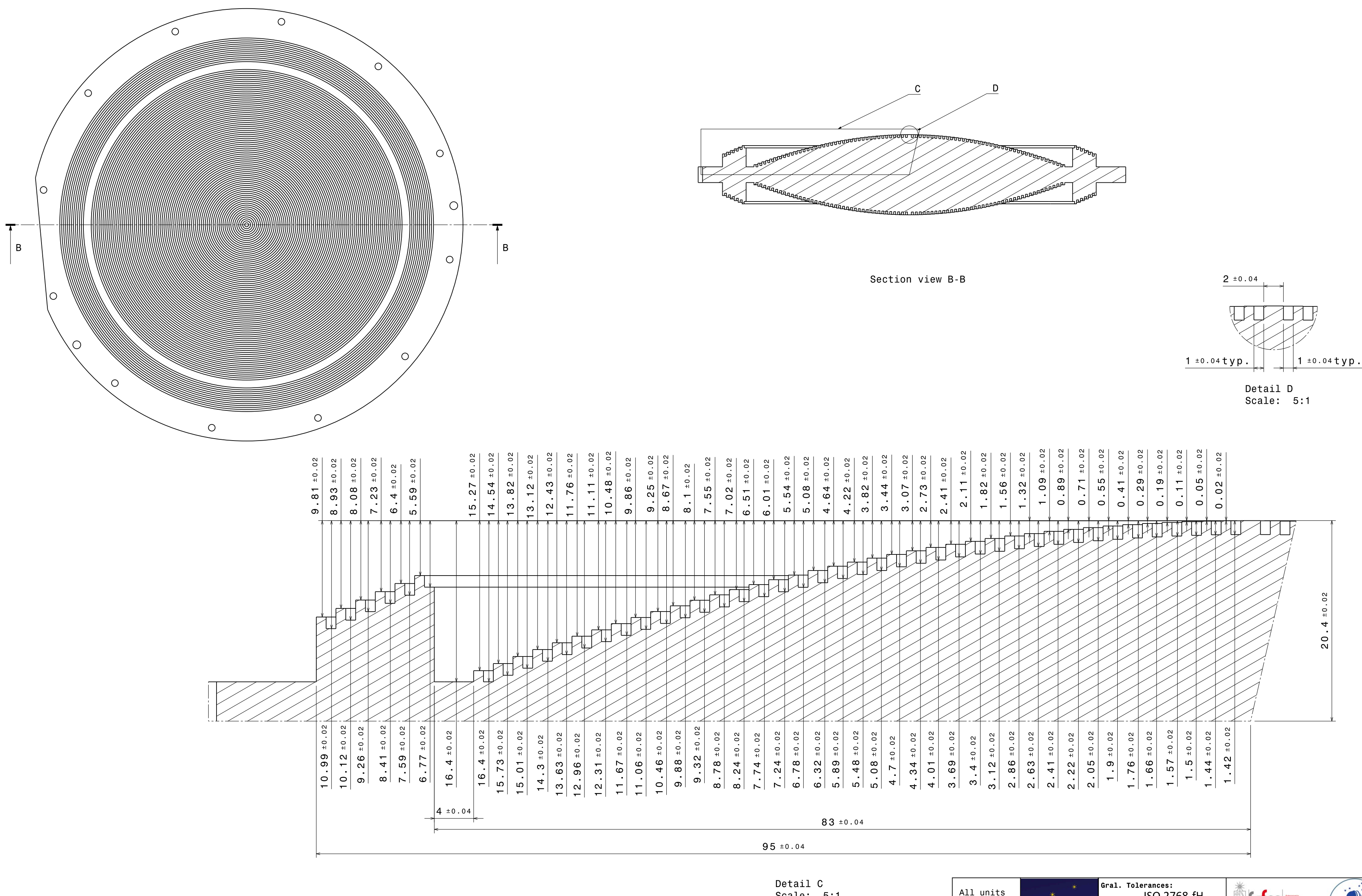

All units are in mm.	Gral. Tolerances: ISO 2768-fH		Cerro Calán – Observatorio Astronómico Nacional	
	Material: HDPE		DRAWING TITLE: BAND 1 LENS	
Finish: CLEAN/REMOVE ALL BURRS	DRAWN BY: MASC	DATE: 16/12/2014	SIZE: A1	DRAWING NUMBER: 40.01.01.01-010
ALMA	CHECKED BY: JP	DATE: 17/12/2014	REV: 3.0	
	DESIGNED BY: VT/AG	DATE: 12/12/2014	SCALE: 1:1	WEIGHT(kg) 0.683
			SHEET: 2/2	

Appendix F

Design of the optical system for ALMA Band 1

Design of the optical system for ALMA Band 1

Nicolás Reyes[a,b,*], Valeria Tapia[a], Doug Henke[c], Miguel Sanchez-Carrasco[a,d], F. Patricio Mena[a], Stéphane M. X. Claude[c], Leonardo Bronfman[e].

[a]Departament of Electrical Engineering, Universidad de Chile, Santiago, Chile
[b] Max-Planck-Institut für Radioastronomie, Bonn ,Germany
[c] NRC - Herzburg Institute of Astrophysics, Ottawa, Canada
[d] Instituto de Astrofísica de Andalucía, Andalucía, España
[e] Astronomy Departament, Universidad de Chile, Santiago, Chile
[*]Contact: nireyes@u.uchile.cl, phone: +56-2-9787119

ABSTRACT

This work presents a complete study of the optical system for ALMA band 1, which covers the frequency range from 35 to 50 GHz, with the goal of extending the coverage up to 52GHz. Several options have been explored to comply with the stringent technical specifications, restrictions, and cost constraints. The best solution consists of a corrugated zoned lens, two infrared filters and a spline profiled corrugated horn. The calculated aperture efficiency is better than 75%, while the average noise contribution is lower than 10.3 K. The first prototypes of the system have been constructed and first evaluation results available

Keywords: ALMA, band 1, optics, spline-profile horn, lens, noise temperature, efficiency.

1. INTRODUCTION

The Atacama Large Millimeter Array (ALMA) is the largest millimeter and submillimeter radio telescope in the world. It consists of 66 classical Cassegrain antennas with diameters of 7 and 12 m, divided in two subarrays. It has been constructed in Chile's Atacama Desert at an altitude of 5000 m above sea level. ALMA is providing unprecedented sensitivity and resolution for the study of the origins of the universe; formation of stars, planets and galaxies; and the complex chemistry of the giant clouds of gas and dust [1]. This radio observatory has an operation frequency range between 35–950 GHz divided into 10 bands. Each band has a set of dual linear polarization receivers, one per antenna, that convert the input microwave signals into intermediate frequencies from 4 to 12 GHz. The output signals are then postprocessed to obtain high resolution images using radio interferometric techniques. The quality of the images depends strongly on the noise introduced by the receivers.

In order to minimize this noise, each subsystem has to be optimized, in particular those at the beginning of the chain. Since the receivers' optics are first in the receiver chain of each antenna, achieving good noise temperature and aperture efficiency are fundamental for best sensitivity [2].This paper presents the design and preliminary results of the optical system for the Band 1 receivers of ALMA.

Band 1's optical system combines a series of stringent technical specifications, construction limitationsand cost constraints that require trade-offs with each other. Important specifications are the following. The optical system must cover the frequency range between 35–50 GHz (with the goal of extending the coverage to 35–52 GHz), meet a total aperture efficiency that exceeds 80%, attain an angular alignment of the optical beam within 5 mrad of the nominal direction, and the added noise due to the optics should be close to 10K. The illumination must be frequency independent, thus no mechanical tuning is allowed. If warm optics is present, it cannot interfere with the already-existing common optics of the other bands, the amplitude calibration deviceand Water Vapour Radiometer. Furthermore, the 7 and 12-m antennas use the same front end which leads to different beam tilt angles.

We have performed a comparative study of different alternatives for the ALMA Band 1 optical system using the following approach. First, we studied several optical systems using mode matching and quasioptical techniques. Then, we chose the configuration that achieved the best results and further optimized its components for final manufacturing. Finally, the full system was validated using the finite-element methodandmethod of moments. The proposed solution is currently the baseline design for the final Band 1 production.

Ground-based and Airborne Telescopes V, edited by Larry M. Stepp, Roberto Gilmozzi,
Helen J. Hall, Proc. of SPIE Vol. 9145, 91451W • © 2014 SPIE
CCC code: 0277-786X/14/$18 • doi: 10.1117/12.2055170

2. OPTICAL DESIGN

Several configurations were explored for the focusing elements and feed horn. We have studied optical systems composed of one warm lens with a separate vacuum window, a single warm lens (acting also as a window), two warm mirrors plus a window, and two lenses (with one cooled lens). Furthermore, we have studied different shapes and materials for the lens. The best performance was obtained for a system consisting of the following elements. A low loss High Density Polyethylene (HDPE)biconvex one-zone Fresnel lens; a thin gore-tex membrane and a grooved surface of Polytetrafluoroethylene (PTFE) as infrared filters at the 15 and 110 K stages; and a compact spline-profile corrugated horn that can be machined from a single block.

2.1 Feed horn design

If a standard corrugated feed horn is used, the resulting narrow flare angle of the horn make it difficult to machine as a single piece; however, the horn may be divided into smaller sections and machined on a lathe as in [3]. In order to shorten the overall length of the feed horn, we propose to use a spline profiled corrugated horn. Therefore, we propose to use a spline profiled corrugated horn. The profile was optimized for achieving the desired performance while constraining it for fabrication as a single piece on a computer-numerical-control (CNC) lathe.

To achieve frequency independent illumination while minimizing truncation through the cryostat's window, a maximum beamwaist of 9.6 mm is required. The characteristics of an ideal Gaussian feed were determined by optimizing a quasioptical model of the Band 1 optics. The profiled horn was then optimized to match the Gaussian feed and achieve low cross-polarization and reflected power. The profile was optimized using a mode-matching software, Microwave Wizard from MICIAN, and a genetic algorithm using the goals shown in Table 1. The main parameters of the resulting horn are shown in Table 2, where only the input waveguide radius was not an optimization parameter. The geometry of the spline-profile corrugated horn is shown in Table 2 and Figure 1.

Table 1: Optimization goals of the profiled feed horn

Frequency [GHz]	**33**	**35**	**38**	**42**	**42.5**	**44**	**47**	**50**	**52**
10 dB point [deg]	19.1	18	16.6	15.4	14.8	14.3	13.4	12.6	12.1
PCL[mm]	5	5.6	6.4	7.7	8.2	10.1	11.2	11.2	12
Crosspolar level [dB]	<-30	<-37							<-30
Reflected power [mm]	<-25	<-30							<-25
Δ 10 dB point [deg]*	<1	<0.3							<1
Δ PCL [mm]*	<2	<1							<2
(*)The difference between the E and H planes									

Table 2: Geometry of the spline-profile corrugated horn

Horn design parameter	Value
Input circular radius (R0)	3.35 mm
Aperture diameter (r31)	31.62 mm
Horn total length	70 mm
Number of corrugations	31
Width of corrugation (C)	0.9
Width of gap (G)	1.22
Depth of gap (Ri – ri)	2.97-1.53 mm

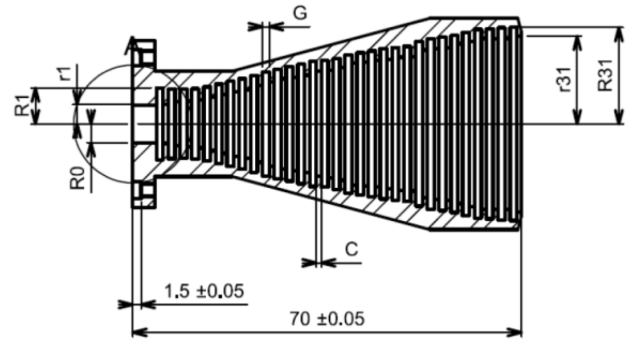

Figure 1: Geometry of the spline-profile corrugated horn

2.2 Design of refocusing elements

2.2.1 Analysis of the different possible options

Single Cold Lens

In order to reduce the noise this was the first option to be studied. A quasioptical analysis shows that to achieve the desired illumination at the subreflector, the refocusing element has to be located above the cryostat top plate. In other words, if the lens is forced to be inside of the cryostat, the beam size at the cryostat aperture exceeds by far the size of the cryostat's window.

Single Warm Lens

In order to optimize the subreflector's illumination with a single warm lens, a quasioptical propagation script was written. The inputs for this script are the beam waist size and position at the horn, while the optimization parameters are the lens position, the focal distance, and the beam radius. It was found that the best results are obtained with a lens located at a distance of 175.2 mm from the horn aperture and a focal length of 172.1 mm. In addition, if we choose an appropriate material, the lens has the advantage of being able to be used as a vacuum window.

Warm and Cold Lenses

A combination of cold and warm lenses was also evaluated. The cold lens was used to obtain a narrower beam to pass the cryostat rim, minimizing the truncation. Accordingly, a warm lens outside of the cryostat was required to obtain the right edge taper on the secondary. The disadvantage of this solution is that the warm lens would still needs to be large, resulting in the same or more signal loss than only a warm lens [3], [4].

Warm Mirrors

The last configuration to be studied was the use of warm mirrors. This configuration has the advantage of producing lower noise contribution than the use of a lens. Moreover, they do not require anti-reflection layers and do not suffer from variations in batch-to-batch material properties, as it is the case for dielectrics. Nevertheless, warm mirrors will require a separate vacuum window, which will need anti-reflection layers. A configuration formed by a standard horn and two warm mirrors was analyzed with a mode matching model. However, it was found that the mirrors would interfere with the robotic arm of the calibration device.

2.2.2 Warm-lens analysis and further optimization

Given the considerations presented above, the warm lens configuration was selected to be further optimized in order to maximize the aperture efficiency and minimize the noise temperature. An important task has been to study the material for the lens design since it will impact the lens thickness and loss. Therefore, a low tangent loss and high dielectric constant are desirable. Furthermore, the lens and the antireflection layer should be easily manufactured. Materials with a high dielectric constant, such as quartz, fused silica and sapphire, require complex antireflection treatment, for instance adding appropriate antireflection layers [5]. Alternatively, a lens and its antireflection layer can be manufactured using plastic materials, such as HDPE and PTFE, through direct CNC machining or injection molds. Since the lens also works as vacuum window, HDPE was chosen over PTFE because it exhibits less creep deformation.

The lens thickness can be reduced using a zoned lens with only one step. By implementing such design, the noise of the optics system can be lowered between 1 and 2 K. Despite the reduction in noise, it can be observed that the use of a zoned lens produces a reduction in efficiency of 0.5% at the lower frequency range.

2.3 Final validation

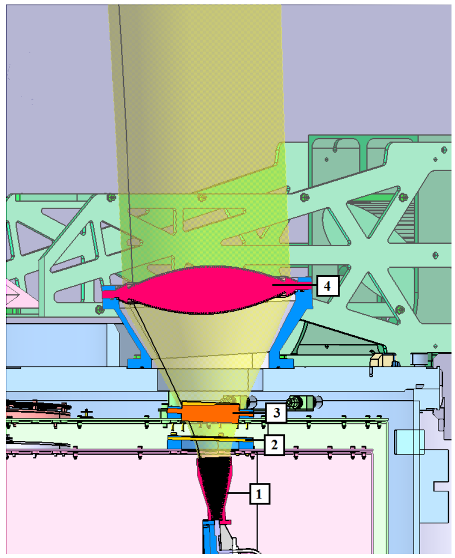

Figure 2: Cross-section of the baseline solution for the Band 1 optics. (1) Spline-profile Feed horn, (2)Gore-tex infrared filter at 15 K, (3) PTFE infrared filter at 110 K, and (4) Biconvex one-zone lens

The full optical system, as shown in Figure 2, was simulated. First, the horn and IR filters were simulated using HFSS, an electromagnetic solver based on the finite-element method. Reflection loss and higher mode orders were studied with a resolution of 50 MHz. The output radiated field was calculated over a near-field sphere with a radius of 175.2 mm, equal to the horn-lens distance. Then, using HFSS-IE (a full-wave integral equation solver), the near-field of the horn and IR filters was used to excite the lens. The resulting output field is then used to calculate the aperture efficiency (including phase, amplitude, cross-polarization, and spill-over efficiencies) assuming an equivalent paraboloid with a diameter equivalent to the secondary diameter and focus equivalent to the resulting telescope focus.

The noise temperature was computed conservativelyconsidering the contribution of each single components, lens, 110 K and 15 K IR filters, as well as truncation in all apertures, including the vertex hole and subreflector spill-over. For the lens and IR filters, the added noise was calculated considering the dielectric losses, truncation and reflections [5]. To estimate truncation losses, multi-mode mode matching simulations were used [5][6]. The reflected power is terminated at a physical temperature equal to the average between the element under analysis and the previous element while inside the cryostat. Truncated power at the vertex hole was terminated at 300 K, while the subreflector spill-over was terminated at 3 K.

2.4 Experiment

In order to characterize the optical system, it has been tested using a vertical planar near-field beam-pattern scanner inside an anechoic chamber [7]. The probe antenna was set in Fresnel zone, and swept an opening equivalent to 40° measuring the near-field co- and cross-polarization patterns.

The near-field was transformed to far-field using a Fast Fourier Transform algorithm [8] and compared with simulation. At the moment of writing, only the horn and 15 K IR filter have been characterized. Final efficiencies and noise temperature results will be confirmed once measurements are completed.

3. RESULTS

3.1 Simulations

3.1.1 Horn

The simulated radiation patterns for the spline-profile corrugated horn at 35, 42.5 and 50 GHz are shown inFigure 3. The patterns exhibit good symmetry down to -20 dB, a cross-polarization level better than -34 dB and side lobes lower than -20 dB. Moreover, the return loss of the horn is lower than -28 dB as shown in Figure 4.

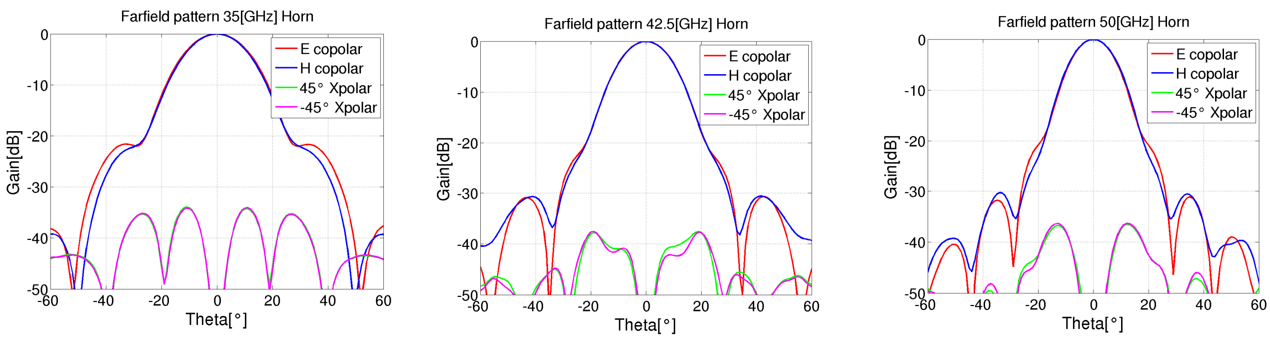

Figure 3: HFSS simulated radiation patterns of the spline-profile corrugated horn at 35, 42.5 and 50 GHz

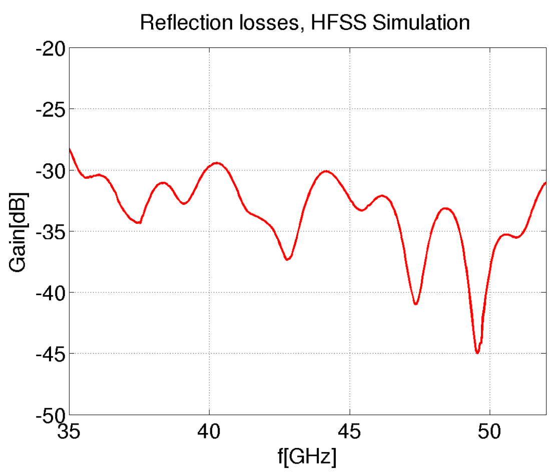

Figure 4: Simulated return loss of the spline-profile corrugated horn

3.1.2 Simulation of the Horn, IR Filters, and Lens Combination

The simulated radiation patterns for the complete optical system at 35, 42.5 and 50 GHz are shown in Figure 5. The patterns exhibit good symmetry to -20 dB, a cross-polarization level better than -22 dB and side lobes lower than -20 dB.

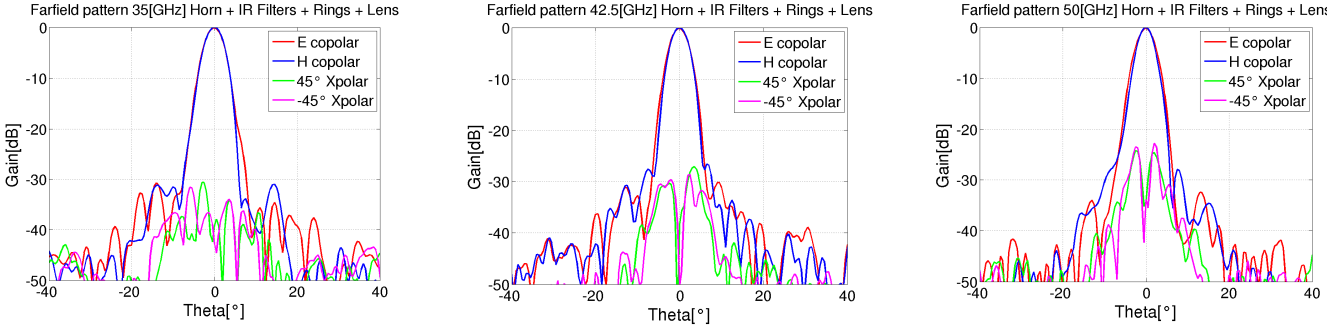

Figure 5: HFSS simulated radiation patterns of the complete optical system at 35, 42.5 and 50 GHz

The aperture efficiency and its components are shown inFigure 6.a. The aperture efficiency for the complete system is between 75% and 79.2%, where the cross-polarization and phase efficiencies are better than 99.5%, the amplitude efficiency is more than 90% and the spillover efficiency is less than 80%. We also compare the efficiencies for the full system and the system without IR filters to show the degradation due to the IR filters. The total noise temperature and the contribution of each single element is shown inFigure 6.b. The total noise is between 9.4 and 11.6 K, where the lens contributes the most to the noise.

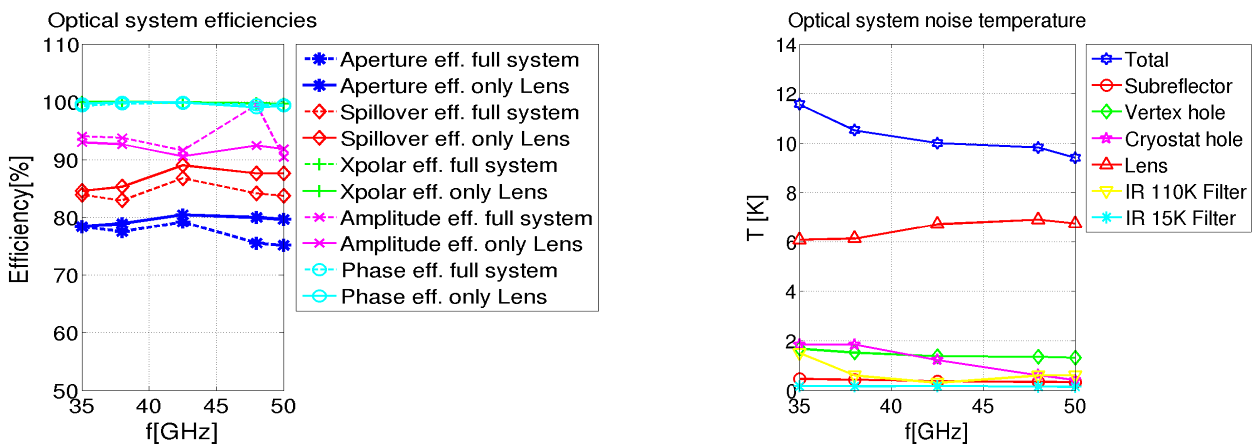

Figure 6: a) HFSS simulated aperture efficiency comparison between the full system (horn, IR filters, and lens)and only horn + Lens from 35 to 50 GHz. b) Noise temperature contribution of each single component from 35 to 50 GHz.

3.2 Measurement results

3.2.1 Horn

The far-field radiation patterns are shown inFigure 7. The copolar measurements are identical to simulation down to -20 dB at all frequencies. The cross-polarization has a maximum difference of 3 dB between the maxima of simulated and measured at 35 GHz.

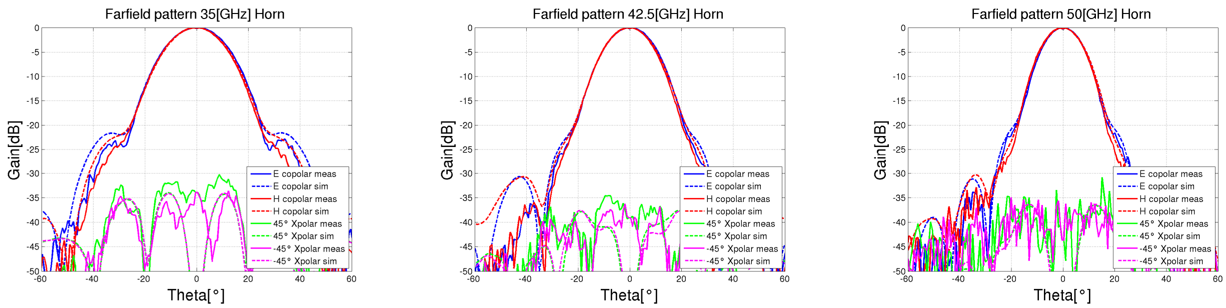

Figure 7: Comparison between simulated and measured radiation patterns of the spline-profile corrugated horn at 35, 42.5 and 50 GHz. Dotted lines correspond to simulation results and straight lines correspond to measurement results.

3.2.2 Measurement of the Horn, 15-K Ring, and 15-K IR Filter Combination

The far-field radiation patterns are shown inFigure 8. The copolar measurements compare well to simulation down to -20 dB across frequency, with maximum differences of 2.5°. The largest difference between the maxima of simulated and measured cross-polarizationis 4 dB.

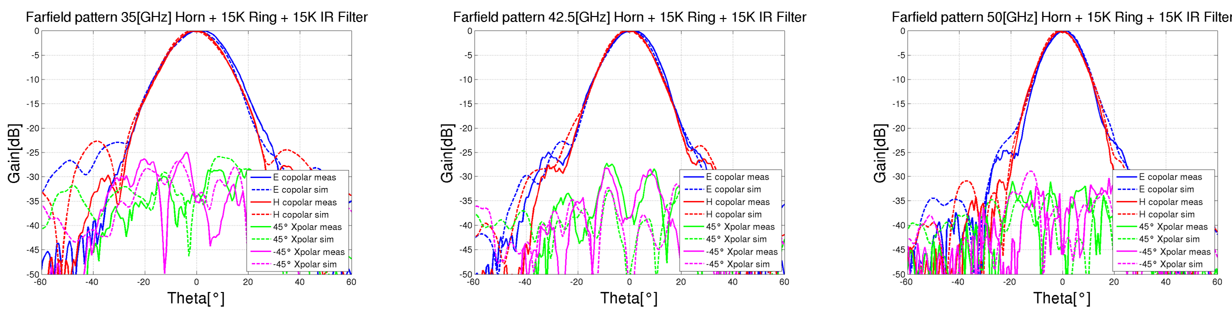

Figure 8: Comparison between HFSS simulated and measured radiation patterns of the horn + IR 15 K filter at 35, 42.5 and 50 GHz.

4. CONCLUSION AND FUTURE WORK

We have presented a complete design of the optical system for ALMA Band 1 that covers the frequency range from 35-50 GHz. The optical system is frequency independent and consists of the following elements. A compact spline-profile corrugated horn, machined from a single block of *duralumin;* a thin *gore-tex* membrane and a grooved surface of *PTFE* as an infrared filter at the 15 and 110-K stages; and a low loss HDPE biconvex one-zone Fresnel lens.Moreover,the warm optics donot interfere with the already-existing common optics or calibration device.

The simulated aperture efficiencies are greater than 75%, slightly lower than the expected, due to truncation and dielectric loss introduced by the filters. It is necessary to mention that the filters have already been constructed and installed in the cryostats. The noise temperature was estimated conservatively, sothe maximum average noise temperature should be less than 10.3 K.

We have successfully constructed a spline-profile corrugated horn. Moreover, the simulation and measurements of radiation patterns agree very well with the HFSS simulations. Final efficiencies and noise temperature results will be confirmed once measurements are completed.

The Band 1 optics design presented throughout this paper is a baseline design. Accordingly, future work may include the effects of the IR filters in the new design in order to improve the efficiency. The first option is to optimize the horn antenna including the degradation of the IR filters. A second option is to optimize the lens to achieve an edge taper nearer to -12.3 dB. The last option is to redesign the IR filter minimizing the truncations.

REFERENCES

[1] A. Wootten Ed., "Science With the Atacama Large Millimeter Array,"ASP confProc, vol. 253 (2001).

[2] James W. Lamb, "Low-noise, high-efficiency optics design for ALMA receivers," Antennas and Propagation, IEEE Transactions on, vol. 51, no. 8, 2035-2047(2003).

[3] S. Claude et al, "ALMA Band 1 Component Down-selection – HIA NRC Report," NRC Herzberg, Victoria, BC (2013).

[4] P. Zorzi et al., "Revisiting the ALMA Band 1 Optics Design," Proc. 21st Int. Symp. Space THz Tech, 348-352 (2010).

[5] P.F. Goldsmith, Quasioptical Systems: Gaussian Beam Quasioptical Propagation and Applications, IEEE Press, New York,(1998).

[6] Sugimoto M.,"Sensitivity Analysis of Optical Systems in Radio Telescopes", Proc Astronomical Society of Japan 62, 39-50 (2010).

[7] P. Zorzi, "Construction and Measurement of a 31.3-45 GHz Optimized Spline-profile Horn and Corrugations," Journal of Infrared Millimeter and Terahertz Waves, vol. 33, 17-24 (2011).

[8] D. Janse van Rensbur, "Millimeter Wave Near-Field Antenna Testing," Nearfield systems Inc. Microwave Product Digest Article (2010).

Bibliography

[1] A. website, “The atmosphere above llano de chajnantor,” Accessed January 2015.

[2] A. Otárola, M. Holdaway, L.-A. Nyman, S. Radford, and B. B. J., “Atmospheric transparency at chajnantor: 1973-2003, alma memo 512,” *ALMA MEMO # 512*, 2005.

[3] D. M. Pozar, *Microwave Engineering.* New York, New York: Wiley, 4 edition, 2011.

[4] S. A. Maas, *Microwave Mixers.* Artech House, 1986.

[5] T. Wilson, K. Rohlfs, and S. Hüttemeister, *Tools of Radio Astronomy.* Astronomy and Asnstitution of Electrical Engineerstrophysics Library, Springer, 2009.

[6] J. W. Kooi, *Advanced receivers for submillimeter and far infrared astronomy.* PhD thesis, Groningen: University Library Groningen, 2008.

[7] J. W. Lamb, “Low-noise, high-efficiency optics design for alma receivers,” *Antennas and Propagation, IEEE Transactions on*, vol. 51, pp. 2035–2047, Aug 2003.

[8] C. Cunningham, G. Tan, H. Rudolf, K. Saini, J. Webber, G. H. Tan, C. Haupt, R. Murowinki, and M. Tarenghi, “Science team decision on frequency coverage and frequency overlap for the alma band 1 receiver design,” Report FEND-40.02.01.00-0008-C-REP, ALMA, 2013.

[9] O. Morata, J. Di Francesco, and C. Kemper, “Change request for the band 1 frequency coverage,” ALMA change request ALMA-90.00.00.00-0021-A-CRE, ALMA, 2013.

[10] J. D. Francesco, D. Johnstone, B. C. Matthews, N. Bartel, L. Bronfman, S. Casassus, S. Chitsazzadeh, H. Chou, M. Cunningham, G. Duchene, J. Geisbuesch, A. Hales, P. T. P. Ho, M. Houde, D. Iono, F. Kemper, A. Kepley, P. M. Koch, K. Kohno, R. Kothes, S. P. Lai, K. Y. Lin, S. Y. Liu, B. Mason, T. J. Maccarone, N. Mizuno, O. Morata, G. Schieven, A. M. M. Scaife, D. Scott, H. Shang, M. Shimojo, Y. N. Su, S. Takakuwa, J. Wagg, A. Wootten, and F. Yusef-Zadeh, “The science cases for building a band 1 receiver suite for alma,” 2013.

[11] Y. Hwang, C. Chiong, J. Kuo, D. Henke, and M. Pospieszalski, “Band 1 cartridge preliminary design report,” ALMA change request FEND-40.02.01.00-0039-B-REP, ALMA, 2013.

[12] Y. Hwang, C. C., T. Huang, Y. Kuo, C. Lin, C. Ho, H. Chuang, M. Pospieszalski, D. Henke, S. Claude, N. Reyes, and F. Finger, “Development of band-1 receiver cartridge for atacama large millimeter/submillimeter array (alma),” *Proc. SPIE 9153, Millimeter, Submillimeter, and Far-Infrared Detectors and Instrumentation for Astronomy VII, 91532H*, p. 14, 2014.

[13] M. Carter and et al., “Alma front-end optics design report,” Design Report FEND-40.02.00.00-035-B-REP, ALMA, 2007.

[14] P. Zorzi, *Design and construction of an optical system for a 31-45 GHz Radioastronomical receiver*. PhD thesis, Dep. de Ingeniería Eléctrica, U. de Chile, 2013.

[15] P. Zorzi, C. Granet, F. Colleoni, N. Reyes, J. Pizarro, F. Mena, and L. Bronfman, "Construction and measurement of a 31.3-45 ghz optimized spline-profile horn with corrugations," *Journal of Infrared, Millimeter, and Terahertz Waves*, vol. 33, no. 1, pp. 17–24, 2012.

[16] N. Reyes, M. Sanchéz, F. Mena, R. Finger, D. Henke, S. Claude, and K. Yeung, "Alma front-end band 1 design report," Design Report FEND-40.02.01.00-0050-A5-REP, ALMA, 2014.

[17] V. Tapia, F. Mena, N. Reyes, and P. Zorzi, "Diseño, construcción y medición de una antena tipo bocina para el receptor heterodino de banda 1 de alma.," engineering thesis, Universidad de Chile, 2013.

[18] N. Reyes, V. Tapia, D. Henke, M. Sanchez-Carrasco, F. Mena, S. Claude, and L. Bronfman, "Design of the optical system for alma band 1," *Proc. SPIE*, vol. 9145, pp. 91451W–91451W–8, 2014.

[19] P. Goldsmith, *Quasioptical Systems: Gaussian Beam Quasioptical Propogation and Applications*. IEEE Press Series on RF and Microwave Technology, Wiley, 1998.

[20] C. A. Balanis, *Antenna Theory, Analysis and design*. Hoboken, New Jersey: Wiley, 3 edition, 2005.

[21] "Ieee standard definitions of terms for antennas," *IEEE Std 145-1983*, pp. 1–31, 1983.

[22] T. Milligan, *Modern Antenna Design*. Wiley, 2005.

[23] B. Widenberg, "A general mode matching technique applied to bandpass radomes," Tech. Rep. TEAT-7098, 2001.

[24] P. Masterman and P. Clarricoats, "Computer field-matching solution of waveguide transverse discontinuities," *Electrical Engineers, Proceedings of the Institution of*, vol. 118, pp. 51–63, January 1971.

[25] N. Dagli, "Mode matching technique as applied to open guided-wave structures," *Progress In Electromagnetics Research*, vol. 10, pp. 75–121, 1995.

[26] R. Collin, *Field Theory of Guided Waves*. Wiley, 1991.

[27] W. Gibson, *The Method of Moments in Electromagnetics*. CRC Press, 2007.

[28] G. Dhatt, E. Lefrançois, and G. Touzot, *Finite Element Method*. ISTE, Wiley, 2013.

[29] Ansys, "Ansoft-antenna/rf training guide," Training Manual 5.0.1, ANSYS, 2010.

[30] R. Johnson and H. Jasik, *Antenna Engineering Handbook*. Electronics: Electrical engineering, McGraw-Hill, 1993.

[31] J. W. Lamb, "Cross-polarisation and astigmatism in matching grooves," *International Journal of Infrared and Millimeter Waves*, vol. 17, no. 12, pp. 2159–2165, 1996.

[32] R. Nesti and V. Natale, "Notes on dielectric characterization in waveguide," application note, IRA-INAF Arcetri Astrophysical Observatory.

[33] K. C. Yaw, "Measurement of dielectric material properties," Application Note RAC0607-0019_1_4e, Rohde & Schwarz, 2012.

[34] J. Sheen, "Comparisons of microwave dielectric property measurements by transmission/reflection techniques and resonance techniques," *Measurement Science and Technology*, vol. 20, no. 4, p. 042001, 2009.

[35] J. Teniente, *Modern Corrugated horn antennas.* PhD thesis, Departamento de Ingeniería Eléctrica y Electrónica,Universidad Pública de Navarra, Pamplona, 2003.

[36] K. Pontoppidan, "Electromagnetic properties and optical analysis of the alma antennas and front ends," Design Report S-1430-02, TICRA, 2007.

[37] P. Wade, *Parabolic dish antenna.* N1BWT, 1998.

[38] M. Sugimoto and N. Mizuno, "Alma front end band 1 to band 10 ir filter technical specification," Design Report FEND-40.03.01.04-001-A-SPE, ALMA, 2006.

[39] P. Zorzi, D. Henke, S. Claude, F. Mena, L. Bronfman, and J. May, "Revisiting the alma band 1 optics design," *21st international symposium on space terahertz technology 2010*, 2010.

[40] D. Vukobratovich and U. of Arizona. Optical Sciences Center, *Introduction to Opto-mechanical Design.* Optical Sciences Center, University of Arizona, 1986.

[41] J. Silvestro, "Hybrid finite element boundary integral method," white paper, Ansys, 2013.

[42] D. Koller, G. Ediss, and A. Kerr, "Dielectric constant of goretex ra7956/7957 radome material in the frequency range 1 mhz-2 thz," ALMA memo 309, ALMA, 2000.

[43] M. Sugimoto, S. Iguchi, J. Inatani, and S. Sekimoto, Y. Asayama, "Sensitivity analysis of optical systems in radio telescopes," 2010.

[44] C. Granet and G. L. James, "Design of corrugated horns: a primer," *Antennas and Propagation Magazine, IEEE*, vol. 47, pp. 76–84, April 2005.

[45] M. Sugimoto and N. Mizuno, "Front end optics design report for aca 7-m antenna," Design Report ANTD-44.00.00.00-004-A-REP, ALMA, 2011.

[46] H. Nyquist, "Certain topics in telegraph transmission theory," *Trans. AIEE*, vol. 47, pp. 617–644, Apr. 1928.

[47] C. Shannon, "Communication in the presence of noise," *Proc. of IRE*, vol. 37, pp. 10–21, Jan. 1949.

[48] S. Gregson, J. McCormick, C. Parini, I. of Engineering, and Technology, *Principles of Planar Near-Field Antenna Measurements.* IET electromagnetic waves series, Institution of Engineering and Technology, 2007.

[49] P. Betjes, "An algorithm for automated phase center determination and its implementation," *AMTA Conference*, 2007.

[50] N. Reyes, *Design of a receiver at 31-45 GHz based on HEMT Amplifiers and schottky mixers.* PhD thesis, Dep. de Ingeniería Eléctrica, U. de Chile, Santiago de Chile, 2013.

[51] F. Colleoni, "Diseño e implementación de un sistema de medición de patrones de radiación de antenas en campo cercano," engineering thesis, Universidad de Chile, Santiago de Chile, 2012.

[52] R. Collin, *Foundations for Microwave Engineering.* IEEE Press Series on Electromagnetic Wave Theory, Wiley, 2001.

[53] S. R. Pennock and P. Shepherd, *Microwave engineering with wireless applications*. McGraw-Hill telecommunications, McGraw-Hill, 1998.

[54] P. J. B. Clarricoats and A. D. Olver, *Corrugated horns for microwave antennas / P.J.B. Clarricoats and A.D. Olver*. P. Peregrinus on behalf of the IEE London, UK, 1984.

[55] L. Barrientos and S. Morales, *Con ojos de gigantes: la observación astronómica en el siglo XXI*. Ediciones B Chile, 2008.

[56] A. B. Peck and A. J. Beasley, "High resolution sub-millimeter imaging with alma," 2008.

[57] D. J. Fixsen, "The temperature of the cosmic microwave background," 2009.

[58] O. Morata, J. Di Francesco, and C. Kemper, "Front-end sub-system for the 12 m-antenna array technical specifications," Report ALMA-40.00.00.00-001-A-SPE, ALMA, 2007.

[59] C. Balanis, *Modern Antenna Handbook*. Wiley, 2008.